Johan Moan Dalene

Self-propagating high-temperature synthesis of zirconium disilicide

Masteroppgave i Industriell kjemi og bioteknologi
Veileder: Kjell Wiik & Mari-Ann Einarsrud
Juli 2020

Masteroppgave

NTNU
Norges teknisk-naturvitenskapelige universitet
Fakultet for naturvitenskap
Institutt for materialteknologi

NTNU
Kunnskap for en bedre verden

Johan Moan Dalene

Self-propagating high-temperature synthesis of zirconium disilicide

Masteroppgave i Industriell kjemi og bioteknologi
Veileder: Kjell Wiik & Mari-Ann Einarsrud
Juli 2020

Norges teknisk-naturvitenskapelige universitet
Fakultet for naturvitenskap
Institutt for materialteknologi

NTNU
Kunnskap for en bedre verden

Preface

This is the master thesis of my M.Sc in materials chemistry, and it has given fascinating insight in self-propagating high-temperature synthesis and $ZrSi_2$ and its applications, especially in nuclear industry. I am glad that I got the opportunity to collaborate with Elkem Fossegrenda on these subjects during this final year of my degree, and would like to thank them for their contributions to this thesis. I would like to credit supervisors professor Kjell Wiik and professor Mari-Ann Einarsrud for their valuable feedback and guidance, and I would also like to highlight the value of their broad and firm knowledge within the fields of material technology and chemistry. The experimental work in this thesis could not have been done without the assistance of technical staff at the Department of Materials Science and Engineering, who have shown an admirable dedication and motivation to facilitate experimental work. The spring of 2020 will undoubtedly be remembered as challenging in regard to logistics and activity at NTNU just like everywhere else in the Norwegian society, due to necessary action taken against COVID-19. I am impressed with the flexibility and initiative displayed by NTNU and everyone at the Department of Materials Science and Engineering in this situation, which confirmed that overcoming challenges and solving problems is everyday business at NTNU.

Even though this thesis and degree in general has served many challenges and frustrations, the open and inclusive environment among the students at the Department of Materials and Engineering, the program Chemical Engineering and Biotechnology, and among students in Trondheim in general has turned these five years into five years of fun, friendship, and growth, and I will probably remember this better than the challenges and frustration when thinking back.

Finally, I would like to thank my partner, family, and friends. They make me feel that I can always get the support I need, and their care and understanding has been greatly appreciated, especially during the last weeks of writing this thesis.

Abstract

In this thesis, a self-developed reactor utilizing a Mg-BaO_2 igniter mixture in a tube furnace was used for SHS of $ZrSi_2$. Literature on combustion synthesis, zirconium, silicon, and the Zr-Si system, was reviewed to establish an expectation of how Zr-Si powder mixtures behave during mixture preparation and SHS. The influence of milling parameters during co-milling of zirconium and silicon was investigated by characterization of milled mixtures by XRD and SEM. The influence of reactor, sample, and experiment properties on the combustion reaction was investigated with different configurations of SHS followed by characterization of reacted samples by XRD and SEM. Silicothermic reduction of ZrO_2 was investigated as a possible negative influence on SHS by thermal analysis and XRD. The reactivity between zirconium silicides and zirconium and silicon was investigated to determine its effect on SHS of zirconium silicides. Results of the co-milling of zirconium and silicon revealed that large milling media causes flattening and deforming of zirconium particles, while small milling media causes crushing of zirconium particles. The results of the SHS-experiments revealed that the combustion formation of $ZrSi_2$ was sensitive and negatively affected by the explosivity of the igniter, dissipation of heat from the samples, insufficient size reduction of the zirconium particles, and solid-state diffusion before ignition. Silicothermic reduction and reactivity between zirconium silicide and zirconium and silicon was considered to have a negligible effect on SHS of zirconium silicides. Based on available literature on the successful large-scale SHS of $MoSi_2$, the main challenge of large-scale application of SHS of $ZrSi_2$ was determined to be sufficient size reduction of the zirconium powder.

Sammendrag

I denne oppgaven ble en selv-utviklet reaktor som benyttet en Mg-BaO_2 antennelsesblanding i en rørovn bruk til SHS av $ZrSi_2$. Litteratur om forbrenningssyntese, zirkonium, silisium og Zr-Si systemet ble studert for å etablere en forventning til hvordan Zr-Si pulverblandinger oppfører seg under forberedelse av blandingen og SHS. Innflytelsen til mølleparametere under ko-mølling av zirkonium og silisium ble undersøkt ved karakterisering av møllede bladninger ved XRD og SEM. Innflytelsen til reaktor-, prøve-, og eksperimentegenskaper ble undersøkt med forskjellige konfigurasjoner av SHS etterfulgt av karakterisering av prøver ved XRD og SEM. Silisotermisk reduksjon av ZrO_2 ble undersøkt som en mulig negativ innflytelse på SHS ved termisk analyse og XRD. Reaktiviteten mellom zirkoniumsilisider or zirkonium og silisium ble undersøkt for å bestemme dens effekt på SHS av zirkoniumsilisider. Resultatene av SHS-eksperimentene avslørte at forbrennigsdannelsen av $ZrSi_2$ var sensitiv og ble negativt påvirket av eksplosiviteten til igniteren, spredning av varme fra prøvene, utilstrekkelig størrelsesreduksjon av zirkoniumpartiklene, og fast-stoff diffusjon før antennelse. Silisotermisk reduksjon og reaktivitet mellom zirkoniumsilisid og zirkonium og silisium ble betraktet til å ha neglisjerbar effekt på SHS av zirkoniumsilisider. Basert på tilgengelig litteratur om den suksessfulle stor-skala syntesen av $MoSi_2$, ble det fastslått at størrelsesreduksjon av zirkonium er den største utfordringen i stor-skala applikasjon av SHS av $ZrSi_2$.

Contents

Preface i

Abstract iii

Sammendrag v

Table of Contents x

List of Tables xiii

List of Figures xx

Abbreviations xxi

1 Introduction 1
- 1.1 Background and motivation . . . 1
- 1.2 Aim and scope of the work . . . 2

2 Literature Review 5
- 2.1 Combustion Synthesis . . . 5
  - 2.1.1 General characteristics . . . 5
  - 2.1.2 Configurations . . . 6
- 2.2 Self-propagating high-temperature synthesis . . . 8
  - 2.2.1 Heating . . . 9
  - 2.2.2 Ignition . . . 12
  - 2.2.3 Reaction propagation . . . 12
- 2.3 Properties and reactivity of silicon . . . 15
  - 2.3.1 Chemical and mechanical properties . . . 15

2.3.2 Interactions with oxygen . . . 16
2.3.3 Interactions with other gases . . . 17
2.4 Properties and reactivity of zirconium . . . 17
2.4.1 Chemical and mechanical properties . . . 17
2.4.2 Interactions with oxygen . . . 18
2.4.3 Interactions with other gases/atmospheres . . . 19
2.5 Transition metal-silicon systems and intermetallics . . . 22
2.5.1 Molybdenum and the Mo-Si system . . . 23
2.5.2 The Zr-Si system . . . 25
2.6 Synthesis of zirconium silicides . . . 28
2.6.1 SHS of zirconium silicides . . . 28
2.6.2 Alternative methods . . . 34

3 Experimental **37**
3.1 Chemicals and apparatus . . . 37
3.2 Characterization methods . . . 39
3.2.1 Characterization by XRD . . . 39
3.2.2 Characterization by SEM . . . 41
3.3 Co-milling of zirconium and silicon . . . 41
3.4 Pre-experiment: Development of SHS reactor . . . 41
3.4.1 Resistive heating . . . 42
3.4.2 Chemical ignition . . . 45
3.5 SHS experiments . . . 50
3.5.1 SHS-experiment configurations . . . 50
3.5.2 Configuration utilizing furnace temperature gradient . . . 53
3.5.3 SHS at room temperature . . . 54
3.5.4 SHS at 600 °C . . . 55
3.5.5 Experiment using furnace temperature gradient . . . 56
3.5.6 Sample table . . . 56
3.6 Other experiments . . . 57
3.6.1 Silicothermic reduction of ZrO_2 . . . 57
3.6.2 Reactivity between zirconium silicides and precursors . . . 58

4 Results **61**
4.1 Characterization of precursor powders . . . 61
4.1.1 SEM images . . . 61
4.1.2 Powder XRD . . . 64
4.2 Co-milling of zirconium and silicon . . . 66
4.3 SHS experiments . . . 68
4.3.1 SHS at room temperature . . . 68
4.3.2 SHS at 600 °C . . . 79
4.3.3 SHS with inherent tube furnace gradient . . . 85
4.3.4 Summary of results . . . 90
4.4 Silicothermic reduction . . . 91
4.4.1 Oxidation of zirconium powder . . . 91
4.4.2 DSC/TGA measurement of siliocthermic reduction . . . 91

4.5 Reactivity between zirconium silicides and precursors 94

5 Discussion **95**
5.1 SHS experiments 95
5.1.1 Reaction completeness in different experiments 95
5.1.2 Effect of synthesis temperature and igniter explosivity on the ignition of Zr-Si mixtures 97
5.1.3 Propagation of combustion in a Zr-Si mixture 97
5.1.4 SHS of $ZrSi_2$ compared to SHS of $MoSi_2$ 100
5.2 Co-milling of zirconium and silicon 100
5.3 The SHS-experiment set-up 100
5.4 Silicothermic reduction 102
5.4.1 Reactivity 102
5.4.2 Relevance for SHS 102
5.5 Reactivity between zirconium silicides and precursors 103
5.5.1 Reactivity of silicon versus reactivity of zirconium 103
5.6 Relevance to SHS 103

6 Conclusions **105**
6.0.1 Factors causing incomplete SHS 105
6.0.2 Reactions general for the Zr-Si system 106

7 Further Work **107**
7.1 Future studies of SHS of $ZrSi_2$ 107
7.2 Large scale synthesis of $ZrSi_2$ by SHS 107
7.2.1 SHS from ZrH_2 and Si 107
7.2.2 SHS from ZrO_2 and Si 108

Appendices **i**
A Estimation of SiO(g) partial pressure i
B Properties of reactants ii
C Customized flange iii
D Observations during SHS iv
D.1 Heating of igniter in tube furnace iv
D.2 Zr+2Si(Room temp, Indep. Ign)1 after experiment iv
D.3 Cracking of alumina tube by Zr+2Si(Room temp, Indep. Ign)2 . . v
D.4 Igniter pieces on Zr+Si(Room temp, Ign. in fila.) v
D.5 Samples Zr+2Si(600 °C, Ign. in cylinder) and Zr+2Si(600 °C, Ign. in cylinder) before and after the experiment vii
D.6 Zr+2Si(1400 °C, Temp. grad.) after synthesis vii
E Reactivity between zirconium silicides and precursors - diffractograms . . ix
E.1 3Zr + Si ix
E.2 $ZrSi_2$ + 3Zr x
E.3 $Zr_{(3)}Si$ + 5Si xii
F Documentation for received powders xiv
Silicon powder data xiv

Zirconium powder data xviii

List of Tables

2.1 Temperature of eutectic points involving MoO_2 or MoO_3 estimated either empirically or by thermodynamic modelling. The data is taken from Zhang *et al.* [54], where the empirical values were gathered from available literature and the thermodynamic modelling was done in the study. 24

2.2 Formation enthalpy values of the phases in the Zr-Si gathered from available literature. Note that values from Bertolino *et al.* [67] are converted from $\mathrm{kJ\,mol^{-1}}$ to $\mathrm{kJ\,(mol\ of\ atoms)^{-1}}$, given that there are x+y moles of atoms in one mol of Zr_xSi_y, and that values from Shu *et al.* [68] were estimated by reading of Figure 1 in the article 28

2.3 The formation enthalpy of the phases in the Zr-Si binary system, the measured combustion temperature during SHS of a Zr-Si powder mixture with stoichiometry corresponding to the zirconium silicide phase, and the melting point of each phase. The table also includes the melting points of zirconium, silicon, and the zirconium-rich and silicon-rich eutectic points in the Zr-Si system. Note that not all of the phases melt congruently, but some form a eutectic with another phase or decompose peritectically to another phase and a liquid 30

2.4 Densities of some zirconium silicides taken from Shu *et al.* [68], and the volume reduction as percent loss of initial volume. 31

3.1 The table shows the properties of the chemicals used in this project, and how they are referred to in this report (See section F for more data). Note that the silicon content in silicon powder is measured by the amount of expected impurities, and that surface oxide is omitted [80] 37

3.2 The apparatus used during the experiments, and how they are referred to in the text 38

3.3 Reference XRD-peaks used to qualitatively determine the present phases in powder samples from the diffractograms obtained in this thesis 40
3.4 The resulting composition from combined Pawley and Rietveld refinement of the diffractogram in Figure 3.6. The Rwp and GOF were 13.6 and 4.7 respectively 47
3.5 Samples from SHS-experiments, with the Zr-Si mixture used to make the sample, and the configuration and temperature of the experiment 57

4.1 Resulting composition from combined Pawley and Rietveld refinement of the diffractogram shown in Figure 4.4. Rwp and GOF were 4.39 and 3.23 respectively 65
4.2 Composition estimated by combined Pawley and Rietveld refinement of the diffractograms shown in Figure 4.9. Rwp and GOF were 9.36 and 4.0 for the "Igniter contact"-diffractogram and 7.40 and 3.0 for the "Igniter adjacent"-diffractogram 71
4.3 Composition estimated by combined Pawley and Rietveld refinement of the diffractogram shown in Figure 4.15. Rwp and GOF were 7.48 and 3.1 77
4.4 The result of the EDS point scans of points shown in Figure 4.16b, and what phases are assumed to be present at these points based on the composition. Epoxy, which contributes with a large amount of carbon and a small amount of oxygen, is ignored when assuming which phases are present in each point 79
4.5 Composition estimated by combined Pawley and Rietveld refinement of the diffractograms shown in Figure 4.18. Rwp and GOF were 9.81 and 2.2 for the "Igniter contact"-diffractogram and 13.37 and 3.0 for the "Igniter adjacent"-diffractogram 81
4.6 Resulting composition from combined Pawley and Rietveld refinement of the diffractogram shown in Figure 4.19. Rwp and GOF were 5.27 and 2.0 respectively 82
4.7 Resulting composition from combined Pawley and Rietveld refinements of diffractogram shown in Figure 4.21. Rwp and GOF were 10.55 and 4.2 in respectively 84
4.8 Resulting compositions from combined Pawley and Rietveld refinements of diffractograms shown in Figure 4.23. Rwp and GOF were 10.93 and 4.4 in "Unreacted", 12.56 and 4.8 in "Reaction front", and 14.95 and 5.8 in "Reacted" 87
4.9 The Zr-Si mixture and experiment configuration used in the SHS-experiments, and the amount of product formed in different ares of the samples. The configurations are described in section 2.1.2 90
4.10 Composition of ZrO_2-Si sample before DSC/TGA measurement, and after measurement which was given by combined Pawley and Rietveld refinement of the diffractogram shown in Figure 4.27. Rwp and GOF were 8,72 and 2,3 respectively 93
4.11 Resulting compositions from combined Pawley and Rietveld refinement of diffractograms of samples generated by the experiments presented in section 3.6.2 94

B1 Collection of presented chemical and mechanical properties zirconium and silicon compounds ii

List of Figures

1.1 Figure illustrating the promising use of $ZrSi_2$ as a refractory material, with special focus on use as an accident-tolerant protective coating for zirconium alloy in nuclear reactors, the advantages of producing $ZrSi_2$ by SHS, and the main focus of this thesis which is whether SHS is feasible for large-scale production of $ZrSi_2$ 3

2.1 Illustration of generalized approaches to combustion synthesis. A illustrates local heating at one end of a compacted sample, leading to ignition in heated volume which releases heat and results in a propagating reaction wave. This approach is referred to as "self-propagating high-temperature synthesis". B illustrates uniform heating of a compacted green reactive mixture which leads to ignition and heating simultaneously throughout the green reactive mixture. This approach is referred to as volume synthesis or "thermal explosion mode". C illustrates an approach where the initial green reactive mixture is a loose powder mixture which may be slightly compacted before heating and will be subjected to pressure during synthesis. The heating is not local as in A, but may be less uniform than in B. D illustrates a similar approach, but where the applied heat is as local as in B. 7

2.2 The figure illustrates the combustion wave that arises during combustion synthesis, and the processes that occur in and around the front of the wave [22]. 13

2.3 Dependency of combustion temperature T_c and wave velocity U on parameters of the green reactive mixture. The splitting of the curve in figure (e) illustrates that velocity either can grow monotonically with ρ_0, or go through a maximum [8] 15

2.4 Gibbs free energy of the reaction in Eq. (2.12) at discrete temperatures with $5\,^{\circ}\mathrm{C}$ intervals collected from HSC Chemistry, and the partial pressure of SiO(g) calculated at these temperatures based on estimation of chemical activity and the equilibrium constant of the reaction (see section A) 17

2.5 Zr-O binary phase diagram compiled from available experimental results [40] 18

2.6 Zr-N phase diagram at $101\,325\,\mathrm{Pa}$ calculated by Ma *et al.* [46] 20

2.7 Zr-H binary phase diagram [47] 21

2.8 Phase diagram of the binary Mo-Si system at ambient pressure [55] . . . 24

2.9 Widely accepted binary phase diagram of the Zr-Si system created by Okamoto [58] by assessing available experimental data 26

2.10 Gibbs free energy of the reaction in Eq. (2.18) with $n, m = 1, 2$ at discrete temperatures with $5\,^{\circ}\mathrm{C}$ intervals collected from HSC Chemistry, and the partial vapor pressure of SiO(g), calculated at these temperatures based on estimation of chemical activity and the equilibrium constant of the reaction (see section A). The partial pressure is compared to the partial pressure of SiO at the Si-SiO_2 interface (see Figure 2.4) 27

3.1 Schematic of the chosen set-up for the SHS experiments. "Sample" refers to a pressed pellet of a Zr-Si powder mixture, "Igniter" refers to a chemical igniter, *i.e.* highly exothermically reactive powder mixture, "Alumina container" may be any alumina container that fits the purpose, here represented by an alumina ship 42

3.2 The two proposed filament designs for use in the SHS reactor. a) shows $1\,\mathrm{mm}$ 8020NiCr filament used for conduction intertwined with $0.4\,\mathrm{mm}$ Kanthal A filament for heating. b) shows the polished tip of a $1\,\mathrm{mm}$ 8020NiCr filament 43

3.3 The experimental set-up for testing the heat generation in the two filament designs presented in Figure 3.2 44

3.4 Glow in $0.4\,\mathrm{mm}$ Kanthal A filament connected to four $1\,\mathrm{mm}$ 8020 NiCr filaments on each end with an applied voltage of $11\,\mathrm{V}$ 45

3.5 Diffractogram from XRD over a 2θ-range of 30–130° of magnesium powder using a step size of $0.01°$ with $1.1\,\mathrm{s}$ per step 46

3.6 The resulting diffractogram from XRD of BaO_2-powder over a 2θ-range of 20–145° with a step size of $0.01°$ and $0.9\,\mathrm{s}$ per step. The indicators show which phases contribute to which peaks in the combined Pawley and Rietveld refinement in the 2θ-range 20–120°. It should be noted that the last peak indicated with BaO_2 was excluded in the final refinement, but previous refinements indicated that the peak was solely caused by BaO_2 . 47

3.7 DSC and TGA data from heating a mixture of small Mg-chips and BaO_2-powder up to $600\,^{\circ}\mathrm{C}$ and cooling down to room temperature, with a heating- and cooling rate of $600\,^{\circ}\mathrm{C\,h^{-1}}$ and alumina powder as reference 48

3.8 DSC and TGA data from heating a mixture of magnesium- and BaO_2-powder up to $600\,^{\circ}\mathrm{C}$ and cooling down to room temperature, with a heating- and cooling rate of $600\,^{\circ}\mathrm{C\,h^{-1}}$ and alumina powder as reference. a) shows the whole measurements, while b) highlights measurements before ignition. 49
3.9 Illustrations of the three general configurations of sample, igniter, and filament in room temperature SHS experiments. a) illustrates a sample in contact with an igniter pellet which in turn is in (attempted) contact with the heating filament. This configuration is referred to as "Independent Igniter" in text, and "Indep. Ign.)" in sample names. b) illustrates an igniter pellet pressed within the sample, and the filament is in (attempted) contact with the igniter. This configuration is referred to as "Pressed in igniter" in text, and "Pressed in ign." in sample names. c) illustrates the igniter pellet being forced to be in contact with the filament, which is in (attempted) contact with the sample. This configuration is referred to as "Igniter in filament" in text, and "Ign. in fila." in sample names. 51
3.10 Illustration of configurations used in SHS-experiments were the sample and surroundings are heated to $600\,^{\circ}\mathrm{C}$. a) illustrates a beam-shaped sample with an igniter pressed in at one end. This configuration is referred to as "Igniter in beam end" in text and "Ign- in beam" in sample names. b) illustrates a cylindrical sample where the igniter is pressed in the center of the sample. This configuration is referred to as "Igniter in cylinder" in text and "Ign- in cylinder" in sample names. 53
3.11 Illustration of the set-up used for an SHS experiment only utilizing the inherent temperature gradient in the tube furnace. This configuration is referred to as "Temperature gradient" in text and "Temp. grad." in samples 54
3.12 Flow scheme illustrating the preparation of an treatment samples for studying reactivity between zirconium silicides and zirconium and silicon powders 59

4.1 SEM-images in SE-mode, with $100\,\mathrm{X\ magnification}$ of the zirconium and silicon powders, where a) shows the zirconium powder, b) the Si(<75)-powder, c) the Si(10-75)-powder, and d) the Si(40-100)-powder. 62
4.2 SEM-images in SE-mode of the smallest particles observed in the a) zirconium powder at $16\,\mathrm{kX\ magnification}$ and b) Si(<75) powder at $40\,\mathrm{kX\ magnification}$ 63
4.3 XRD diffractograms of the received silicon powders, where a) shows the full diffractograms and b) shows a low intensity range that reveals the smaller peaks 64
4.4 XRD diffractogram of the received Zr powder 65
4.5 Diffractograms of attritor-milled Zr+2Si mixtures where one was milled with $5\,\mathrm{mm}$ zirconia balls, and the other was milled with $2\,\mathrm{mm}$ zirconia balls. 66
4.6 SEM-image taken in SE-mode of a Zr+2Si powder mixture attritor-milled with $5\,\mathrm{mm}$ zirconia balls in isopropanol 67
4.7 SEM-image taken in SE-mode of a Zr+2Si powder mixture attritor-milled with $2\,\mathrm{mm}$ zirconia balls in isopropanol 68
4.8 Illustration of where the powder samples for XRD were taken from the sample Zr+2Si(Room temp, Indep. Ign.) 69

4.9 Resulting diffractograms from XRD of the Zr+2Si(Room temp, Indep. Ign.)1- The indicators indicate which phases contributed to which peaks in the combined Pawley and Rietveld refinement 70
4.10 Diffractograms of samples taken from Zr+2Si(Room temp, Indep. Ign.)2 (see Table 3.5). The indicators illustrate which phases were attributed to which peaks during a qualitative assessment in Bruker Eva 72
4.11 Illustration of the powder samples taken from Zr+2Si(Room temp, Pressed in ign.) (see Table 3.5) 73
4.12 Resulting diffractograms from XRD of the samples from the room temperature SHS experiment where the heating filament was adjacent to the end of the Zr+2Si beam which had an igniter pellet pressed into it. The indicators indicate which phases are attributed to which peaks based on qualitative assessment in Bruker Eva. 74
4.13 Illustration of the powder samples taken of the Zr+2Si samples from the SHS experiment with the configuration illustrated in Figure 3.9c 75
4.14 Resulting diffractograms from XRD of Zr+2Si(Room temp, Ign. in fila.) (see Table 3.5). The indicators indicate which phases are attributed to which peaks based on qualitative assessment in Bruker Eva. 76
4.15 Resulting diffractogram from piece of Zr+Si(Room temp, Ign. in fila.) (see Table 3.5) struck by a igniter piece. The indicators illustrate which phases contribute to which peaks during combined Pawley and Rietveld refinement 77
4.16 SEM-images taken in BSE-mode of a of Zr+Si(Room temp, Ign. in fila.) (see Table 3.5. In the EDS-maps, red indicates zirconium, yellow zirconium silicides, and green silicon. a) shows an overview of the center of the samples, b) shows the edge of the sample where the igniter struck, with points where EDS point scans were done, c) shows a close up of an area in b), and d) shows the same area with an EDS-map overlay 78
4.17 Illustrations of XRD-samples taken from Zr+2Si(600 °C, Ign. in beam) (see Table 3.5) 79
4.18 Diffractograms taken from powder samples of Zr+2Si(600 °C, Ign. in beam) (see Table 3.5). The indicators illustrate which phase contributed to which peaks during combined Pawley and Rietveld refinement 80
4.19 Resulting diffractograms from XRD of the powder sampleZr+2Si(600 °C, Ign. in cylinder) (see Table 3.5). The indicators illustrate which phases contributed to which peaks in the combined Pawley and Rietveld refinements 81
4.20 The figure shows SEM-images taken in BSE-mode of the sample Zr+2Si(600 °C, Ign. in cylinder) (see Table 3.5). a) shows the difference between the reacted zone, the reaction front, and the unreacted front, and b) is close-up of the reaction front with an EDS-map overlay. In the EDS-map, red refers to zirconium, yellow refers to zirconium silicides, and green refers to silicon 82
4.21 Resulting diffractogram from XRD of the powder sample taken from Zr+Si(600 °C, Ign. in cylinder) (see Table 3.5)The indicators illustrate which phases contributed to which peaks in the combined Pawley and Rietveld refinements 83

4.22 SEM-images taken in BSE-mode of a sample taken from Zr+Si(600 °C, Ign. in cylinder) (see Table 3.5) a) shows an area of the microstructure and composition that extended from the edge that was in contact of the igniter and across the majority of the sample. In the EDS-map overlay, red refers to zirconium, yellow refers to zirconium silicides, and green refers to silicon. b) shows an area of the microstructure that extends from the far edge from the igniter contact point and inwards to before the middle of the sample. 84

4.23 Resulting diffractograms of powder samples taken from an alumina ship filled with a lightly compacted attritor-milled Zr+2Si powder mixture which was placed with one end in the center of the tube furnace, after heating to 1391 °C at on end and approximately 1337 °C at the other. The indicators illustrate which phases contributed to which peaks during combined Pawley and Rietveld refinements 86

4.24 SEM-images taken in BSE-mode with EDS-map overlay of samples taken from an alumina ship filled with a lightly compacted attritor-milled Zr+2Si powder mixture which was placed with one end in the center of the tube furnace, after heating to 1391 °C at on end and approximately 1337 °C at the other. In the EDS-maps, red refers to zirconium, yellow refers zirconium silicides, and green refers to silicon 87

4.25 Diffractogram from powder XRD of zirconium powder heated to 1500 °C in synthetic air 91

4.26 DSC/TGA characerization of a ZrO_2 and Si powder mixture in an alumina crucible in argon atmosphere during heating to 1550 °C 92

4.27 Diffractogram from powder XRD of ZrO_2 and Si powder mixture analyzed with TGA/DSC. Which phase(s) contributed to each peaks during Pawley and Rietveld refinement is shown by the indicators 93

5.1 SEM-images showing four types of synthesis completion. a) is an image of Zr+Si(Room temp, Ign. in fila.) and depicts initiation of silicon melt and formation of zirconium silicides without ignition in the Zr-Si mixture. b) is an image of Zr+2Si(600 °C, Ign. in cylinder) and depicts combustion at the igniter contact point, and establishment of combustion front adjacent to the igniter, but no propagation. c) is an image of of Zr+2Si(1400 °C, Temp. grad.) and depicts well-defined border between a nearly completely reacted zone and a somewhat reacted zone. d) is an image of Zr+Si(600 °C, Ign. in cylinder) and depicts the microstructure of the nearly fully reacted sample. Experimental details of each sample is given in Table 3.5. 96

5.2 Results of pre-experiment leading to the conclusion that resistive heating combined with chemical ignition could be used in the room temperature SHS experiments. a) shows the observed glow in a Kanthal A filament when a voltage of 11 V was applied, and b) shows a DSC/TGA-analysis of a Mg-BaO_2 powder mixture heated to 600 °C and cooled back down . . 101

C1 Drawings of the custom flange needed for the room temperature experiments. a) is the initial sketch, and b) is the technical drawing used for machining of the flange. iii
D2 Images of course of events during an SHS-experiment. a) shows the filament glowing when a current is passed through, b) shows the explosion of the igniter pellet, c) shows a fading glow likely coming from the igniter, and d) shows that the glow from both filament and igniter disappears after the explosion iv
D3 Images of the sample Zr+2Si(Room temp, Indep. Ign)1 (see Table 3.5). a) is a top view of the sample, and b) is an image of the side that was in contact with the igniter v
D4 Image of alumina tube sample container and part of Zr+2Si beam that was in contact with igniter during a room temperature SHS experiment where the filament was adjacent to the igniter pellet which was in contact with the Zr+2Si beam v
D5 Zr+Si(Room temp, Ign. in fila.) (see Table 3.5) after experiment. The small white pieces are pieces of the exploding igniter. vi
D6 Images of Samples Zr+2Si($600\,^{\circ}\mathrm{C}$, Ign. in cylinder) and Zr+2Si($600\,^{\circ}\mathrm{C}$, Ign. in cylinder) a) before and b) after the experiment vii
D7 Top view of Zr+2Si($1400\,^{\circ}\mathrm{C}$, Temp. grad.) (see Table 3.5) after the experiment viii
E8 The resulting diffractogram of XRD of the sample "3Zr+Si"(see section 3.6.2) at $1500\,^{\circ}\mathrm{C}$ for one hour, with a heating rate of $200\,^{\circ}\mathrm{C\,h^{-1}}$. Which phases contribute to each peak is shown with indicators. ix
E9 The resulting diffractogram of XRD of the sample "$ZrSi_2$+Zr" (see section 3.6.2) after it was heated and held at $1500\,^{\circ}\mathrm{C}$ for one hour, with a heating rate of $200\,^{\circ}\mathrm{C\,h^{-1}}$. Which phases contribute to each peak is shown with indicators. x
E10 The resulting diffractogram of XRD of the sample "$ZrSi_2$+Zr"(see section 3.6.2) after it was heated to $1400\,^{\circ}\mathrm{C}$ with a heating rate of $200\,^{\circ}\mathrm{C\,h^{-1}}$. Which phases contribute to each peak is shown with indicators. xi
E11 The resulting diffractogram of XRD of the mixture "$Zr_{(3)}$Si + 5 Si" (see section 3.6.2), after it was heated and held at $1500\,^{\circ}\mathrm{C}$ for one hour, with a heating rate of $200\,^{\circ}\mathrm{C\,h^{-1}}$. Which phases contribute to each peak is shown with indicators. xii
E12 The resulting diffractogram of XRD of the mixture "$Zr_{(3)}$Si + 5 Si" (see section 3.6.2), after it was heated to $1400\,^{\circ}\mathrm{C}$ with a heating rate of $200\,^{\circ}\mathrm{C\,h^{-1}}$. Which phases contribute to each peak is shown with indicators. xiii

Abbreviations

BSE Backscattered Electrons.

CIP Cold Isostatic Pressing.

CS Combustion Synthesis.

DSC Differential Scanning Calorimetry.

EDS Energy-Dispersive x-ray Spectroscopy.

GOF Goodness of Fit.

HFIHCS High-Frequency Indcution-Heated Combustion Synthesis.

PCACS Pulsed Current Activated Combustion Synthesis.

SE Secondary Electrons.

SEM Scanning Electron Microscopy.

SHS Self-propagating High-temperature Synthesis.

TGA Thermogravimetric Analysis.

UTS Ultimate tensile strength.

XRD X-Ray Diffraction.

1 Introduction

1.1 Background and motivation

$ZrSi_2$ is a transition metal silicide. This group of materials does in general exhibit high thermal stability, excellent corrosion resistance, high electronic conductivity and unique electronic structures, and high compatibility with silicon substrates. Earlier research explored the potential use of $ZrSi_2$ in integrated circuits [1]. $ZrSi_2$ has similar properties as the common refractory ceramic $MoSi_2$, and might exhibit superior performance at high temperatures. Additionally, $ZrSi_2$ is not vulnerable to pest oxidation at lower temperatures which is a critical weakness in $MoSi_2$ [2] [3]. Later research suggests potential use in catalysis and as an accident-tolerant protective coating for zirconium cladding materials. In the latter application, $ZrSi_2$ appears to have an unrivaled potential due to its excellent adhesion to zirconium alloys and excellent corrosion resistance. Zirconium alloys are commonly used as a fuel cladding in nuclear power plants, and they have good corrosion resistance at operating conditions, but may be severely oxidized by steam in a loss-of-coolant accident in certain nuclear reactors. This compromises the cladding material while generating hydrogen gas, and was the cause of the explosions in the nuclear reactor buildings at the Fukushima Daiichi power plant in 2011. In high-temperature oxidizing atmospheres, $ZrSi_2$ forms nanoscale zirconia and silica-structures by spinodal decomposition which acts as a diffusion barrier for oxygen, and results in a corrosion resistant coating with no signs of spallation at temperatures up to $1200\,^{\circ}\mathrm{C}$. [4][5]

The current commercially available $ZrSi_2$ is expensive and is mostly used for research on the aforementioned applications. In order to utilize $ZrSi_2$ in improvement of current technology or development of new technology, it must be produced on a large scale and at a price that does not outweigh the gain of applying the material. The synthesis route should also give the opportunity to control characteristics like purity and microstructure in the final product so it can be tailored for different applications.

A synthesis route that may fulfill these requirements is self-propagating high-temperature

synthesis (SHS). In general, the synthesis utilizes the exothermic formation of a compound to supply the required energy needed in the synthesis. That is, a small volume of the green reactive mixture is heated to reaction, and the generated heat of reaction heats the adjacent mixture to reaction, resulting in the reaction propagating through the mixture as a wave. Although a SHS-reactor must be able to locally heat a mixture to high temperature and then withstand the high temperature generated by the synthesis, the principle is fairly simple and easily scalable. The reaction between zirconium and silicon to form zirconium silicides - including $ZrSi_2$ - is exothermic enough to be utilized in SHS, and they can therefore be synthesized from zirconium and silicon powders in a relatively simple reactor. SHS has been shown to produce high-purity $ZrSi_2$, and the microstructure of the final product can be affected by the microstructure of the precursor powder and synthesis parameters.

To date, large-scale SHS of $ZrSi_2$ has not been extensively studied. Most research on SHS of $ZrSi_2$ has focused on whether it is a possible synthesis route, reaction mechanisms and kinetics. The studies utilize methods, equipment, and reactants, which are mostly only viable on a laboratory scale, with little focus on commercial feasibility. In order to propose and develop a commercially viable synthesis route, the performance and reliability of SHS using commercially viable methods, equipment, and reactants must be understood. Additionally, a full synthesis route from precursor zirconium and silicon powders to $ZrSi_2$ requires a sound understanding of the behaviour and interactions in the precursor powder.

All in all, $ZrSi_2$ has promising refractory applications, especially as an accident-tolerant protective coating in certain nuclear reactors, and SHS is a promising synthesis route for large-scale production. However, there is little understanding of whether production of $ZrSi_2$ by SHS is commercially viable, which is what this thesis intends to explore. A summary of the motivation behind the thesis is illustrated in Figure 1.1.

1.2 Aim and scope of the work

The aim of the thesis is to develop an understanding of the opportunities and challenges with a full synthesis route based on SHS for large-scale production of $ZrSi_2$. The work that was done to achieve this can be divided in three parts, which all consist of establishing a foundation of knowledge based on available literature and results obtained from previous work ([6]), followed by experimental work.

First, an efficient and scalable way of preparing green reactive Zr+Si mixtures from commercially available powders was explored. Then, an experimental set-up for SHS was developed by using equipment that is viable for up-scaling. The aim was to explore the possible solutions to achieving a commercially attractive way of performing SHS of $ZrSi_2$. The set-up was then used to attempt to synthesize $ZrSi_2$ in order to study the reactive mixture's behaviour during SHS and to expose challenges with up-scaling and minimizing cost of SHS of $ZrSi_2$. Finally, the reactivity in the Zr-Si system at high temperature was studied. This included the reactivity of the zirconium oxide layer with silicon, and the reactivity between zirconium silicides and zirconium or silicon. These experiments were done to give insight on how other reactions than the combustion reaction in SHS influences

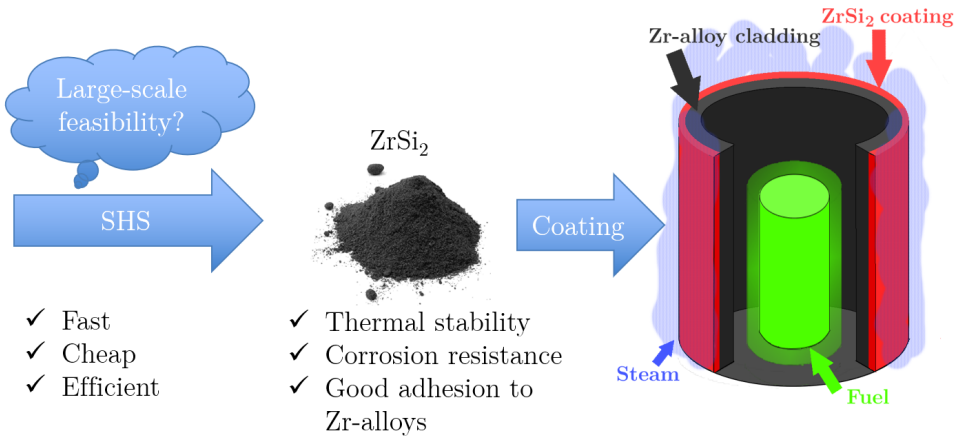

Figure 1.1: Figure illustrating the promising use of $ZrSi_2$ as a refractory material, with special focus on use as an accident-tolerant protective coating for zirconium alloy in nuclear reactors, the advantages of producing $ZrSi_2$ by SHS, and the main focus of this thesis which is whether SHS is feasible for large-scale production of $ZrSi_2$

the synthesis.

2 Literature Review

In this chapter, combustion synthesis will be presented, and SHS will be discussed in detail. In order to create an optimal synthesis route, the interactions between the precursor powders, and also between precursor powders and synthesis conditions, must be assessed. These interactions include how the powders react to processing like milling and heating, and how they react with the different atmospheres and materials used during processing. The literature review of combustion synthesis and the properties of zirconium and silicon will be followed by a presentation of Some of the content in this chapter is based on Dalene [6], and will be referred to when appropriate. In each section where this is done, it will be explained which paragraphs are reused in which are unique to this thesis.

2.1 Combustion Synthesis

2.1.1 General characteristics

All content in this section is based on Dalene [6]. Combustion synthesis (CS) is a synthesis route where a material is produced through an exothermic reaction. In these synthesis methods, the exothermic nature of the reaction can be taken advantage of to decrease the required energy input. However, CS often use precursors that require a large amount of energy to be refined from raw materials. Another attractive feature, aside from the stored energy in itself, is the characteristics of how the stored energy is released during combustion. Since the reactions are usually fast and strongly exothermic, the system can reach temperatures between 2000–$4000\,\mathrm{K}$ at heating rates in the range of 10^4–$10^5\,\mathrm{K\,s^{-1}}$ [7]. Levashov *et al.* [7] focus mainly on SHS, but much can be generalized for CS. CS is initially characterized by the physical state of precursors:

- Solid-state: At least one precursor is in solid phase. Even if all precursors are in solid phase, the combustion may include intermediate liquid phases and gas evolution due to the high temperatures.

- Solution Combustion Synthesis: Precursors are in aqueous solution. Heat is generated by combustion of an organic fuel like glycine or urea.
- Flame Synthesis: Precursors are in gas phase.
- Spray Flame Pyrolysis: Precursors can be in both gas and liquid phase.

In this thesis, the focus will be on solid-state CS. Different types of solid-state CS can be distinguished based on the chemistry of the synthesis. Three of these are relevant to this thesis. The first type uses elements as precursors, and a general reaction can be formulated as:

$$\sum_{i=1}^{n} R_i^s \longrightarrow \sum_{i=1}^{m} P_i^{s,l} + Q \tag{2.1}$$

where R represents the precursors, P represents the product, s and l solid and liquid state respectively, and Q the heat of reaction. The second utilizes a thermite type reaction. At least one precursor is an oxide, and a reducing metal is added. The general reaction can be formulated as:

$$\sum_{i=1}^{n}(\mathrm{MeO}_x)_i^s + \sum_{i=1}^{m} Z_i^s + \sum_{i=1}^{k} X_i^s \longrightarrow \sum_{i=1}^{j} P_i^{s,l} + \sum_{i=1}^{l}(\mathrm{ZO}_y)_i^s + Q \tag{2.2}$$

where MeO_x is a metal oxide, Z is a metal with a higher affinity to oxygen than Me, X is an elemental precursor, P is the desired product, ZO_y is the product of the oxidation of Z, and Q is the heat of reaction. The third type utilizes inorganic compounds as precursors. Examples of this reaction type are metathesis reactions, for example:

$$\mathrm{MeCl}_n(\mathrm{s}) + \mathrm{X}_n\mathrm{E}(\mathrm{s}) \longrightarrow \mathrm{MeE}(\mathrm{s}) + n\mathrm{XCl} + Q \tag{2.3}$$

Where $\mathrm{MeCl}_n(\mathrm{s})$ is a metal chloride, $\mathrm{X}_n\mathrm{E}(\mathrm{s})$ can be an alkali/earth alkali pnictide or chalcogenide, $\mathrm{MeE}(\mathrm{s})$ is the desired product and Q is the heat of reaction. Other types of reactions can be between a solid precursor and a gas to form hydrides, oxides, nitrides, or carbides, or exchange reactions between for example metal and non-metal nitride to form a metal nitride.

2.1.2 Configurations

The content in this section is based on edits of Dalene [6]. The current configurations of SHS can be divided into three general approaches, based on whether heat is supplied locally and whether pressure is applied to the green reactive mixture during the synthesis. The three configurations are illustrated in Figure 2.1

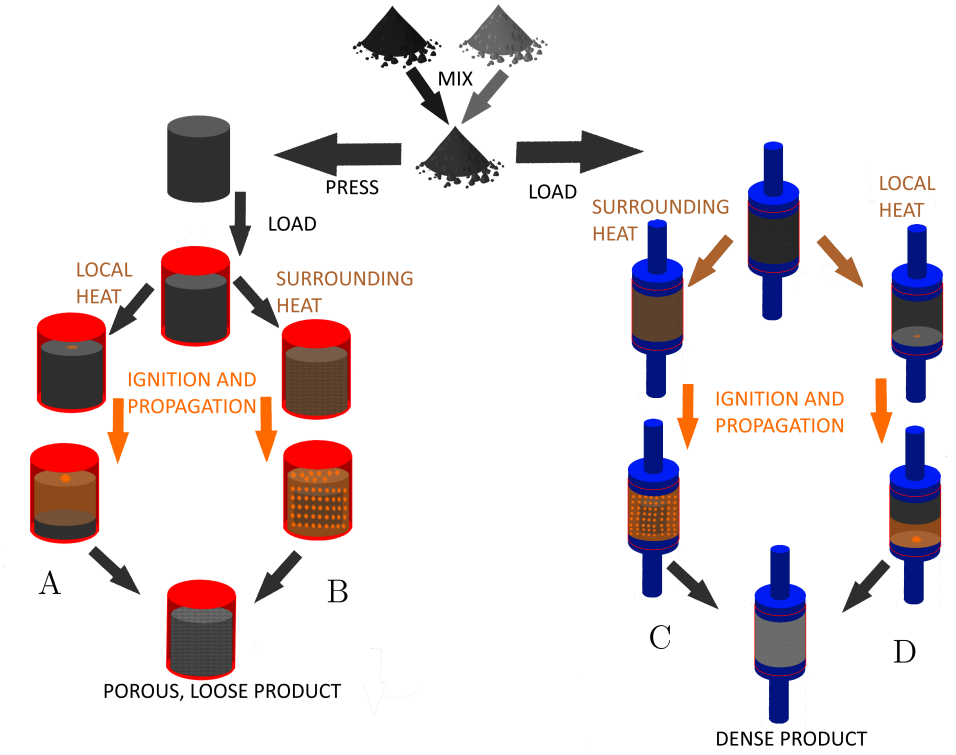

Figure 2.1: Illustration of generalized approaches to combustion synthesis. A illustrates local heating at one end of a compacted sample, leading to ignition in heated volume which releases heat and results in a propagating reaction wave. This approach is referred to as "self-propagating high-temperature synthesis". B illustrates uniform heating of a compacted green reactive mixture which leads to ignition and heating simultaneously throughout the green reactive mixture. This approach is referred to as volume synthesis or "thermal explosion mode". C illustrates an approach where the initial green reactive mixture is a loose powder mixture which may be slightly compacted before heating and will be subjected to pressure during synthesis. The heating is not local as in A, but may be less uniform than in B. D illustrates a similar approach, but where the applied heat is as local as in B.

Figure 2.1 Indicates that routes A and B require the sample to be a pressed green body. This is not entirely accurate, as it is possible to use a powder mixture which is not pressed during pre-treatment. [7]

Self-propagating synthesis

As illustrated in Figure 2.1, a complete reaction can be achieved by only heating a small volume of the green reactive mixture, since the released reaction heat causes the reaction to

propagate through the mixture. Thus, the required heat addition for this approach is only a small fraction of the heat needed to ignite the entire mixture. However, the approach requires the reaction to release enough heat to propagate the reaction. This approach is highly researched, is commonly referred to as "self-propagating high-temperature synthesis" (SHS), and will be discussed in further detail in section 2.2. Route D in Figure 2.1 illustrates an application of pressure during synthesis, which is required to achieve a dense product. The pressure may be applied a few seconds after ignition (optimization of this delay is actually of great importance to achieve maximum density), or can be utilized to ignite the mixture instead of heating. A mechanical piston driven by high-pressure gas hits the side of the mixture, resulting in compression and a rapid temperature increase which is high enough to ignite the mixture, resulting in self-propagating reaction with a supersonic propagation rate. [7] In the rest of the literature review, the focus will be on SHS without applied pressure, *i.e.* route B in Figure 2.1.

Volume synthesis

Volume synthesis refers to an approach where the green reactive mixture is heated uniformly, leading to the reaction occurring simultaneously in the entire sample which is illustrated as route B in Figure 2.1. Compared to the self-propagating mode presented in the previous paragraph, this mode is not as sensitive to the exothermicity of the mixture , but requires far more energy. Therefore, there has been little interest in this approach beyond laboratory experiments. [8] Also illustrated in Figure 2.1 is an approach that may be described as volume synthesis with applied pressure during combustion. Two examples of this approach are "pulsed current activated combustion synthesis" (PCACS) and "High-frequency induction-heated combustion synthesis" (HFIHCS). PCACS and HFIHCS are recent synthesis techniques with the intention of producing a dense, sintered product in one step. Both techniques do this by applying pressure during combustion and the synthesis is performed with a powder mixture in a graphite die between two alumina punches. The main difference between the two is how the mixture is ignited. PCACS heats the mixture to ignition by passing a current through the die and the mixture causing resistive heating [9]. This technique was used by Ko *et al.* [10] to produce a dense $ZrSi_2$-SiC composite with grain sizes on the nanoscale with a density of $97\,\%$ of theoretical density. An interesting effect of these synthesis techniques is that they utilize the heat of the reaction to sinter the materials, and the sharp temperature increase at ignition combined with applied pressure may lead to unique microstructure properties. PCACS is similar to spark-plasma sintering, but may achieve even higher temperatures due to the generated heat of formation. HFIHCS heats the powder mixture and graphite die by an induction coil [11]. This technique was used by Park *et al.* [11] to synthesize nanoscale $ZrSi_2$ from mechanically activated Zr and Si with a density of $96\,\%$ of theoretical density.

2.2 Self-propagating high-temperature synthesis

In section 2.1.2, SHS was presented as a mode of CS where heat is supplied to only a small part of the green reactive mixture, which ignites and reacts, resulting in the released heat of reaction establishing a combustion wave propagating through the mixture. The process

can be divided into three main stages:

- Local heating
- Ignition in heated volume
- Propagation of reaction through combustion wave

In this section, these three stages will be discussed in further detail.

2.2.1 Heating

As mentioned, the main idea of SHS is to supply heat to a small volume of a green reactive mixture, and let the reaction propagate from this volume. The mixture needs a good thermal conductivity to propagate the reaction, but the thermal conductivity may also be a disadvantage when attempting to raise the temperature in a small volume. To overcome dissipation of the supplied heat and equalization of temperature in the mixture, a method that is able to supply heat both locally and rapidly must be utilized. Several approaches to supply the required heat for combustion synthesis have been explored in previous research. Some of the approaches are only viable for volume synthesis while some are also viable for SHS. In this section, a selection of approaches that have been successfully utilized in SHS and some that may potentially be utilized will be presented.

Resistive heating

Resistive heating is based on generation of heat caused by an electrical current passing through a medium with an electrical resistance. The heating power generated from the passing current is given by:

$$P = I^2 R \tag{2.4}$$

where P is the heating power in watts, I is the electrical current in ampere, and R is the electrical resistance of the medium in ohm. Resistive heating can be "direct", which means that the material to be heated is heated by passing a current through the material, or "indirect", which means that a dedicated conductor is heated by a passing current, and the material is subsequently heated by heat transferred from the conductor. [12, p. 28-29] In SHS, resistive heating is often utilized by heating a approximately $1\,\mathrm{cm}^3$ of the green reactive mixture indirectly [7]. The advantages of indirect heating is that a dedicated heating filament may have properties that better facilitate joule heating. With direct heating, it may also be more difficult to concentrate the heating power on a small volume, so it is better suited for volume synthesis approaches like PCACS which was presented in section 2.1.2. An approach to utilize direct resistive heating in SHS is "spark ignition", where a high voltage discharge within the mixture heats the mixture to ignition by direct resistive heating. However, this approach is not suited for SHS in powder mixtures as the conductivity in the powders in the mixture may inhibit the build-up of charge between electrodes.

Inductive heating

Inductive heating resembles direct resistance heating described in the previous paragraph, in the sense that heat is generated by an electrical current in the material. The main dif-

ference is that the current in the sample is generated by an alternating magnetic field according to Lenz's law, which states that if a conductor is subjected to a magnetic field, an electrical current that generates an opposing magnetic field will be generated in the conductor. However, a current will only be induced while the strength or direction of the magnetic field is changing. In practice, induction heating of a sample is done by passing a high-frequency alternating current through a coil that surrounds the sample. An alternating current will be induced at the surface and inwards in the sample, depending on the skin depth which is determined by the frequency of the AC in the coil and material properties [12, p. 75-78]. Even though the heating is limited to the surface and a certain thickness inwards, induction heating is difficult to localize, and is better suited for HFIHCS presented in section 2.1.2.

Laser heating

The mechanism that generates heat in a material during laser heating is in principle the same mechanism that causes radiative heat transfer, *i.e.* electrons absorbing the photon energy through excitation to a higher energy-state and subsequent relaxation to lower-vibrational stages by release of photons before the relaxation back to the ground state. Lasers give the opportunity to quickly focus large amounts of energy in the form of light on a small surface area of a material, and the penetration depth can be as short as a few nanometers. [13] Thus, laser irradiation can be utilized to quickly heat a small volume on one side of a green reactive mixture to ignition. Additionally, the use of laser heating allows the distance between sample and heat source to be increased with only negligible "defocusing" of heat generation in the sample. Laser ignited SHS has been used to successfully synthesize titanium carbide [14].

Microwave heating

Microwave heating utilizes the oscillating electric and magnetic fields in electromagnetic waves to generate heat in the material. This is done by sending electromagnetic waves with an oscillation frequency close to either $900\,\mathrm{MHz}$ or $2450\,\mathrm{MHz}$. Electromagnetic waves can generate heat in materials that are either electrically conductive or polar dielectric materials. In electrical conductors, heat is generated by the oscillating electric and magnetic fields in the same manner as direct resistive heating and induction heating respectively. In polar dielectrics, the electric field causes oscillation in the material when the dipoles try to align themselves to oppose the electric field. [15, pp. 1–19] Nishvili *et al.* [16] argue that the heating power of microwaves on metals is too low to heat a mixture from room temperature to ignition, but that the heating power rises significantly with increasing power. This can be utilized to assist the SHS after it has been heated to ignition by another heat source; This means that microwaves can be used to selectively supply heat to the combustion wave, which can help sustain the large temperature gradients which are characteristic for SHS, and keep the propagation stable (more detailed discussions on propagation will be done in section 2.2.3). [16] This is referred to as microwave-assisted SHS, and is of interest in recent studies [7].

Chemical heating

Exothermic reactions are the basis of the self-sustained propagating characteristic of SHS, but may also be utilized to supply the necessary heat for ignition. An obvious requirement for a chemical is that it ignites at a lower temperature than the green reactive mixture. Preferably, the igniter should ignite and combust at room temperature since a secondary heat source is needed to heat the igniter. An approach to this is a hypergolic igniter, which instantaneously reacts rapidly and strongly exothermically with the green reactive mixture when they are brought in contact with each other. Different alternatives to hypergolic igniters have been proposed in previous literature. However, this approach requires a method of bringing the igniter in contact with the green reactive mixture in a sealed reactor. Additionally, hypergolic igniters are usually gaseous or liquid, which in addition to the biproducts of the igniter reaction could make purity in the final product a challenge. [17] Another approach is to use an independent mixture as a chemical igniter. A powder mixture is easy to incorporate in the green reactive mixture, but this mixture must in turn be stable during preparation of the green reactive mixture before synthesis. Ideally, the chemical igniter is stable during preparation but requires only a small temperature increase to react. A potential candidate is a mixture of magnesium powder and barium peroxide powder. Relative to other peroxides, BaO_2 is stable and inexpensive to produce, but will liberate oxygen extensively at temperatures above $500\,^{\circ}\mathrm{C}$ at atmospheric pressure. The substance that is formed during oxygen release melts at $800\,^{\circ}\mathrm{C}$, and it is completely reacted to barium oxide at $900\,^{\circ}\mathrm{C}$ [18, p. 66-73]. Magnesium resembles zirconium in that is has the same crystal structures at ambient pressure, and is readily oxidized, which may be described by the reaction:

$$\mathrm{Mg(s)} + \frac{1}{2}\mathrm{O_2(g)} \longrightarrow \mathrm{MgO(s)} \qquad \Delta_r G^{\ominus} = -569\,\mathrm{kJ\,mol^{-1}}[19] \tag{2.5}$$

The reaction between magnesium and BaO_2 can be described by

$$\mathrm{Mg(s)} + \mathrm{BaO_2} \longrightarrow \mathrm{MgO(s)} + \mathrm{BaO(s)} \qquad \Delta_r H^{\ominus} = -522\,\mathrm{kJ\,mol^{-1}}[19] \tag{2.6}$$

It should be noted that this reaction may occur via release of oxygen from BaO_2 as oxygen gas, which may then be a byproduct of the reaction if the kinetics of oxygen release is faster than the kinetics of magnesium oxidation. The kinetics of magnesium oxidation may be increased by reducing the powder particle size or melting the magnesium powder. The melting point of magnesium is $650\,^{\circ}\mathrm{C}$, far lower than the melting point of zirconium (see section 2.4.1). Thus, even though oxidation of metals like zirconium oxidizes more spontaneously than magnesium, the low melting point of magnesium may result in less released oxygen gas, ignition at a lower temperature, and a faster reaction all together. The ignition of the $MgBaO_2$ mixture was studied by Hogan *et al.* [20]. Isolated, BaO_2 exhibited a weight loss that was attributed to release of oxygen gas, which began at $600\,^{\circ}\mathrm{C}$. Isolated magnesium in air exhibited a weight increase at around $600\,^{\circ}\mathrm{C}$ which was attributed to formation of magnesium nitride and magnesium oxide. Differential thermal analysis of a Mg-BaO_2 mixture revealed ignition of the mixture at $540\,^{\circ}\mathrm{C}$, with a substantial exotherm reaction preceding the reaction. This suggests that the reaction in Eq. (2.5) may be independent of the isolated reactions of oxygen release and magnesium oxidation, but it could also be attributed to initiation of the reactions on a small scale, which heats parts of the powder to temperatures above the measured temperatures and ignites the reaction.

2.2.2 Ignition

The local heating of a small volume should lead to ignition when the volume reaches a certain temperature, *i.e.* the ignition temperature. Ignition can in SHS be seen as when the rate of a reaction has a sharp increase, or a new reaction with a much higher reaction rate than the previous reaction is initiated. Additionally, the rate of the reaction(s) should become so high that the reaction heat is released significantly faster than heat is dissipated away from the volume in order to initiate the combustion wave. For most systems viable for gasless solid-state SHS, this combustion reaction occurs above the melting point of at least one of the reactants or possible products, or above the lowest eutectic of the system, which indicate that ignition in most systems is caused by formation of a liquid. Initially, the temperature must become high enough for the reactants to be able to overcome activation energy of the formation of the product. When this is achieved, the reactivity pre-ignition is governed by solid-state diffusion. The rate of solid-state diffusion depends on particle surface area, temperature, and the crystal structure of the materials, but is generally low and will not cause a sharp increase in temperature. If a liquid is formed from one or both reactants, the diffusion rate between reactants increases in several orders of magnitude, and the possibility of dissolution of one reactant in the other arises. The reaction of rate of dissolution of reactant and precipitation of product also has a severely higher reaction rate than solid-state diffusion. Another possibility is that the product film formed between reactant particles during solid-state diffusion melts, which increases reactants diffusion rate and thus the reaction rate. [21, p. 8, 133] Thus, the correlation between combustion temperature and the lowest temperature where a liquid is formed can attributed to the kinetics of the expected interactions between the reactants at different temperature regimes.

2.2.3 Reaction propagation

One of the most important characteristics of SHS is the combustion wave. The combustion wave is the result of unreacted precursor being heated to ignition by the released heat of the reaction of adjacent precursors. Different processes occur in and around the combustion wave, as illustrated in Figure 2.2.

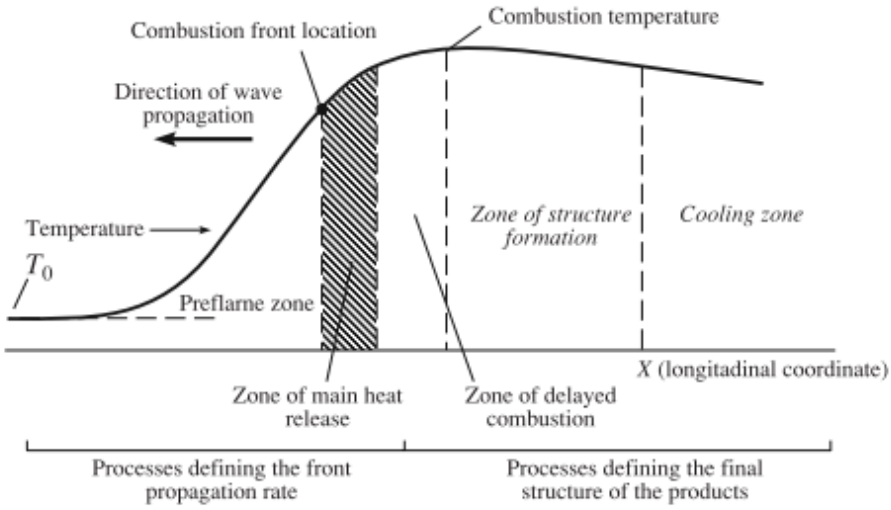

Figure 2.2: The figure illustrates the combustion wave that arises during combustion synthesis, and the processes that occur in and around the front of the wave [22].

The zone with the largest temperature gradient is denoted as the combustion front. In front of this is what is called the warm-up zone, which is heated by the reaction taking place just behind the combustion in what is denoted as "zone of main heat release" in Figure 2.2. Behind the zone of main heat release, post-combustion reactions take place, where delayed combustion reactions may occur and the structure of the final product is formed during cooling [22]. This zone In addition, grain growth, crystal structure ordering, and solidification of melt occurs in this zone, hence the cooling rate behind the combustion wave significantly impacts both the composition and the microstructure in the final product [21, p.206-207].

Important parameters when describing the self-propagating combustion of the green reactive mixture are the temperature generated when the precursors react, combustion temperature (T_c), combustion wave velocity (U) which is the velocity at which the generated heat ignites adjacent precursors. An approximation to T_c is to assume that all the reaction heat is used to heat the reaction product, *i.e.* neglecting heat loss to both the front and the back of the combustion front. The resulting temperature, T_{ad}, can be described by the equation

$$\Delta_{\mathrm{r}} H^{\ominus} + \sum_i \Delta_{\mathrm{pt}} H_{\mathrm{i}}^{\ominus} = \int_{T_0}^{T_{ad}} C_p(T)\, dT \tag{2.7}$$

where T_0 is the initial temperature in the green reactive mixture. T_0 is assumed to be 298 K if there is no bulk heating of the green reactive mixture in addition to the local heating. $\Delta_{\mathrm{r}} H^{\ominus}$ is the standard reaction enthalpy of the combustion reaction, C_p is the total molar

specific heat capacity of the product(s), and $\sum_i \Delta_{\text{pt}} H_{\text{i}}^{\ominus}$ represents the latent heat of the phase transitions in the product(s) that occur between T_0 and T_{ad}. In early literature on SHS, a rule of thumb was proposed that $T_a d$ had to be above $1800\,^{\circ}\text{C}$ for the reaction to self-propagate. [21, p. 60, 76] However, there have been found several examples that contradict this criteria. Su *et al.* [23] synthesized Cu_2Se by SHS which has an adiabatic combustion temperature of only $800\,^{\circ}\text{C}$. They also gathered and presented examples from other studies on synthesis by SHS with an adiabatic combustion temperature substantially lower than $1800\,^{\circ}\text{C}$ [23]. There have been several approaches to analytically determine the velocity of the combustion wave. The approach that is utilized in research today is the Zel'Dovich formula;

$$U \approx \frac{1}{c\rho(T_c - T_0)} \sqrt{2Q \int_{T_0}^{T_c} \lambda W(T)\, dT} \tag{2.8}$$

which suggests that the wave velocity has a positive correlation with Q, λ, and the integral of $W(T)$ between T_0 and T_c, which represents the heat of reaction, thermal conductivity in the combustion wave, and the total amount of product produced during the increase from T_0 to T_c. The formula also suggests a negative correlation with c, ρ, and the difference between T_c and T_0, which represents the heat capacity, the density, and difference between combustion temperature and initial temperature respectively. In research, the reaction rate is assumed to have an Arrhenius type correlation with temperature, and the formula is then used to determine the effective activation energy of the reaction. The formula is rewritten to

$$\ln \frac{U}{T_c} = C - \frac{E}{2R} * \frac{1}{T_c} \tag{2.9}$$

where E is the activation energy, R is the universal gas constant, and C is a constant containing heat conductivity and the pre-exponent factor of the Arrhenius equation, among other variables considered to be constant with change in temperature. E is determined by varying the combustion temperature either by pre-heating or dilution of active reactants, measuring the wave velocity, plotting $\frac{U}{T_c}$ against $\frac{1}{T}$, and determining the value of E from the slope of the linear trend. The approach is especially useful since the heat conductivity and pre-exponent factor, which are usually unknown in SHS conditions, do not need be known to determine the activation energy. The activation energy can then be used to determine the reaction mechanism and rate-limiting step in the combustion. [21, p. 140-145] Not only may the combustion wave velocity give information on mechanisms behind the SHS, it also has an inherent effect on the synthesis as a high velocity results in larger temperature gradients and less heat loss to surroundings. Varma *et al.* [8] summarize how T_c and U vary with some important parameters of the green reactive mixture.

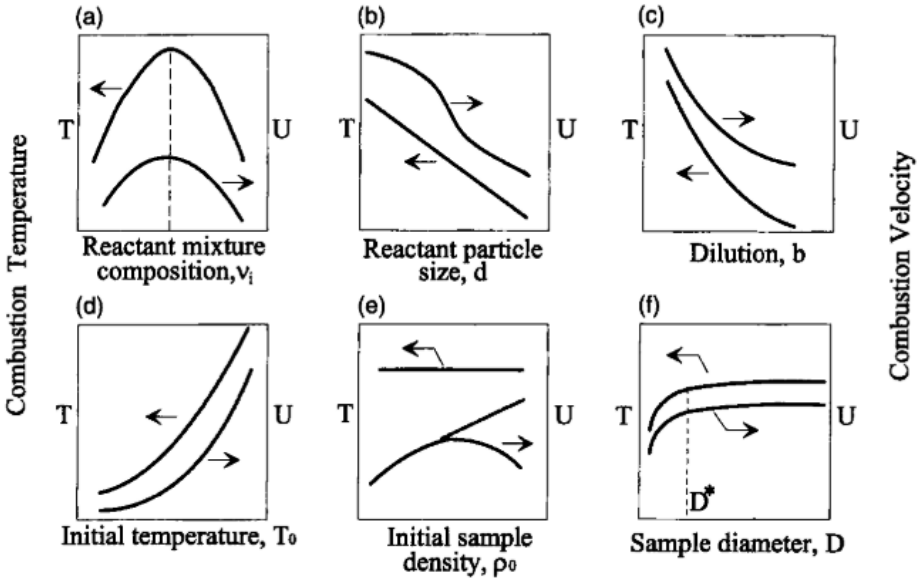

Figure 2.3: Dependency of combustion temperature T_c and wave velocity U on parameters of the green reactive mixture. The splitting of the curve in figure (e) illustrates that velocity either can grow monotonically with ρ_0, or go through a maximum [8]

It is evident that several factors impact the combustion temperature and the combustion wave velocity, which implies that the properties of the reactant powders and the green reactive mixture as a whole may negatively affect the propagation of the combustion wave. If the reaction conditions move far away from the optimum, the combustion wave is not necessarily extinguished but may enter a regime of unsteady propagation .This regime may be propagation with oscillations in velocity, or propagation in a spiral pattern [22]. These propagation patterns arise because the excess heat in the reacted product starts flowing to the combustion front if the combustion wave is slowed down [24]. These patterns are visible even to the naked eye, which can indicate sub-optimal performance even though the sample is ignited and reaction propagates.

2.3 Properties and reactivity of silicon

2.3.1 Chemical and mechanical properties

Silicon is the second most abundant element on earth, and occurs in nature in form of oxides. It is a Group 14 element with an electron configuration of [Ne]$3s^2 3p^2$, and pure silicon crystallizes in the diamond lattice (space group $Fd\bar{3}m$ in Hermann-Mauguin notation), making each silicon atom 4-coordinated, and the interatomic bonds are made by overlap of sp^3-hybridized orbitals, and is a semiconductor at room temperature. [25, p.

329-333] Silicon has several high pressure phases, and the ambient diamond phase transforms to a metallic β-tin phase at 10–12 GPa [26]. The density of the diamond phase is $2.33\,\mathrm{g\,cm^{-3}}$, and the melting point of the diamond phase at ambient pressure is $1412\,^{\circ}\mathrm{C}$ [27, p. 5-6]. The density of the liquid is higher, $2.54\,^{\circ}\mathrm{C}$, than the density of the crystal which leads to a volume reduction during melting [28]. Due to the formation of a passive layer of SiO_2, solid silicon is relatively unreactive except at high temperatures. Liquid silicon on the other hand is highly reactive. [25] Additionally, dust clouds formed by fine silicon powders have been shown to be explosive with little energy input required for ignition [29].

Single-crystal silicon has a fracture toughness of $0.6\,\mathrm{MPa\,m^{1/2}}$ at room temperature. Comparable compounds are single-crystal NaCl and glass with fracture toughness values of $0.3\,\mathrm{MPa\,m^{1/2}}$ and $0.7\,\mathrm{MPa\,m^{1/2}}$ respectively. [30, p. 630] Silicon has a sharp brittle-to-ductile transition in the temperature interval 607–$617\,^{\circ}\mathrm{C}$ where a sharp transition from brittle cleavage fracture to dislocation emission behavior occurs. [31] The E-modulus in directions $[1\,0\,0]$, $[0\,1\,0]$, $[0\,0\,1]$ is approximately $130\,\mathrm{GPa}$, while it is approximately $169\,\mathrm{GPa}$ in directions $[1\,1\,0]$, $[1\,\bar{1}\,0]$, and $[1\,1\,\bar{2}]$ [32]. The E-modulus of polycrystalline silicon is expected to lie in between these values depending on the orientation of the grains. For comparison, typical E-modulus values for aluminium alloys and iron are $69\,\mathrm{GPa}$ and $197\,\mathrm{GPa}$, respectively [30, p. 214]. In sum, silicon has notable – but not high – resistance against deformation but will experience brittle failure when deformed at temperatures up to about $600\,^{\circ}\mathrm{C}$.

2.3.2 Interactions with oxygen

Silicon is oxidized by both oxygen in air and by water in a highly spontaneous manner. In air, oxidation of silicon is described by

$$\mathrm{Si\,(s)} + \mathrm{O_2(g)} \longrightarrow \mathrm{SiO_2(s)} \qquad \Delta_r G^{\ominus} = -856\,\mathrm{kJ\,mol^{-1}}\text{[19]} \tag{2.10}$$

where the Gibbs free energy of reaction is given for standard conditions, *i.e.* $p_{\mathrm{O_2}} = 1\,\mathrm{bar}$ and temperature at $25\,^{\circ}\mathrm{C}$. Oxidation by water is described by

$$\mathrm{Si\,(s)} + 2\mathrm{H_2O\,(l)} \longrightarrow \mathrm{SiO_2(s)} + 2\mathrm{H_2(g)} \qquad \Delta_r G^{\ominus} = -382\,\mathrm{kJ\,mol^{-1}}\text{[19]} \tag{2.11}$$

where standard conditions are pH at 7 and temperature at $25\,^{\circ}\mathrm{C}$. SiO_2 forms a protective oxide layer, and the mechanisms and kinetics and further mechanism is poorly understood. However, oxidation at higher temperatures have been extensively studied, which has indicated that the thickness of the oxide layer increases linearly, and this is attributed to the diffusion of oxidating species through the oxide layer to the underlying silicon [33]. At the interface between Si and SiO_2, SiO(g) may be formed through the reaction

$$\mathrm{Si\,(s)} + \mathrm{SiO_2(s)} \longrightarrow 2\mathrm{SiO\,(g)} \uparrow \tag{2.12}$$

Figure 2.4 shows the natural logarithm of equilibrium partial pressure of SiO vs. the inverse of temperature at surrounding pressure of $1\,\mathrm{bar}$.

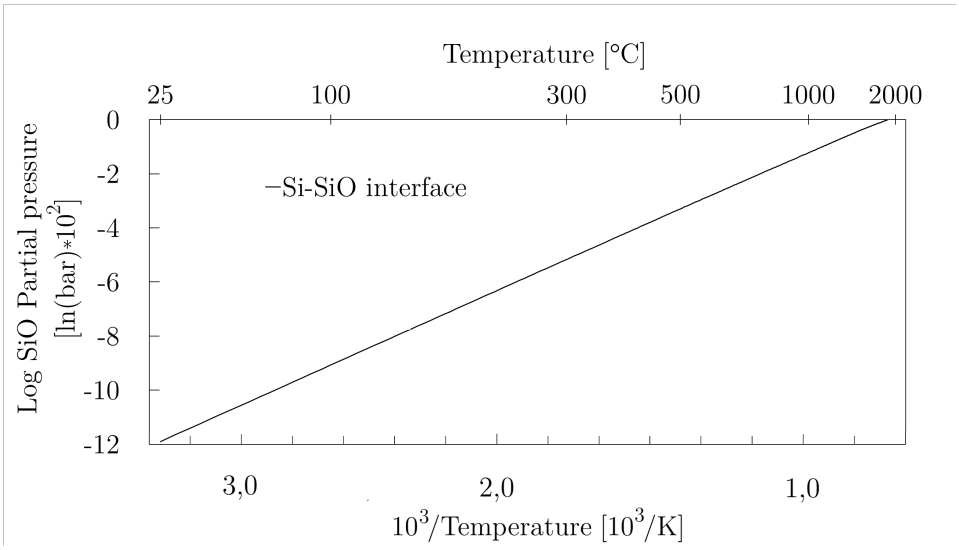

Figure 2.4: Gibbs free energy of the reaction in Eq. (2.12) at discrete temperatures with 5 °C intervals collected from HSC Chemistry, and the partial pressure of SiO(g) calculated at these temperatures based on estimation of chemical activity and the equilibrium constant of the reaction (see section A)

2.3.3 Interactions with other gases

Silicon reacts rapidly with N_2(g) at temperatures over 1400 °C to form SiN and Si_3N_4, and with sulfur vapor and phosphor vapor at 600 °C and 1000 °C respectively.

2.4 Properties and reactivity of zirconium

2.4.1 Chemical and mechanical properties

Zirconium is a group 4 transition metal, and is found in nature mainly in the form of zircon ($ZrSiO_4$) and baddeleyite ($\alpha-ZrO_2$). It is in period 5 and has the electron configuration [Kr]$4d^2 4s^2$, and has three allotropes; α, β, and ω. The crystal structures of the allotropes are hcp ($P6_3/mmc$), bcc ($Im\bar{3}m$), and simple hexagonal ($P6/mmm$) respectively. At ambient temperature and pressure, the α-phase is the equilibrium phase, which has a density of $6.51\,\mathrm{g\,cm^{-3}}$. At standard pressure, the α-phase transforms to the β-phase at 862 °C. The β-phase melts at 1857 °C. At 27 °C, α-Zr transforms to ω-Zr at 2.10 GPa, which can be considered meta-stable at ambient conditions. The triple point is estimated to be at 6.35 GPa and 637 °C. [34] [35] [36].

α-zirconium's preferential slip plane is the prismatic plane, which has been attributed to both its low c/a-ratio and electronic structure. In addition to slip, α-zirconium can be deformed by twinning [37]. Because of this, zirconium shows a ductile response to applied

stress, and Addessio *et al.* [38] found it to have an ultimate tensile strength of $280\,\mathrm{MPa}$ and failure at $55\,\%$ strain [38]. Weck *et al.* [39] calculated the Young's modulus to be 91–$98.8\,\mathrm{GPa}$ by density functional perturbation theory, matching well with the experimental reference of $95\,\mathrm{GPa}$.

2.4.2 Interactions with oxygen

Similar to silicon, zirconium is readily oxidized in both air and water. Oxidation in air is described by

$$\mathrm{Zr\,(s)} + \mathrm{O_2(g)} \longrightarrow \mathrm{ZrO_2(s)} \qquad \Delta_\mathrm{r}G^\ominus = -1101\,\mathrm{kJ\,mol^{-1}}[19] \tag{2.13}$$

where the Gibbs free energy of reaction is given for standard conditions, *i.e.* $p_{\mathrm{O_2}} = 1\,\mathrm{bar}$ and temperature at $25\,^\circ\mathrm{C}$. Oxidation by water is described by

$$\mathrm{Zr\,(s)} + 2\mathrm{H_2O\,(l)} \longrightarrow \mathrm{ZrO_2(s)} + 2\mathrm{H_2(g)} \qquad \Delta_\mathrm{r}G^\ominus = -627\,\mathrm{kJ\,mol^{-1}}[19] \tag{2.14}$$

where standard conditions are pH at 7 and temperature at $25\,^\circ\mathrm{C}$. Zirconium oxide forms a protective layer, which is chemically more complex than pure ZrO_2. Figure 2.5 shows the phase diagram of the Zr-O binary system.

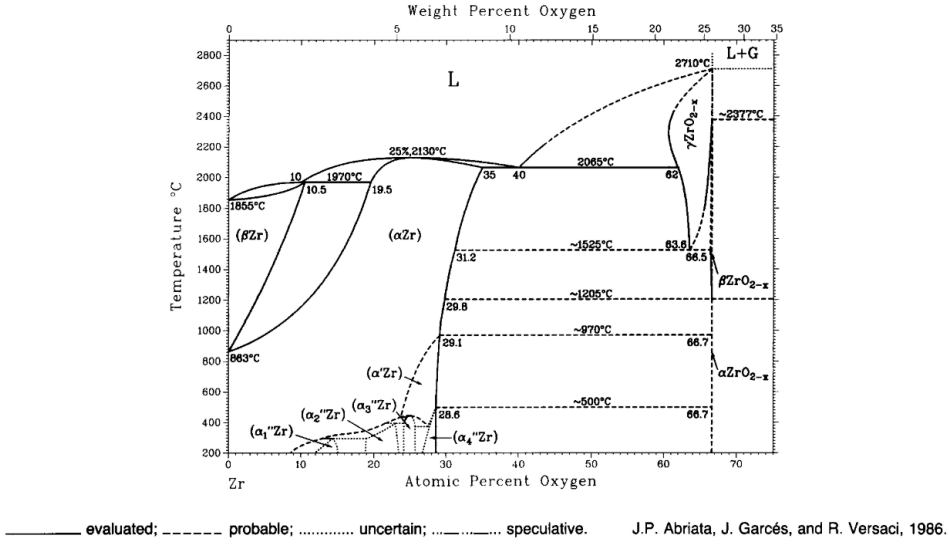

Figure 2.5: Zr-O binary phase diagram compiled from available experimental results [40]

From the phase diagram, it is evident that oxygen has a high solubility in zirconium. Dissolved oxygen can be degassed by heating the zirconium to $1000\,^\circ\mathrm{C}$ or higher [41]. The dissolved oxygen stabilizes the α-Zr phase, which is completely stabilized up to melting at an oxygen content of $19.5\,\mathrm{at.\%}$ and has a maximum solubility of $35\,\mathrm{at.\%}$ oxygen at $2065\,^\circ\mathrm{C}$. In the α-phase, the dissolved oxygen occupies octahedral holes, and α'- and α''

represents differences in how the oxygen interstitials are ordered. It is evident that increase in oxygen-content and decrease in temperature increases the ordering of the interstitials. [40] The diagram in Figure 2.5 shows that there are three ZrO_2-phases: α, β, and γ. The crystal systems of these phases are monoclinic, tetragonal, and cubic, with space groups $P2_1/c$, $P4_2/nmc$, and $Fm\bar{3}m$ respectively. The transition temperatures between these phases are denoted as "probable" by Abriata *et al.* [40], but Puchala *et al.* [42] indicate that these temperatures are still considered the reference: α-phase transforms to the β-phase at $1205\,^{\circ}\mathrm{C}$, which in turn completely transforms to the γ-phase at $2377\,^{\circ}\mathrm{C}$. However, the γ-phase can in contrast to the the other phases accommodate oxygen understoichiometry up to γ-$ZrO_{2-0.44}$, which stabilizes the phase down to $1525\,^{\circ}\mathrm{C}$.

The polymorphism of ZrO_2, in addition to the polymorphism of zirconium, makes the protective oxide layer on zirconium vulnerable to rapid changes in temperature in the region where the phase transformations occur. The phase transformations in ZrO_2 cause a substantial change in volume, which introduces microcracks that in turn reduce both toughness and thermal shock resistance. This may cause cracks that exposes the zirconium surface, which diminishes the otherwise high chemical inertness of bulk zirconium. [43, p. 914] Another phenomenon related to failure of the protective oxide layer is *breakaway*. Breakaway occurs at temperatures below the stable region of β-ZrO_2. Before breakaway, oxidation is limited by diffusion of oxygen anions from the oxide/atmosphere-interface to the metal/oxide-interface. Even though the the thermodynamically stable ZrO_2 phase is the α-phase, some β-phase is present. The β-phase is stabilized by sub-stoichiometry caused by low oxygen availability. Additionally, β-phase at the metal/oxide interface is stabilized by compressive stress caused by lattice mismatch between oxide and metal. This leads to a layer with a higher concentration of β-phase at the oxide/metal interface. The β-phase at the metal/oxide interface is an effective diffusion barrier. The mismatch between the two oxide phases results in stress that causes cracking at a certain oxide layer thickness. At the interface, the β-phase transforms martensitically to the α-phase, which compromises the diffusion barrier. Impurities in the material, N_2-gas and water steam can reduce the required time for breakaway. [44] [45, p. 271-283]

2.4.3 Interactions with other gases/atmospheres

In addition to oxygen, zirconium has a high solubility and/or reactivity with nitrogen, hydrogen, water vapor, carbon monoxide and carbon dioxide even at low pressure. The uptake of carbon dioxide is rapid above $800\,^{\circ}\mathrm{C}$. Carbon dioxide reacts with zirconium to form zirconium carbide and zirconium dioxide, making the uptake irreversible. [41] The uptake of nitrogen, hydrogen, and water vapor will be discussed in detail.

Interaction with nitrogen gas

Ma *et al.* [46] performed a thermodynamic assessment of the Zr-N binary system, which was found to be in agreement with available experimental data on the system. The resulting phase diagram is shown in Figure 2.6.

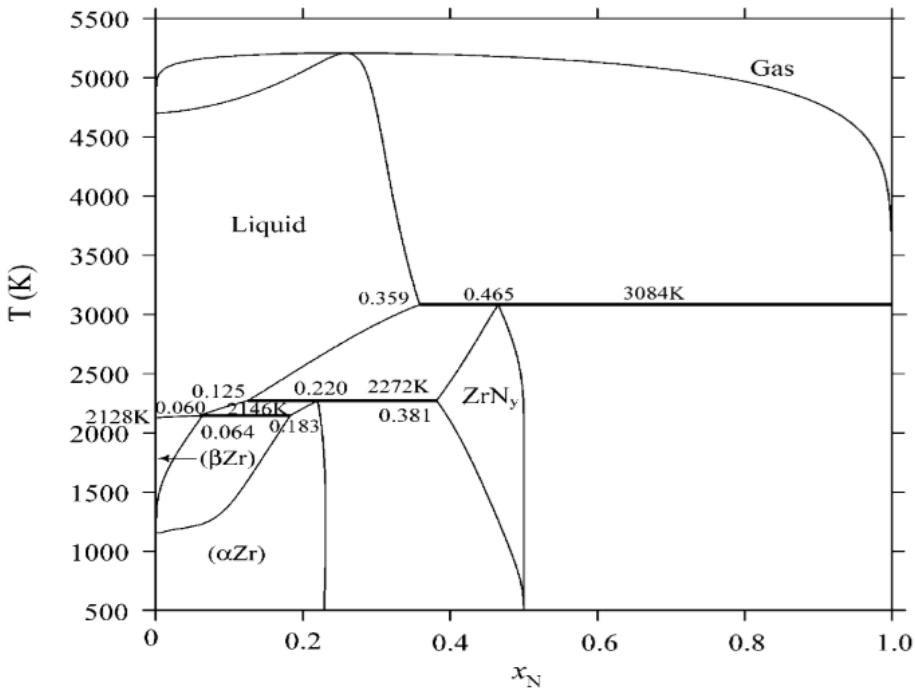

Figure 2.6: Zr-N phase diagram at 101 325 Pa calculated by Ma *et al.* [46]

From the phase diagram, it is evident that the dissolved nitrogen stabilizes the α-phase of zirconium, which has a solubility that decreases with increasing temperature, and in the interval 22–23 $\mathrm{at.\%}$ nitrogen. Beyond this, zirconium nitride is formed. Zirconium nitride can accommodate an increasing sub-stoichiometry with increasing temperature, where the maximum sub-stoichiometry corresponds to $ZrN_{0.76}$. The maximum possible concentration of nitrogen corresponds to stoichiometric zirconium nitride, *i.e.* 50 $\mathrm{at.\%}$ nitrogen. [46] Guldner *et al.* [41] found that the absorbed nitrogen could not be outgassed at 1300 °C, indicating that both zirconium nitride and nitrogen dissolved in zirconium has a high stability.

Interaction with hydrogen gas

Figure 2.7 shows the binary phase diagram of the Zr-H system.

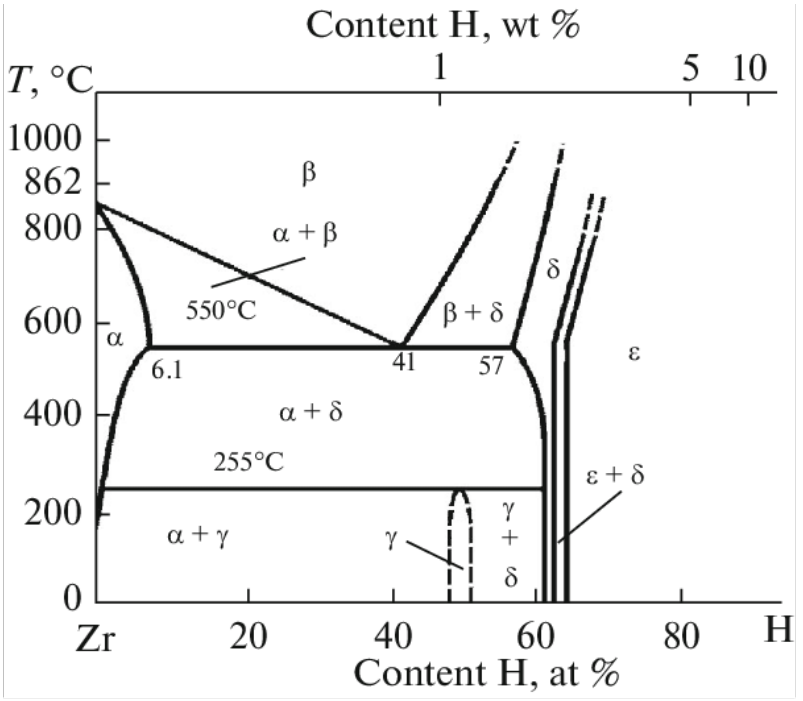

Figure 2.7: Zr-H binary phase diagram [47]

The phase diagram shows that hydrogen is most soluble in the β-phase and stabilizes this phase down to $550\,^{\circ}\mathrm{C}$ at a hydrogen content of $40\,\mathrm{at.\%}$. The phases γ, δ, and ϵ are zirconium hydride phases. The γ-phase is ZrH with a face-centered tetragonal structure, while the δ- and ϵ phases are ZrH_2 face-centered tetragonal and face-centered cubic structures respectively. It is evident from the phase diagram that both the γ- and δ-phase can accommodate a variation in stoichiomtery, and that the delta phase is in fact only stable at sub-stoichiometry in the temperature range given in the phase diagram. Dissolved hydrogen greatly reduces the plasticity of zirconium, and zirconium hydrides are far more brittle than zirconium. [47] Guldner *et al.* [41] found that zirconium's interactions with hydrogen gas was completely reversible, and that the gas was completely liberated at approximately $800\,^{\circ}\mathrm{C}$. The combination of reversible absorption of hydrogen gas and embrittling effect of the absorption is found in a variety of metals, and is taken advantage of in the "Hydride-dehydride process" to create fine powders of ductile metals. First, hydrogen is absorbed to react the metal to metal hydride, which is subsequently milled to fine powder. Finally, the metal is heated to liberate the hydrogen gas, yielding a fine powder of metal with little impurities. [48] This method has been shown to be a successful way of synthesizing fine zirconium powders with few impurities [49].

Interaction with water

Previously, oxidation of zirconium by water was described by Eq. (2.14). However, this equation does not reflect the complexity of the reaction. The result of corrosion of zirconium can to some extent be viewed as zirconium reacting with both hydrogen gas and oxygen gas. Guldner *et al.* [41] found that zirconium absorbs water vapor at the same rate as it absorbs oxygen in the temperature range 250–300 °C. When raising the temperature, hydrogen gas is liberated and at 700–800 °C H_2 was formed directly during absorption. [41] During corrosion, the anode reaction occurs at the metal/oxide interface and can be described by

$$\begin{aligned} \mathrm{Zr} &\longrightarrow \mathrm{Zr}^{4+} + 4\mathrm{e}^- \\ \mathrm{Zr}^{4+} + 2\mathrm{O}^{2-} &\longrightarrow \mathrm{ZrO_2} \end{aligned} \tag{2.15}$$

Alternatively, if oxygen is dissolved in zirconium, the reaction at the anode can in Kröger-Vink notation be described by

$$\mathrm{v}_i^* + \mathrm{O}^{2-} \longrightarrow \mathrm{O}_i^* + 2\mathrm{e}^- \tag{2.16}$$

where v_i^* represents a neutrally charged interstitial vacancy and O_i^* represents a neutrally charged oxygen interstitial. The formation of oxygen anions, which occur at the oxide/water interface can be simplified to

$$2\mathrm{H_2O} \longrightarrow 4\mathrm{H}^+ + 2\mathrm{O}^{2-} \tag{2.17}$$

where reduction of the resulting protons is the cathode reaction. There are two possible reaction paths: The hydrogen is reduced and released as $H_2(g)$ at the oxide/water interface, or the protons are absorbed and conducted to the metal/oxide interface where they are reduced to form dissolved hydrogen. Lindgren *et al.* [50] investigated these possibilities by computational modelling. The study showed that the anode reaction is best described by Eq. (2.16) rather than Eq. (2.15) due to zirconium's ability to dissolve ZrO_2. It was found that the energetically preferred cathode reaction is absorption of hydrogen, which is supported by the findings of Guldner *et al.* [41] who indicated that the hydrogen in water practically behaves as hydrogen gas during absorption in zirconium. [50] [41]

2.5 Transition metal-silicon systems and intermetallics

The material in focus in this thesis – which is the transition metal silicide $ZrSi_2$ – is an intermetallic. Intermetallics are a type of alloy where the chemical, mechanical and physical properties may be completely different from both host material and alloying element. Most transition metals form silicides, while some form low eutectic alloys with silicon. Hg and Tl do not react with silicon. Chen *et al.* [4] describes the following mechanism in formation of transition metal silicides:

When Si atoms in transition metal silicides insert into the lattice of the transition metal, the d-atomic orbitals of the transition metal repel one another, a jumping level is reduced, and the d-band is narrowed. The resonance energy shifts to higher binding energy, which

causes the weakening of d-electron bonding strength and the loss of cohesive energy. In order to compensate for this loss, the energy states of Si and metal will inevitably couple, so that the formed state is closer than the original bonding states. These filled bonding orbitals lead to the strengthening of the bonds, which leads to the strong stability of metal silicides.

The formed metal-silicon bond have a strong influence on the electronic properties of the material. In addition, a silicon-silicon bond is formed, which decreases the valence state of silicon. The bonding mechanisms gives rise to unique electronic structures and geometries and the significant difference in properties from the component materials [4]. In most cases, these compounds have a defined stoichiometry and the transition metal silicides come in a wide array of stoichiometries and crystal structures [51].

In this section, two systems will be presented; the Mo-Si system, with special focus on $MoSi_2$, and the Zr-Si system with focus on $ZrSi_2$. Selected relevant properties of molybdenum, the Mo-O system, and the Mo-Si systems will be introduced followed by some characteristics of the Mo-Si system during SHS. The Zr-Si system will initially be introduced in terms of the binary phase diagram and some promising applications of zirconium silicides. Relevant properties of the zirconium silicides and the Zr-Si system will be presented in light of a review on characteristics of SHS in the Zr-Si system. Then, some possible high-temperature interactions between zirconium and silicon other than formation of zirconium silicides will be presented. Finally, a discussion of necessary precautions for preparation of Zr-Si powder mixtures will be done based on the discussions of SHS and the properties of zirconium and silicon. The Mo-Si system and $MoSi_2$ will be treated as a reference system and material where SHS is a feasible synthesis method, as SHS of $MoSi_2$ has been done on a commercial scale.

2.5.1 Molybdenum and the Mo-Si system

Properties of molybdenum

Molybdenum is a group VIa metal, who share several characteristics; they crystallize in the bcc ($Im\bar{3}m$) -structure, undergo a ductile-to-brittle transition at approximately $0.15T_m$, and form volatile oxides at elevated temperatures. [52] Molybdenum is in period 5, the same period as Zr, has a density of $10.2\,\mathrm{g\,cm^{-3}}$, and a melting point of $2623\,^{\circ}\mathrm{C}$. According to Klopp [52], this means that the ductile-to-brittle transition is at around $430\,^{\circ}\mathrm{C}$ (assuming kelvin is used in the $0.15T_m$ relation).

The Mo-O system

Molybdenum forms two main oxides, MoO_3 and and MoO_2[53]. The standard gibbs free energy of formation of the oxides are $-668\,\mathrm{kJ\,mol^{-1}}$ and $-533\,\mathrm{kJ\,mol^{-1}}$ [19]. Thus, molybdenum is readily oxidized at even ambient conditions, but not as readily as silicon and zirconium (see Table B1. The eutectic points involving these two oxides have been estimated both empirically and by thermodynamic modelling, and the results are shown in Table 2.1.

Table 2.1: Temperature of eutectic points involving MoO_2 or MoO_3 estimated either empirically or by thermodynamic modelling. The data is taken from Zhang *et al.* [54], where the empirical values were gathered from available literature and the thermodynamic modelling was done in the study.

Reaction	Temperature [°C]	Estimation method
$L = \mathrm{Mo} + \mathrm{MoO_2}$	2150 ± 150	Empiric
	2206	Thermodynamic modelling
$L = \mathrm{Mo_9O_{26}} + \mathrm{MoO_3}$	778 ± 15	Empiric
	786	Thermodynamic modelling

Volatilization of MoO_3 starts at temperatures above its eutectic point in a surplus of oxygen gas, and the boiling point is $1107\,^{\circ}\mathrm{C}$. [19] [54]

The Mo-Si system

The Mo-Si binary phase diagram at ambient pressure, taken from Mitra *et al.* [55], is shown in Figure 2.8

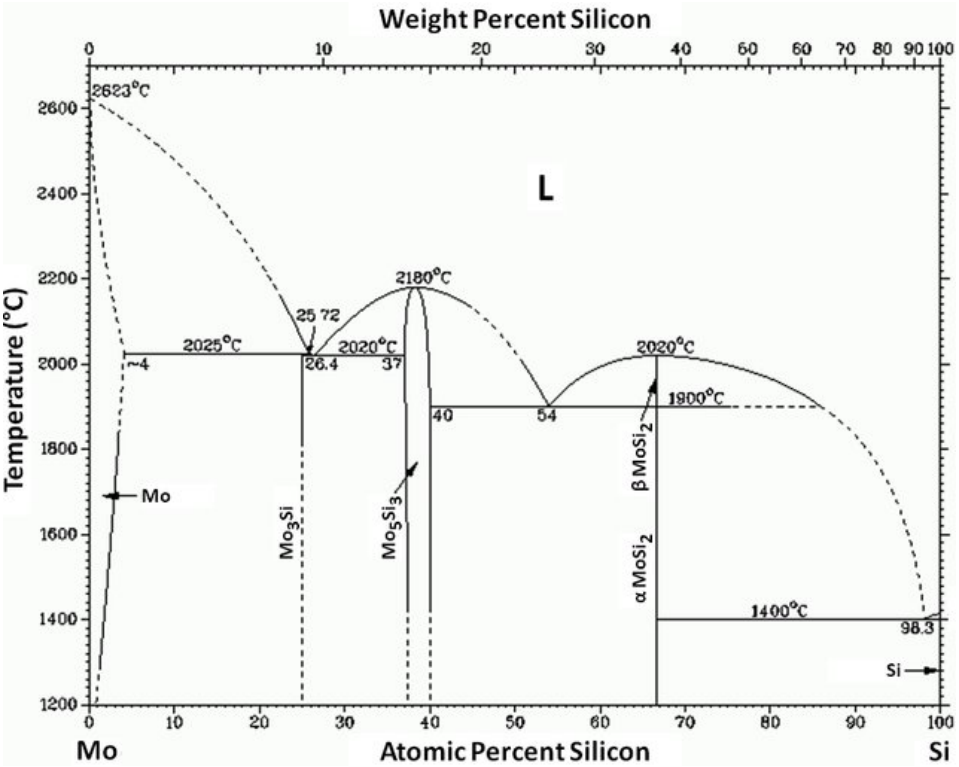

Figure 2.8: Phase diagram of the binary Mo-Si system at ambient pressure [55]

Figure 2.8 indicates that there are three stable molybdenum silicides: Mo_3Si, Mo_5Si_3, and $MoSi_2$. Mo_3Si and Mo_5Si_3 have cubic and tetragonal crystal structures respectively, and Mo_3Si decomposes peritectically at $2025\,^{\circ}C$ while Mo_5Si_3 melts congruently at $2180\,^{\circ}C$. $MoSi_2$ is polymorphic and goes from tetragonal to hexagonal at $1900\,^{\circ}C$ with increase in temperature, which subsequently melts congruently at $2020\,^{\circ}C$.

The adiabatic temperature of the combustion wave (see Eq. (2.7)) is $1650\,^{\circ}C$ [56], which is above the melting temperature of silicon and the silicon rich eutectic in Figure 2.8, but below the melting point of Mo and $MoSi_2$. Jo *et al.* [57] measured the combustion temperature to be $1731\,^{\circ}C$, which is higher than the adiabatic combustion temperature and therefore unlikely. No explanation for this observation is offered ind the article. Minasyan *et al.* [56] measured the combustion temperature to be about $1500\,^{\circ}C$ with dilution of both $10\,wt.\%$ and $13\,wt.\%$ Si. The dilution is expected to lower the combustion temperature, so it would probably be somewhat higher in an undiluted Mo+2Si mixture. It has been suggested that the reaction mechanism for formation of $MoSi_2$ is dissolution of molybdenum in molten silicon and subsequent precipitation of $MoSi_2$. At low hearing rates, the combustion reaction is preceded by formation of Mo_5Si_3, which then reacts with molten silicon to form $MoSi_2$. [57] [3] $MoSi_2$ was the first material synthesized by solid-state SHS, and has been synthesized commercially by SHS [21, p. 5] [8] $MoSi_2$ is ductile above $1000\,^{\circ}C$ and has an E-modulus of $400\,GPa$, it is a good thermal conductor and has an excellent oxidation resistance at high temperature. Its properties makes it viable for refractory applications or as a heating element. A severe disadvantage of $MoSi_2$ is PESTing, which is caused by formation of MoO_3 on the surface of the material in oxidizing atmospheres. As previously shown, MoO_3 is volatile at high temperatures, so oxidation at high temperature causes MoO_3 to evaporate and leave a surface layer of SiO_2. Hence, PESTing is not an issue at high temperature, and the resulting SiO_2-layer works as a protective layer on the material. MoO_3 not evaporating results in the oxide surface layer being porous, which provides an easy passage for oxygen diffusion. PESTing is most prominent at $500\,^{\circ}C$.

2.5.2 The Zr-Si system

Zirconium silicides

The content of this section is based on Dalene [6], with some edits and additions.

The zirconium-silicon phase diagram has been widely studied, and several binary phase diagrams have been proposed. Okamoto [58] assessed available experimental data in composing a phase diagram, which is shown in Figure 2.9. In literature, this phase diagram is widely accepted as the reference.

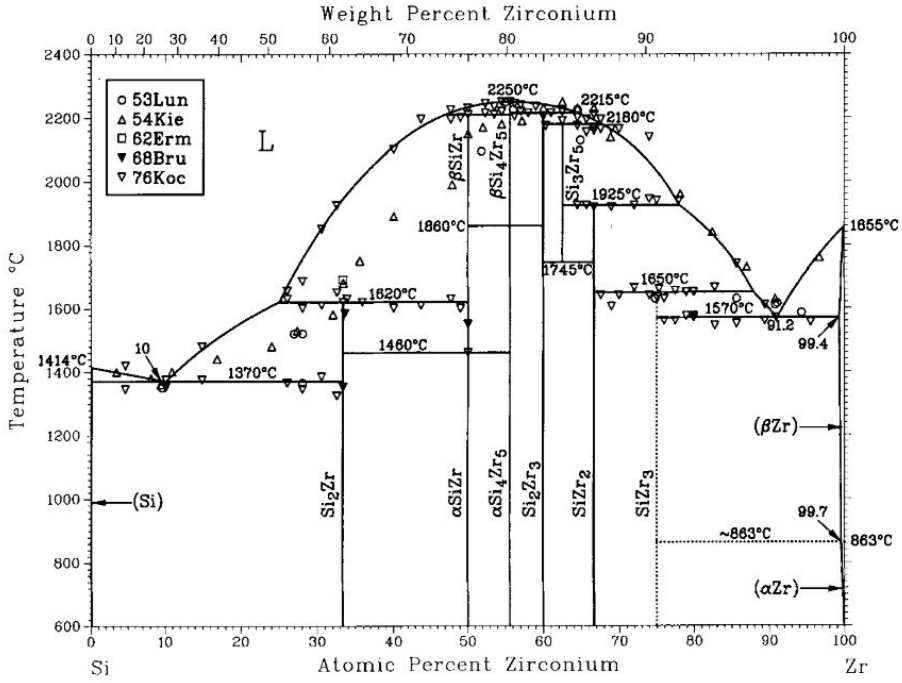

Figure 2.9: Widely accepted binary phase diagram of the Zr-Si system created by Okamoto [58] by assessing available experimental data

Early research indicates that the high-temperature phase Zr_5Si_3 may be stabilized if synthesized from zirconium containing nitrogen and oxygen [59]. Chen *et al.* [60] performed a thermodynamic assessment of the Si-Zr system, yielding a phase diagram that agrees well with the phase diagram presented by Okamoto [58]. [60] The phase diagram shows that there is a wide array of zirconium silicides. From the phase diagram, it is evident that $ZrSi_2$ is the lowest-melting compound.

Among the zirconium silicides, almost all research related to both their application and synthesis is devoted to $ZrSi_2$. However, compounds like ZrSi and Zr_3Si_2 may possibly be better candidates for refractory applications. Canel *et al.* [61] explored the use of zirconium silicide composites while Le Flem *et al.* [62] explored the use of Zr_3Si_2 in applications with temperatures exceeding the operational temperature of $ZrSi_2$. Yeom *et al.* [63] compared the oxidation of Zr_2Si, ZrSi, and $ZrSi_2$, revealing that $ZrSi_2$ exhibits the best passivation behaviour between the three. This result is further supported by a study of this passivation behaviour by Yeom *et al.* [2]. The study indicates that the formation of a thin, highly passivating oxide layer depends on spinodal decomposition of $ZrSi_2$, and silicon-rich regions. From stoichiometry $ZrSi_2$ should result in the largest amount of silicon-rich regions of all compounds in the Zr-Si system. $ZrSi_2$ is a viable candidate to replace $MoSi_2$ in applications where PESTing of $MoSi_2$ is a challenge. An application where $ZrSi_2$ is an unrivaled candidate is as a protective coating for zirconium cladding

material in certain types of nuclear reactors. The main advantages with $ZrSi_2$ in this application are the excellent corrosion-resistance and its strong adhesion to the ZrO_2-layer on the zirconium cladding. Such a coating would protect the cladding material from steam corrosion during a loss-of-coolant-accident where breakaway – which was presented in section 2.4.2 – causes the otherwise corrosion-resistant cladding to be rapidly oxidized by water vapor forming hydrogen gas in the process. These conditions caused the explosions in the reactor buildings at the Fukushima Daiichi nuclear power plant in 2011, so $ZrSi_2$ can be a part of the solution to the challenge of avoiding such disastrous consequences of a loss-of-coolant-accident. [5] [64] [65].

Silicothermic reduction

In this thesis, "silicothermic reduction" refers to reduction of ZrO_2 by silicon compounds which forms metal silicides. This may happen through the reaction

$$n\mathrm{ZrO_2} + (2n+m)Si \longrightarrow \mathrm{Me}_n\mathrm{Si}_m + 2n\mathrm{SiO\,(g)} \uparrow \tag{2.18}$$

Figure 2.10 shows the natural logarithm of the partial pressure of SiO from silicothermic reduction compared to the natural logarithm of the partial pressure of SiO at the Si-SiO_2 interface as a function of the inverse of temperature.

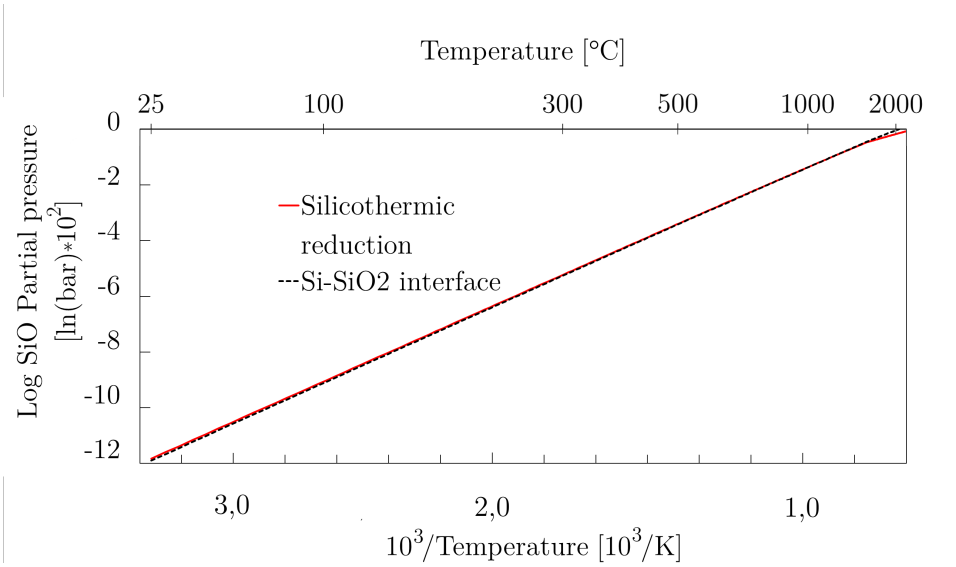

Figure 2.10: Gibbs free energy of the reaction in Eq. (2.18) with $n, m = 1, 2$ at discrete temperatures with 5 °C intervals collected from HSC Chemistry, and the partial vapor pressure of SiO(g), calculated at these temperatures based on estimation of chemical activity and the equilibrium constant of the reaction (see section A). The partial pressure is compared to the partial pressure of SiO at the Si-SiO_2 interface (see Figure 2.4)

The calculation indicates that the vapor pressure of SiO from silicothermic reduction is on the same magnitude as the partial pressure of SiO at the Si-SiO_2 interface at temperatures up to $2000\,^{\circ}\mathrm{C}$. This reaction was used by Tkachenko *et al.* [66] to synthesize zirconium silicides in a vacuum furnace, where synthesis of $ZrSi_2$ at $1400\,^{\circ}\mathrm{C}$ yielded the best results. The synthesis method is of little interest in large-scale application as it requires a continuous supply of heat, but the reaction may be important to consider as a parasitic reaction in combustion synthesis of zirconium silicides, and will be revisited in section 2.6.1.

2.6 Synthesis of zirconium silicides

2.6.1 SHS of zirconium silicides

The formation enthalpy of several phases in the Zr-Si seems to be unavailable in literature, and the phases where a formation enthalpy is estimated the value varies from reference to reference [67] [68]. Formation enthalpy values of the phases have been gathered from available literature, and are shown in Table 2.2. Note that values from Bertolino *et al.* [67] are converted from $\mathrm{kJ\,mol^{-1}}$ to $\mathrm{kJ\,(mol\ of\ atoms)^{-1}}$, given that there are x+y mol of atmos in one mol of Zr_xSi_y, and that values from Shu *et al.* [68] were estimated by examining Figure 1 in the article.

Table 2.2: Formation enthalpy values of the phases in the Zr-Si gathered from available literature. Note that values from Bertolino *et al.* [67] are converted from $\mathrm{kJ\,mol^{-1}}$ to $\mathrm{kJ\,(mol\ of\ atoms)^{-1}}$, given that there are x+y moles of atoms in one mol of Zr_xSi_y, and that values from Shu *et al.* [68] were estimated by reading of Figure 1 in the article

Phase	$\Delta_f H^{\ominus}$ [$\mathrm{kJ\,(mol\ of\ atoms)^{-1}}$]			
	Weast [69] (via Bertolino *et al.* [67])	Topor *et al.* [70]	Meschel *et al.* [71]	Shu *et al.* [68]
Zr_3Si	-54.43	-	-	
Zr_2Si	-69.77	-	-	-76
Zr_5Si_3	-71.69	-71.7 ± 4.8	-	-80.5
Zr_3Si_2	-77.00	-	-	-88.5
Zr_5Si_4	-	-	-91.9 ± 1.9	
ZrSi	-77.40	-	-94.5 ± 2.3	-93.5
$ZrSi_2$	-53.00	-	-60.3	-63

The work done by [67] showed that zirconium silicides can be synthesized by SHS from zirconium and silicon, and more recent studies have explored synthesis of zirconium silicides from a thermite type reaction (see Eq. (2.2)) with magnesium as reducer and ZrO_2 as the metal oxide [72]. The focus in this section will be on SHS from zirconium and silicon powders. First, the reaction stages during SHS in the system will be discussed in view of the synthesis stages discussed in section 2.2. Then, the influence of the reactant properties

on the synthesis will be discussed, which will be the basis of a discussion on the required pre-treatment of the green reactive mixture before synthesis.

Reaction stages in SHS

In section 2.2, the SHS-process was divided into heating, ignition, and propagation. In this section, the behaviour of the Zr-Si system during these stages will be discussed based on available literature and previous work and discussions from [6]. As of the heating techniques discussed in section 2.2, it is important to consider that silicon is only a semiconductor, which will have an effect on direct resistive heating, inductive heating, and microwave heating. Since zirconium is electrically conductive, and the charge carrier density in semiconductors increase with temperature, the techniques would heat a Zr-Si mixture, but with poor efficiency at low temperature since the contribution from silicon is low. In fact, both PCACS and HFIHCS (see section 2.1.2 have been utilized to synthesize dense $ZrSi_2$ [10] [11]. During heating of a Zr-Si mixture, preceding work for this thesis in Dalene [6] found that solid-state diffusion will form layers of Zr_2Si, ZrSi, and $ZrSi_2$ between the zirconium and silicon particles. These findings are supported by the finding of Bertolino *et al.* [67], and the formation of these phases may have an effect on both the final product, and the propagation of the reaction which will be discussed later.

Table 2.3 shows the melting point, and the combustion temperature of the corresponding Zr-Si mixture of the phases in the Zr-Si system measured by Bertolino *et al.* [67]. They emphasize that the measurements were done with a pyrometer on the surface of each sample, and that the resulting temperatures are a lower limit since the the bulk of the samples are hotter than the surface and there is a fairly large uncertainty related to pyrometer measurements.

Table 2.3: The formation enthalpy of the phases in the Zr-Si binary system, the measured combustion temperature during SHS of a Zr-Si powder mixture with stoichiometry corresponding to the zirconium silicide phase, and the melting point of each phase. The table also includes the melting points of zirconium, silicon, and the zirconium-rich and silicon-rich eutectic points in the Zr-Si system. Note that not all of the phases melt congruently, but some form a eutectic with another phase or decompose peritectically to another phase and a liquid

Phase	T_{ad} [67][°C]	T_c of corresponding mixture [67] [°C]	T_m [°C][58]
Zr_3Si	-	1792	1650
Zr_2Si	2394	1698	1925
Zr_5Si_3	2483	1975	2180
Zr_3Si_2	-	1869	2215
Zr_5Si_4	-	1757	2250
ZrSi	2649	1830	2210
$ZrSi_2$	1963	1405	1620
Zr	-	-	1857
Zr-rich eutectic	-	-	1570
Si	-	-	1412
Si-rich eutectic			1370

In Dalene [6], it was found that a Zr+2Si powder mixture ignited after an endotherm reaction at around $1356\,^{\circ}\mathrm{C}$. Based on the expectation that ignition is related to formation of a liquid and the values in Table 2.3, it seems that formation of the silicon-rich eutectic causes the mixture to combust. This is supported by the findings of Bertolino *et al.* [67], and it is reasonable to assume that this is the ignition point of all Zr-Si mixtures, and not only Zr+2Si mixtures.

In order for the combustion to propagate, the combustion temperature must be above the ignition temperature of the mixture. From table Table 2.3, it is evident that Zr-Si mixtures with a Zr/Si -ratio corresponding to the stoichiometry of a phase in the system had a measured combustion temperature above the ignition temperature measured by Dalene [6]. The Zr+2Si mixture had the lowest combustion temperature, and is only about $50\,^{\circ}\mathrm{C}$ above the ignition temperature. The low difference between combustion temperature and ignition temperature was reflected by the work Bertolino *et al.* [67], who found that the combustion temperature was too low to make propagation possible with a diluent added to the mixture. This made them unable to measure the activation energy by the method presented in section 2.2.3, but they were able to do the experiment with a 5Zr+3Si mixture. The resulting activation energy confirmed that a solid-solid process is not involved in control of the SHS process.

This conclusion by Bertolino *et al.* [67] is reflected by Table 2.3, which may also suggest which phases are formed in the combustion front and which are formed in the zones behind the combustion front (see section 2.2.3). If one or more phases whose stoichiometry does

not correspond to the Zr/Si-ratio in the initial mixture are formed in the combustion front, achieving a monophasic product will rely on complete re-reaction of these phases behind the combustion front. This does in turn rely on a slow enough cooling rate. Considering only the information in Table 2.3, several of the phases could be formed in the combustion wave of a multitude of Zr-Si mixtures. If the melting point of a phase is lower than the combustion temperature, it will be formed behind the combustion front. Otherwise, it may be formed in the combustion front. Whether a phase is formed in the combustion front may be of great important to both the combustion wave itself and the final product: The heat generated in the combustion wave is dictated by which phases are formed there. However, Bertolino *et al.* [67] conclude from their work that the main process of the combustion wave in Zr-rich mixtures is formation of Zr_5Si_3, and that it is formation of ZrSi in Si-rich mixtures with the exception of mixtures corresponding $ZrSi_2$ where $ZrSi_2$ is formed directly in the combustion wave. They attribute this to reaction kinetics. Thus, synthesis of ZrSi and $ZrSi_2$ has the advantage that the desired product is formed directly in the combustion wave, and this is reflected by the results of the SHS-experiments by Bertolino *et al.* [67] which show synthesis of ZrSi and $ZrSi_2$ gave the purest products. They also conclude that the reaction that occurs between zirconium and silicon is a solid-liquid reaction in the combustion wave of a mixture corresponding to $ZrSi_2$ and probably also in a mixture corresponding to Zr_2Si, and a liquid-liquid reaction in the mixtures corresponding to the rest of the phases in the Zr-Si system.

Formation of zirconium silicides from zirconium and silicon will cause a volume reduction. This is illustrated in Table 2.4, which lists densities of some zirconium silicides taken from Shu *et al.* [68], and the volume reduction as percent loss of initial volume.

Table 2.4: Densities of some zirconium silicides taken from Shu *et al.* [68], and the volume reduction as percent loss of initial volume.

Phase	Density [$\mathrm{g\,cm^{-3}}$]	Volume reduction [$\%$ loss of xZr+ySi volume]
Zr_2Si	6.055	14
Zr_5Si_3	5.821	13
Zr_3Si_2	5.852	15
α-ZrSi	5.585	19
β-ZrSi	5.609	19
$ZrSi_2$	4.866	21

Table 2.4 shows a significant reduction in volume, that increases with Si-content in the phase. This reflects the description of the mechanism of transition metal silicide formation, which states that *silicon inserts into the Zr-lattice*. The volume reduction is an important reason to why external pressure is needed during SHS to achieve a dense product as this increases the porosity during synthesis, which was reflected in the results in the preceding work for this thesis [6]. The formation of zirconium silicides by solid-state diffusion before ignition may have a substantial negative effect on the propagation of the combustion, especially in synthesis of $ZrSi_2$. $ZrSi_2$ formed by solid-state diffusion will act as an inert diluent. Zr_2Si and ZrSi may be reacted further with molten Si in the combustion wave

to form $ZrSi_2$. The possible impact on the heat generated in the combustion wave may be illustrated by the reaction enthalpy of $ZrSi_2$ from molten Si and Zr_2Si or ZrSi versus the reaction enthalpy by formation from Zr and Si. The estimated reaction enthalpy of these reactions at $1405\,^{\circ}\mathrm{C}$ (measured combustion wave temperature in Zr+2Si mixture, see Table 2.3) and adjusting for 1 mol of produced $ZrSi_2$ is shown below

$$\mathrm{Zr} + 2\mathrm{Si} \longrightarrow \mathrm{ZrSi_2} \qquad \Delta_r H(1405\,^{\circ}\mathrm{C}) = -269\,\mathrm{kJ} \tag{2.19}$$

$$\frac{1}{2}\mathrm{Zr_2Si} + \frac{3}{2}\mathrm{Si} \longrightarrow \mathrm{ZrSi_2} \qquad \Delta_r H(1405\,^{\circ}\mathrm{C}) = -134\,\mathrm{kJ} \tag{2.20}$$

$$\mathrm{ZrSi} + \mathrm{Si} \longrightarrow \mathrm{ZrSi_2} \qquad \Delta_r H(1405\,^{\circ}\mathrm{C}) = -57\,\mathrm{kJ} \tag{2.21}$$

assuming pure molten Si instead of Si-rich eutectic, and using data on total enthalpy of each compound from HSC Chemistry. In the relevant time-scale, solid-state diffusion will only form minor amounts of zirconium silicides, and far from completely consuming the available Zr, but Eq. (2.19) Eq. (2.20) Eq. (2.21) may still be an illustration of how solid-state diffusion reduces the exothermicity of the mixture and hence may reduce the temperature of the combustion front. Additionally, as none of these silicides or zirconium particles melt at the Zr+2Si combustion wave temperature (see Table 2.3) they may also act as a diffusion barrier between the molten silicon and zirconium particles.

There are three relevant gas-evolving parasitic reactions; formation of $SiO(g)$ at the Si/SiO_2-interface (see section 2.3.2), release of dissolved hydrogen in zirconium (see section 2.4.3) and silicothermic reduction of ZrO_2 (see section 2.5.2). As all these processes are endothermic, they will consume some of the reaction heat generated in the combustion wave. Generally the hydrogen concentration is low, so the release of hydrogen is not expected to participate in the main combustion reaction or have a significant effect on the synthesis. The SiO-forming reactions may on the other hand have an effect, and if the reactivity of these processes is high enough, it may result in destabilization of the propagation wave. Available literature does not discuss the effect from these reactions on SHS of $ZrSi_2$.

There are some important similarities between SHS of $MoSi_2$ (see section 2.5.1) and of $ZrSi_2$. First of all, both have an adiabatic combustion temperature ($1650\,^{\circ}\mathrm{C}$ for $MoSi_2$ and $1963\,^{\circ}\mathrm{C}$ for $ZrSi_2$) and a measured combustion temperature ($1731\,^{\circ}\mathrm{C}/1500\,^{\circ}\mathrm{C}$ for $MoSi_2$ and $1405\,^{\circ}\mathrm{C}$ for $ZrSi_2$) below the melting point of the product and the melting point of the transition metal, but above the melting point of silicon and the silicon-rich eutectic. Therefore, the reaction in the combustion front of both system happens in a silicon melt. However, there is a substantial difference in mechanism; $MoSi_2$ is thought to be formed by dissolution of molybdenum in the silicon melt and subsequent precipitation of $MoSi_2$. $ZrSi_2$ however is thought to be formed by reaction between solid zirconium and a silicon-rich eutectic. This difference can be attributed to the difference in the phase diagrams of the systems; The Mo-Si system has a eutectic point at $54\,\mathrm{at.\%}$ Si and $1900\,^{\circ}\mathrm{C}$. This is somewhat above the combustion temperature in the system, but may close enough to be formed in a short time-frame at ideal conditions and thus make the molten silicon able to dissolve the molybdenum. The Zr-Si system does not have a corresponding eutectic. This is reflected in findings that indicate that combustion formation of $MoSi_2$ has low sensitivity to the particle size of the molybdenum, while coarse zirconium particles affect the combustion formation of $ZrSi_2$. It may also explain why the difference between adi-

abatic and real combustion temperature is much higher in $ZrSi_2$ than in $MoSi_2$ since the the dissolution-precipitation mechanism is likely to be more efficient than the solid-liquid mechanism [57] [67].

Reactant considerations

Figure 2.3 suggests that variations in mixture composition, reactant particle sizes, and the sample density affects the combustion temperature and the combustion wave velocity. Variations from ideal mixture composition will occur if the mixture is inhomogeneous. Larger particles means less reaction surface, and Bertolino *et al.* [67] found that due to the combustion temperature in Zr+2Si mixtures being far below the Zr-rich eutectic, coarse Zr particles may not be fully reacted. The amount of oxide present on the zirconium and silicon particles may also have an effect on both reactivity and the final product. The $SiO(g)$-producing reactions discussed in the previous paragraph are caused by presence of either SiO_2 or ZrO_2, and will reduce the silicon/zirconium ratio in the reactive mixture if they occur. Eq. (2.12) shows that silicon is consumed to reduce SiO_2. From the reaction in Eq. (2.18) it is evident that the necessary silicon/zirconium reactant ratio is larger than the silicon/zirconium ratio in the produced silicide if this reactions occurs. An advantage of these reactions is that they reduce the amount of oxide in the mixture, and therefore increase the purity of the product. Also, the reduction in the silicon/zirconium ratio can be accommodated by adding a surplus of silicon in the initial mixture. However, finding the exact amount of oxide in the reactant powders is tedious, and it may also be difficult to predict the yield of these reactions due to the rapid changes in temperature during the synthesis. As discussed in section 2.3.2 and section 2.4.2, the oxide layers on both silicon and zirconium make them relatively inert at ambient temperatures. Since melting of silicon is proposed to be the initiation of combustion, it may be expected that the silicon oxide layer is unable to shield the silicon from zirconium. Due to the high temperature and rapid temperature increase during combustion, the zirconium oxide layer may crack due to phase transformations as discussed in section 2.4.2. Thus, the oxide layers are not expected to shield silicon and zirconium from reacting.

Required pre-treatment

Some of the content in this paragraph is based on Dalene [6].

As the discussed in the previous paragraph, degree of homogeneity, powder particle size, mixture density, and oxide content influences the synthesis.

An efficient technique to both reduce powder particle size and achieve a homogeneous mixture is to mill the powders together, by ball milling or attrition milling, where attrition milling is faster than ball milling and can easily be performed in an inert atmosphere [73, p. 422-426]. A variety of the ball mill, the planetary ball mill, can obtain more complex movement patterns since the container both rotates around its own axis and around the axis of the base. This results in higher intensities of forces applied to the powder particles. However, these mills are only used at a laboratory or pilot scale [74]. Fine milling may even make the powder particles more reactive, which is called mechanical activation. It is

possible to ignite an SHS-viable mixture by only high-energy milling. This technique is called mechanochemical synthesis, and will be presented in more detail in section 2.6.2.

Some special characteristics of the milling arise from the fact that zirconium is ductile and silicon is brittle (see Table B1). At certain milling conditions, the zirconium will be flattened and deformed while the silicon is crushed, and they may form laminated composites. This may be an advantage in terms of activation, but the flattened shape of the zirconium particles may affect the flow properties, compaction abilities and homogeneity of the mixture. [21, p. 34] As molybdenum also is ductile at normal milling conditions (see section 2.5.1), co-milling of Mo-Si mixtures share the same characteristics.

The milling can be done wet or dry, where both techniques have advantages over each other that are important to consider in the context of mixing precursor powders. Wet milling obtains smaller particle sizes and better homogeneity. However, wet milling cause more wear on the milling media and lining, which is a disadvantage both in terms of cost of equipment and the purity of the mixture [73, p. 424]. When dry milling, an atmosphere of inert gas can be chosen to ensure that the powders do not oxidize, or even explode as was presented as a possibility with silicon in section 2.3.1. During wet milling, a liquid that does not react with the powders must be chosen. Isopropanol is found not to react with silicon powders even when milled down to nanoscale [75], and is already used to wet mill silicon on a large scale [76]. Preceding work for this thesis found that zirconium may also be milled in isopropanol without reacting [6]. In addition, the powder must be dried before combustion synthesis if wet-milled. The drying process is not necessarily a disadvantage as the powder can be dried by spray drying. In this technique, the slurry produced by wet milling is sprayed to small droplets by a nozzle into a chamber where a gas dries the liquid, and the powder mixture agglomerates and falls into a collector at the bottom of the drying chamber. The process results in a uniform, free-flowing powder which may be a large advantage in further processing [73, p. 439-440].

In previous discussions, the amount of oxide in the powders was proposed to have a negative effect on the synthesis. Milled zirconium and silicon powder particles will have had their oxide layer cracked, and hence they are subjected to further oxidation after milling. Therefore, if the powder mixture is extensively milled it might be necessary to keep the powder under inert atmosphere between milling and synthesis, which may be an engineering challenge if further pre-treatment like pressing is required.

A powder product can be achieved by using the uncompacted powder mixture directly. The result is a porous sintered body that is easily milled. More compact products can be achieved by pressing the green mixture before combustion. For metal-nonmetal systems, the achieved density is 40–$80\,\%$ of theoretical density [8]. As shown in Figure 2.3, a higher density also increases the propagation velocity.

2.6.2 Alternative methods

Mechanochemical synthesis

In this synthesis route, powders are milled in a planetary mill. As the powders are milled, crystallite size is reduced and stress is introduced, to the extent that the activation energy

of reaction between the powders is lowered. In exothermic systems like the Zr-Si system, the heat of reaction can be large enough to heat unreacted powder to ignition and reaction, causing a self-propagating reaction. This is analogous to combustion synthesis, except that the energy needed for ignition is supplied mechanically instead of thermally. This synthesis has been done successfully both from elemental powders and through metathesis, which in this case is formation of zirconium silicide and an alkaline earth metal halide from zirconium halide and alkaline earth metal silicide, for example:

$$\mathrm{ZrCl_4(s) + 2CaSi\,(s) \longrightarrow ZrSi_2(s) + 2CaCl_2(s)}$$

Mechanochemical synthesis can produce powder with a particle size on the nanoscale. In general, the synthesis is time consuming and requires a large energy input. Mechanochemical synthesis from elements requires non-stop intensive milling to obtain a pure product, which increases wear and introduces impurities. Milling can be paused in the metathesis approach, but the reaction in this approach is not self-propagating, which means an even larger energy input is required [77] [78].

Arc melting

In this synthesis route, precursors are melted by an electric arc. By considering the phase diagram of the Zr-Si system (see Figure 2.9), each compound can be made in thermodynamic equilibrium by controlling temperature and the composition of the mixture [4]. However, evaporation of silicon causes a large shift in stoichiometry, and additional heat treatment may be required to purify the product from secondary zirconium silicide compounds [61].

Reaction sintering

In this synthesis route, Zr- and Si -powders are reacted and sintered in one process. The process involves simultaneous solid-state reactions and sintering performed at high temperatures below the lowest melting point in the system. A dense product can be achieved by simultaneous application of pressure during heat treatment [61]. This synthesis was explored by Canel *et al.* [61] with a 1:1 Zr-Si stoichiometry. A shell-like composite of Zr_2Si, ZrSi, and $ZrSi_2$ was obtained, similar to the products of solid-state diffusion observed in the preceding work for this thesis [6]. It proved to be difficult to obtain a pure product, and the process is time consuming as reactions only occur in solid-state.

Electrochemical reduction of $ZrSiO_4$-SiO_2

Liu *et al.* [79] produced pure $ZrSi_2$ in form of nodular particles by reducing sintered pellets of a mixture of $ZrSiO_4$ (zircon) and SiO_2. These precursors are cheaper than Zr and Si. However, a sintered pellet was needed, and the synthesis was performed in molten CaCl-NaCl for 15 hours, which is time and energy consuming. In addition, a graphite anode was consumed, producing CO and CO_2.

Silicothermic reduction of ZrO_2

Tkachenko *et al.* [66] produced zirconium silicides from reduction of ZrO_2 by Si by the reaction in Eq. (2.18).

The synthesis was done by pressing ZrO_2 and Si pressing and subsequently heating the pellet in a graphite cartridge for 1 hour. The best result was achieved by heating at $1400\,^{\circ}\mathrm{C}$, but the reaction is incomplete and there are carbon-impurities in the product.

3 Experimental

In this chapter, the chemicals and apparatus used in the experimental work in this thesis will be presented first. Then, experiments done to characterize the received powder and to study the effects of co-milling zirconium and silicon will be presented. Before the SHS-experiments are presented, the pre-experimentation that was done during the development of an experimental set-up for SHS synthesis will be presented, along with the results of these pre-experiments. Finally, experiments on silicothermic reduction and reactivity between zirconium silicides and zirconium and silicon will be presented.

3.1 Chemicals and apparatus

The received zirconium and silicon powders used in the experiments are shown in Table 3.1

Table 3.1: The table shows the properties of the chemicals used in this project, and how they are referred to in this report (See section F for more data). Note that the silicon content in silicon powder is measured by the amount of expected impurities, and that surface oxide is omitted [80]

Notation	d50 [µm]	Particle size 99 % [µm]	Purity [wt.%]	Manufacturer
Si(<75)	17.85	$<75\,\mu m$	99.9 %	Elkem Bremanger
Si(10-75)	29.22	10–75 µm	99.7 %	Elkem Bremanger
Si(40-100)	Unknown	40–100 µm	99.7 %	Elkem Bremanger
Zr-powder	60.60	$<180\,\mu m$	99 %	Lipmann Walton & Co Ltd

The apparatus and chemicals used in the experimental work are shown in Table 3.2.

Table 3.2: The apparatus used during the experiments, and how they are referred to in the text

Apparatus/chemical	Information	Application
Uniaxial Press	Mäder Pressen S3-S40 HV	Pressing pellets
CIP (cold isostatic press)	Autoclave Engineers (max. 29000 psi)	Post pressing pellets
Rotavapor	BÜCHI Rotavapor R-210	Used for drying of attritor-milled powder mixtures
Tube Furnace	Entech ETF 15 Horizontal Tube Furnace	Heat treatment, SHS synthesis chamber
DSC/TGA apparatus	NETZSCH STA 449 F3 Jupiter	TGA/DSC-measurements of samples up to $1500\,^{\circ}\mathrm{C}$ in argon atmosphere
Epoxy mould	Struers EpoFix Resin Struers EpoFix Hardener	Moulding SEM-samples
RotoPol Polisher	Struers RotoPol-31 Struers RotoForce-4 Struers RoDos	Lubricated polishing of epoxy mounted samples. Base rotating at 150 rpm with rotating sample holder and lubricant doser
$30\,\mu\mathrm{m}$ SiC paper	Struers Silicon Silicon Carbide Grinding Paper, particle size $30\,\mu\mathrm{m}$	Rough polishing of epoxy mounted SEM-samples
MD-Dur polishing cloth	Struers MD-Dur woven silk polishing cloth	Fine polishing of epoxy mounted SEM-samples
Lubricant	Struers blue lubricant (Ethanol, Ethanediol, isopropanol, blue dye)	Lubrication used during polishing of SEM-samples
X-ray diffractometer	Bruker D8 Focus X-ray diffractometer	XRD, $\Theta : 2\Theta$-configuration, fixed divergence slit, and Cu Kα radiation

Continued on next page

Apparatus	Information	Application
ZEISS SEM	ZEISS Ultra-55 Scanning Electron Microscope	SE-imaging of powder samples
HITACHI SEM	HITACHI S-3400N OXFORD INSTRUMENTS X-MAX $80\,\mathrm{mm}^2$	BSE-imaging and EDS of samples. Equipped with Silicon drift detector with $80\,\mathrm{mm}^2$ active area for EDS
IR-thermometer	Peak 4960 IR-thermometer	Measurement of temperature in filaments

3.2 Characterization methods

3.2.1 Characterization by XRD

A general approach was used when characterizing powder samples by XRD. The step size was for $0.01°$ for all samples, but the range of diffraction angles and time per step varied from experiment to experiment. After XRD the present phases were determined by comparing the diffractogram peaks to the peaks reported in literature of probable phases. Bruker Eva was used for this purpose, and the reference used for each phase is listed in Table 3.3

Table 3.3: Reference XRD-peaks used to qualitatively determine the present phases in powder samples from the diffractograms obtained in this thesis

Phase	PDF number
α-Zr	PDF 04-008-1477
δ-$ZrH_{(2-x)}$	COD 154039
ϵ-ZrH_2	PDF 01-071-4972
γ-ZrH	PDF 04-018-4122
α-ZrO_2	PDF 01-071-5577
Si	PDF 00-027-1402
SiC	PDF 04-006-7620
Fe_2O_3	PDF 00-039-1346
Zr_2Si	PDF 04-001-0938
Zr_5Si_3	PDF 04-004-7269
Zr_3Si_2	PDF 04-004-7162
α-ZrSi	PDF 04-005-9809
β-ZrSi	PDF 01-072-2031
$ZrSi_2$	PDF 00-032-1477
α-Mg	PDF 04-013-4129
BaO_2	PDF 04-008-6535
$BaCO_3$	PDF 00-041-0373

When the quantity of the present phases was of interest, the composition was estimated by doing a combined Pawley and Rietveld refinement in the Bruker TOPAS software. Pawley refinement was done by adding the the space group and lattice parameters of each phase – but no information on atoms and their coordination – and then refining by first varying sample displacement, then gradually the lattice parameters and crystallite sizes of the added phases. When a sufficient refinement was achieved, the structure of each phase was added. The structures were in most cases gathered from Jain *et al.* [81], with some exceptions where they could not be found there. These exceptions where specifically the phases δ-$ZrH_{(2-x)}$ and γ-ZrH, where the structures were made based on data from Maimaitiyili [82], and Zr_3Si_2, where the structure was made based on data from BOYKO *et al.* [83]. The lattice parameters and crystallite sizes obtained during the Pawley refinement was added to the loaded structures, and initially only the amount of each phases was varied during the refinement. Then, lattice parameters and crystallite sizes was gradually refined for each phase. In some cases, preferred orientation and strain was refined to get a better fit (strain was only refined for α-Zr). This what Rietveld refinement refers. However, the only parameters that will be reported are composition, and Rwp and GOF which describes the quality of the fit. The exact composition will not be utilized in interpretation of the results, but will rather be used as an indication of the magnitude of presence of each phase.

3.2.2 Characterization by SEM

Both powder samples for SEM-imaging in SE-mode and moulded samples for SEM-imaging in BSE-mode and characterization by EDS were prepared during the work in this thesis. The powder samples were prepared by laying out and spreading the powder on aluminium foil to avoid large agglomerates, before a piece of carbon tape was pressed down on the powder. Air was blown on the graphite tape to blow of excess powder. The sample was then put in a drying furnace to dry of moisture before imaging. The moulded samples were prepared by moulding a piece of a pellet in epoxy, and polishing the surface after hardening to expose a flat cross-section of the piece. The sample was polished down to a desired cross-section by $30\,\mu\mathrm{m}$ SiC-paper. Then, the grooves from this polishing was attempted to be polished away with MD-Dur polishing cloth. The duration of polishing with the SiC-paper varied from 2–$6\,\mathrm{min}$ between samples, but the polishing with the MD-Dur cloth was $30\,\mathrm{min}$ for all samples. All polishing was done with both base and sample-holder rotating counter-clockwise, and with an applied force of $5\,\mathrm{N}$.

3.3 Co-milling of zirconium and silicon

In order to study the feasibility of co-milling zirconium- and silicon powder as a route to obtain a homogeneous powder green reactive mixture of zirconium and silicon, zirconium and silicon powder was milled in an attritor mill using zirconia balls as milling media and isopropanol as dispersant. Before the milling, the powders were characterized by XRD and SEM in SE-mode as received. The XRD characterization was done over a 2θ-range of 10–$90°$ with 1.8 per step for the silicon powders for both the silicon powders and the zirconium powder.

The Si(10-75)-powder was chosen, as it was expected to resemble the zirconium powder the most in terms of particle size distribution. The first milling was done with $5\,\mathrm{mm}$ diameter zirconia balls, while the second was done with $2\,\mathrm{mm}$ zirconia balls. Additionally, the container the first milling was done in was over twice the volume as the container the second milling was done in. The milled mixtures were qualitatively characterized by XRD and imaged by SEM in SE-mode.

3.4 Pre-experiment: Development of SHS reactor

Some of the experiments on SHS in this thesis required a way to heat part of a precursor pellet to ignition in a room-tempered argon atmosphere. It was decided to attempt to achieve this by modifying available apparatus. The tube furnace was chosen as a basis for the reactor, as this can create both vacuum and argon atmosphere, and also sustain high temperatures up to $1500\,°\mathrm{C}$. Even though the mixture may reach a higher temperature during combustion (see section 2.6.1), the volume of the furnace and the flux of argon was considered sufficient to keep the furnace from overheating during synthesis with the chosen sample sizes. Resistive heating through a filament was initially chosen as the source of heat in the SHS-reactor. Not only was a filament required for heating, but it was also chosen as the conductor inside the furnace since regular electrical copper-wires are not

designed to withstand the potential temperature during synthesis. This required a way of conducting an electrical current into the furnace, which was done by designing and making a new flange for one of the furnace sides. The flange was made with a gas outlet, an input for a thermocouple and a input for electrical conductors (see section C for drawings of the flange). However, rough estimates of the possible voltage drop and subsequent temperature increase across the filament suggested it would be difficult to reach temperatures above 1000 °C. To be able to reach the ignition temperature of Zr-Si mixtures - estimated to be between 1350–1400 °C (see section 2.6.1) - a chemical igniter in combination with the filament was proposed. A schematic of the SHS set-up is shown in Figure 3.1

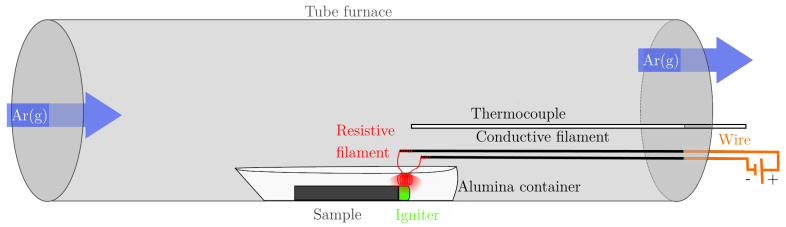

Figure 3.1: Schematic of the chosen set-up for the SHS experiments. “Sample” refers to a pressed pellet of a Zr-Si powder mixture, “Igniter” refers to a chemical igniter, *i.e.* highly exothermically reactive powder mixture, “Alumina container” may be any alumina container that fits the purpose, here represented by an alumina ship

Some experiments were performed to test the performance of the filament and the igniter. Since the results of these experiments affected the final reactor design and thus the SHS experiments presented in section 3.5, they will be presented in this section and not in chapter 4.

3.4.1 Resistive heating

To maximize the voltage drop and thereby the heat generation across the heating filament, two ways to maximize the difference in electrical resistance between conductive and heating filaments were tested; intertwining the heating filament with another filament with lower resistance for conduction, or having a continuous filament where the voltage drop is

created by polishing down the cross-sectional area of a part of the filament. A sample of each of the two designs is shown in Figure 3.2

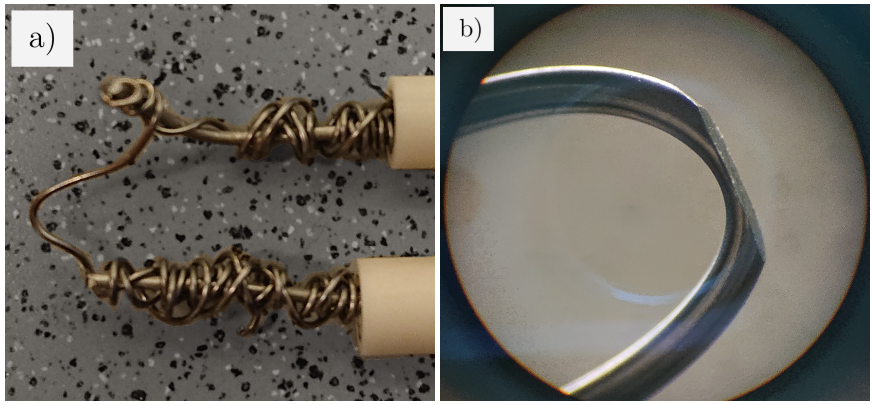

Figure 3.2: The two proposed filament designs for use in the SHS reactor. a) shows $1\,\mathrm{mm}$ 8020NiCr filament used for conduction intertwined with $0.4\,\mathrm{mm}$ Kanthal A filament for heating. b) shows the polished tip of a $1\,\mathrm{mm}$ 8020NiCr filament

The designs shown in Figure 3.2 were tested in a fume hood by passing a current with tuned voltage and amperage through them. The temperature in the filament was initially measured with a thermocouple. Temperature measurements were taken at approximately $5\,\mathrm{mm}$ from the filament, and in thermal contact with alumina in-between to insulate the thermocouple from the electrical current. The set-up is shown in Figure 3.3.

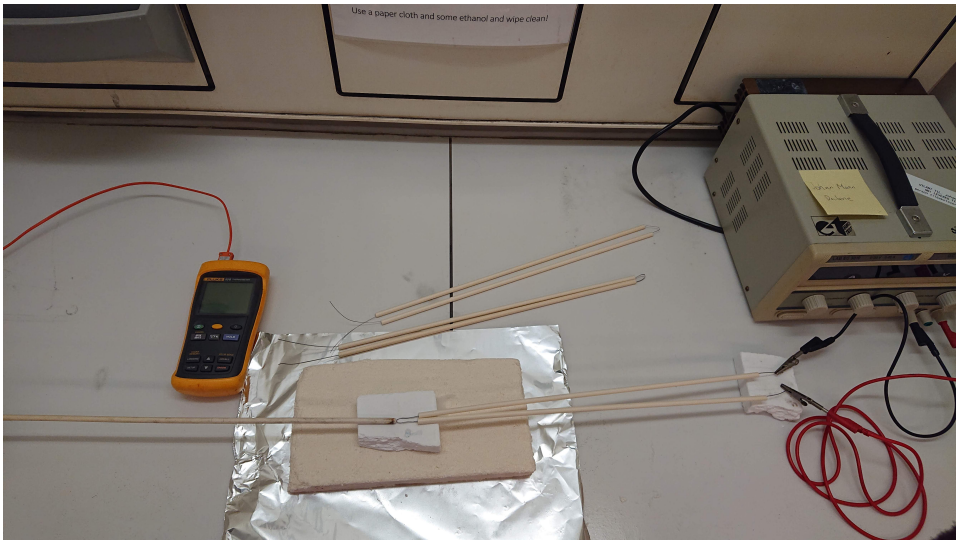

Figure 3.3: The experimental set-up for testing the heat generation in the two filament designs presented in Figure 3.2

The measured temperature did not exceed around $50\,^{\circ}\mathrm{C}$, even though glow in the filament was observed on multiple occasions. The seemingly low temperature measurements were attributed to insufficient thermal contact, which would be difficult improve while keeping the thermocouple electrically insulated from the filament. An IR-thermometer (see Table 3.2) was eventually utilized, but before that observation of glow was the only available merit to indicate the heat generation across the filament.

Glow was only observed in the intertwined filament design (Figure 3.2a), and not in the polished tip design (Figure 3.2b). Additionally, the polished tip was so fragile that it regularly fractured during handling. The consequence of fracture in this design was also greater than fracture in the intertwined filament design, as the intertwined filament design only required replacement of the fractured heating filament while fracture in the polihsed-tip design required polishing of a new filament. For these reasons, the polished tip design was quickly discarded in favour of the intertwined filament design.

The final version of the conductive and heating filaments consisted of two alumina tubes containing four $1\,\mathrm{mm}$ 8020NiCr filaments each for electrical conduction, with a single $0.4\,\mathrm{mm}$ Kanthal A filament tied between the ends for heating. Figure 3.4 shows the resulting glow when applying a voltage of $11\,\mathrm{V}$ across the filaments.

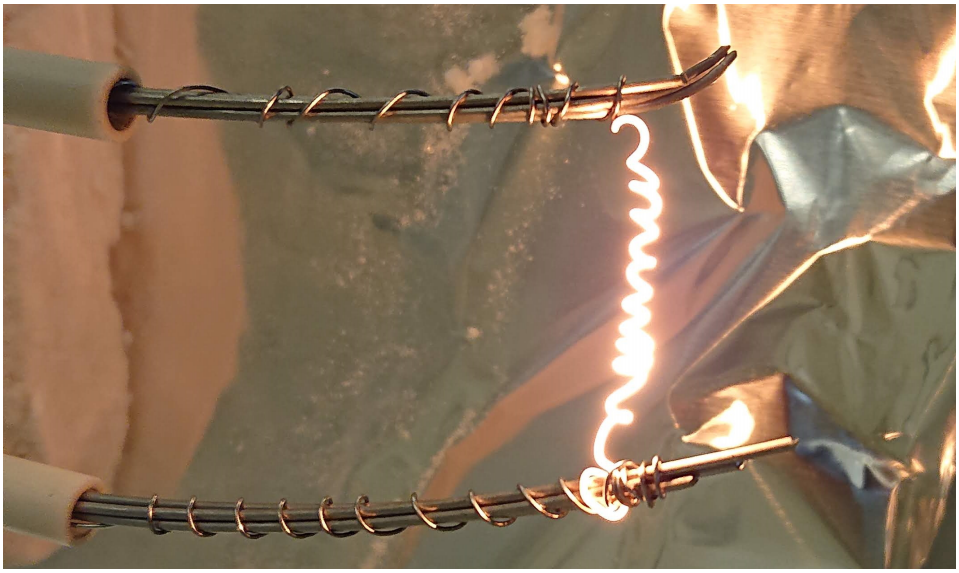

Figure 3.4: Glow in $0.4\,\mathrm{mm}$ Kanthal A filament connected to four $1\,\mathrm{mm}$ 8020 NiCr filaments on each end with an applied voltage of $11\,\mathrm{V}$

The IR-thermometer was used to measure the temperature of several samples of this design, and the maximum measured temperature was $482\,^{\circ}\mathrm{C}$. However, the fact that an almost white glow occured suggests that the temperature in the filament was higher than measured [84].

3.4.2 Chemical ignition

To achieve ignition in the Zr-Si pellet samples, a chemical igniter was needed to assist the heating filament. The igniter needed to fulfill the listed requirements:

- Stable during preparation for use in SHS
- Reaction independent of surroundings, *i.e.* mixture containing both oxidizer and reducer
- Ignition temperature lower than maximum achievable temperature in heating filament
- Burning temperature higher than ignition temperature of Zr-Si mixture

As shown in section 2.2.2, a powder mixture of Mg and BaO_2 is expected to fulfill these requirements, but the feasability was tested nontheless. Since Mg is readily oxidized and BaO_2 is unstable and may release oxygen gas (see section 2.2.2), the powders were characterized by XRD. The sealed magnesium-container was opened in an argon atmosphere glovebox where a glass vial was filled and taken out. It was exposed to ambient atmosphere at room temperature for approximately six hours before XRD, where it was characterized

over a 2θ-range of 30–130° using step size of 0.01° with 1.1 s per step. The resulting diffractogram is shown in Figure 3.5

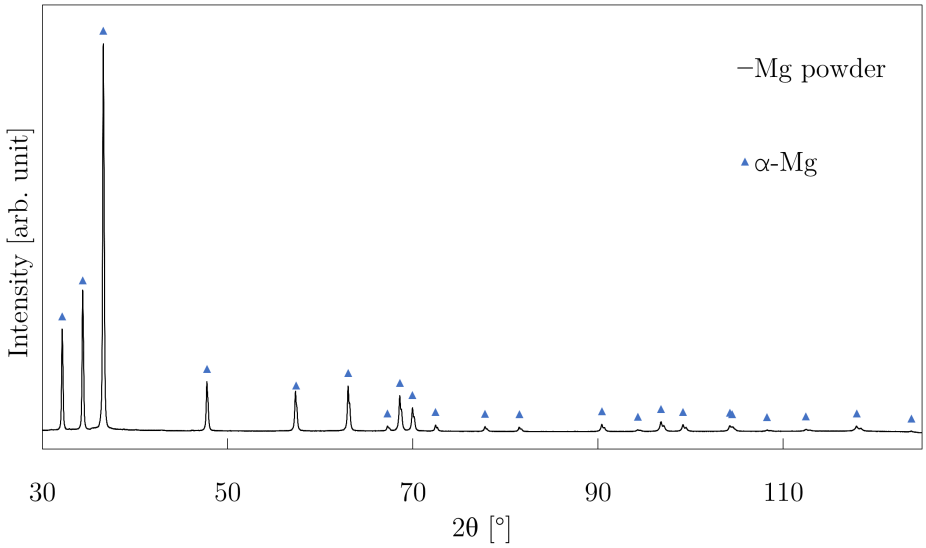

Figure 3.5: Diffractogram from XRD over a 2θ-range of 30–130° of magnesium powder using a step size of 0.01° with 1.1 s per step

The diffractogram indicates that potential impurities were below detectable amounts, and that the powder had not oxidized during exposure to ambient atmosphere at room temperature. The BaO_2-powder container had previously been opened and had been stored at ambient conditions. The powder was character over a 2θ-range of 20–145° with a step size of 0.01° and 0.9 s per step. The resulting diffractogram is shown in Figure 3.6

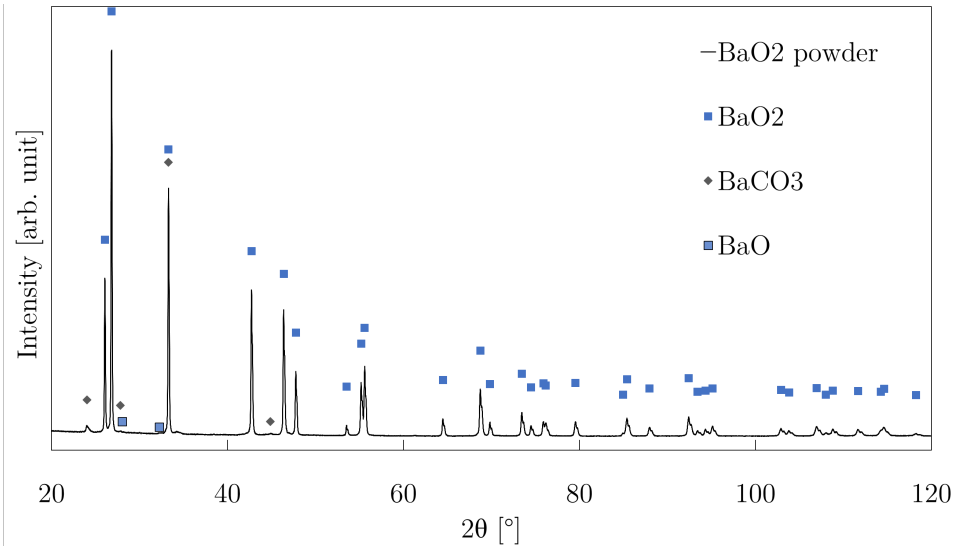

Figure 3.6: The resulting diffractogram from XRD of BaO_2-powder over a 2θ-range of 20–145° with a step size of 0.01° and 0.9 s per step. The indicators show which phases contribute to which peaks in the combined Pawley and Rietveld refinement in the 2θ-range 20–120°. It should be noted that the last peak indicated with BaO_2 was excluded in the final refinement, but previous refinements indicated that the peak was solely caused by BaO_2

Combined Pawley and Rietveld refinement was used to estimate the composition of the sample, but only in the 2θ-range 20–120°. The last part of the diffractogram was excluded due to difficulties with simulating the drop in background signal after the last peak. The results from the refinements are presented in Table 3.4.

Table 3.4: The resulting composition from combined Pawley and Rietveld refinement of the diffractogram in Figure 3.6. The Rwp and GOF were 13.6 and 4.7 respectively

Phase	Amount [at.%]
BaO_2	96
$BaCO_3$	3
BaO	1

The results of characterization of both magnesium and BaO_2 -powder indicates that they are stable at ambient conditions. For the most part, powdered magnesium was used in the igniter mixture, but chips from a magnesium ribbon was also utilized. Both were tested with DSC/TGA-analysis: For the igniter mix using magnesium chips, the magnesium chips and BaO_2-powder were mixed directly in the anlysis-crucible with a large molar

surplus of BaO_2 (Ba/Mg-ratio = 4.9/1) to ensure that all surfaces of the magnesium chips were able to react with adjacent BaO_2. As for the magnesium powder, the powders were mixed with an approximate molar ratio of 1/1, and pressed to a pellet. The pellet was then carefully split into pieces, where some pieces where chosen to be used as the DSC/TGA sample. Both samples were heated to 600 °C and subsequently cooled down to room temperature, with a heating- and cooling rate of 600 °C h^{-1}, and alumina powder was used as reference. The results are shown in Figure 3.7 and Figure 3.8.

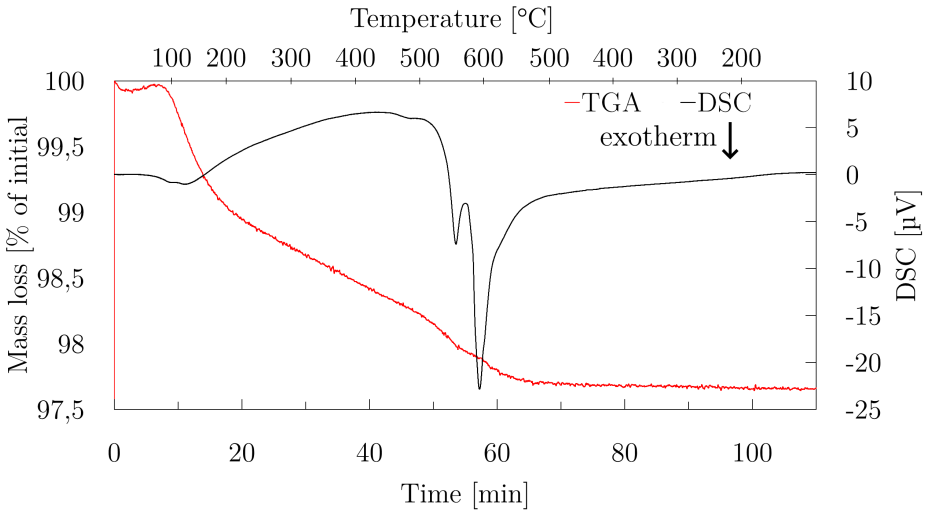

Figure 3.7: DSC and TGA data from heating a mixture of small Mg-chips and BaO_2-powder up to 600 °C and cooling down to room temperature, with a heating- and cooling rate of 600 °C h^{-1} and alumina powder as reference

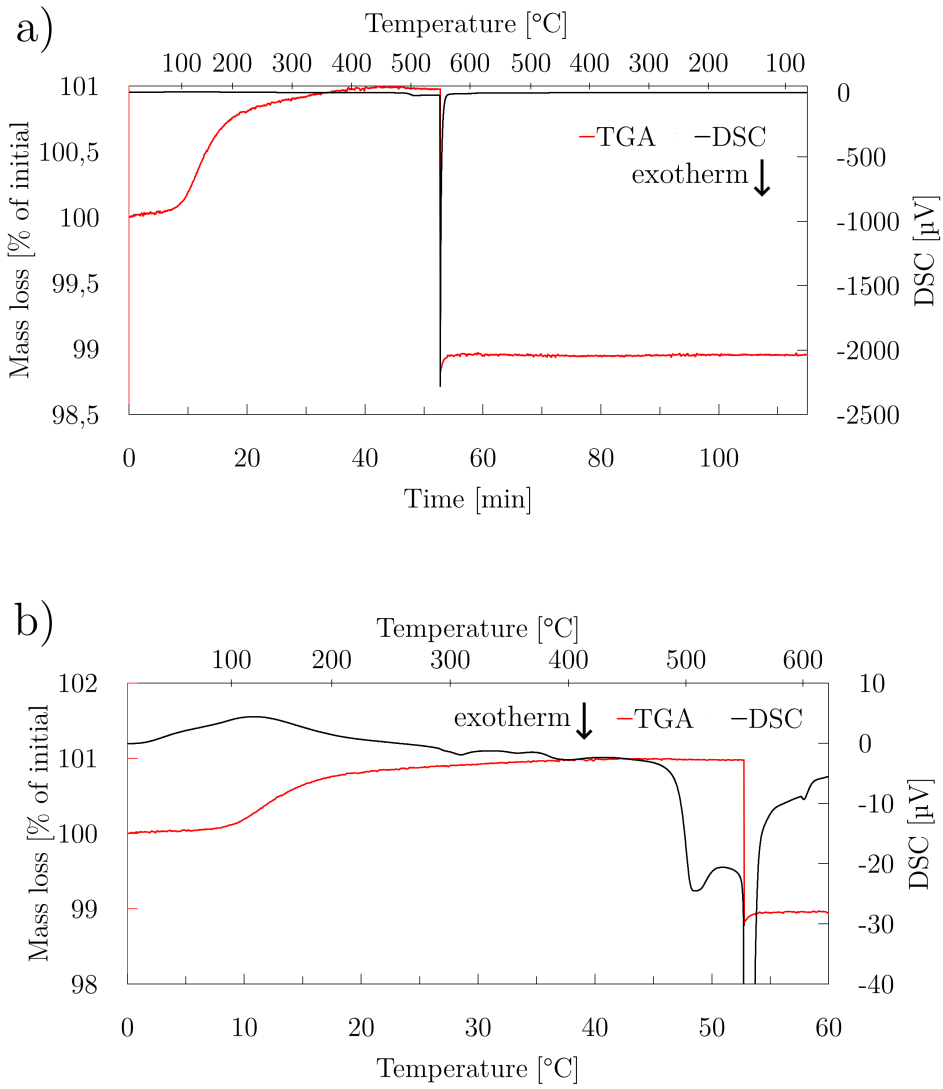

Figure 3.8: DSC and TGA data from heating a mixture of magnesium- and BaO_2-powder up to 600 °C and cooling down to room temperature, with a heating- and cooling rate of 600 °C h^{-1} and alumina powder as reference. a) shows the whole measurements, while b) highlights measurements before ignition.

Figure 3.7 shows an exothermic reaction in two stages being initiated around 550 °C, which agree well with previous literature (see section 2.2.2) The results also indicate a

continuous mass loss starting at around $100\,^{\circ}\mathrm{C}$ which could be due to release of oxygen gas from BaO_2, but may also be due to volatilization of impurities like moisture. Either one correlates well with the long endotherm curve. Figure 3.8a indicates that the reaction is substantially faster with magnesium powder compared to the magnesium chips. Simultaneously with the rapid exotherm reaction a rapid mass loss occurs. This can be attributed to an increase in oxygen release from BaO_2 with increasing temperature. Figure 3.8b shows a more detailed view of the measurement prior to ignition. The figure shows that the exotherm reaction is two-stepped, and is initiated at a lower temperature than the mixture containing magnesium chips. The figure also indicates an initial endotherm behaviour, and a mass increase when the endotherm behaviour stops. A possible explanation is that the mass increase is due to oxidation of the magnesium powder by the atmosphere, and the exotherm character of this oxidation counters the endotherm trend in the sample containing magnesium chips. The results of the DSC/TGA-measurements and the filament experiments indicated that the combination of filament and chemical igniter was a feasible way of reaching ignition temperature in a small volume of a Zr-Si sample.

3.5 SHS experiments

3.5.1 SHS-experiment configurations

SHS-experiments were done at room temperature, $600\,^{\circ}\mathrm{C}$, and one experiment utilized the temperature gradient in the furnace when set to $1400\,^{\circ}\mathrm{C}$. The general configuration was substantially different between these experiment-types. The configuration of the experiments at room temperature and at $600\,^{\circ}\mathrm{C}$ did in turn vary slightly, so in total a wide variety of configurations were used. The configurations were developed and improved through trial and error, so only a selection of the performed experiments will be presented. The experiments that will be presented are the ones were the igniter pellet was successfully ignited and characterization gave indicative results. Some of the mixtures used in the experiments were mixed by hand-mortaring while others were mixed by attritor-milling. However, no significant difference was observed during the experiments and characterization, so the milling technique used for the sample in each experiment will not be declared. In all the experiments, the Si(10-75) as this was expected to have the most similar particle size distribution as the zirconium powder.

XRD and SEM-imaging in BSE-mode, and EDS was used to characterize reacted samples. The XRD characterization was done over a 2θ-range of 10–90° with 0.9 per step.

Configurations at room temperature

The basis for the setup of the SHS-experiments at room temperature was shown in Figure 3.1. However, due to difficulty with arranging the sample, igniter, and filament, the conductive filament was shortened so the location of the filament was easier to control when the customized flange was attached to the tube furnace. Each experiment required a new sample, igniter pellet, and heating filament, and the performance of the set-up varied from experiment to experiment. So the actual configuration - in addition to what type of alumina container was used to contain the sample - varied from experiment to experi-

ment. The configurations that were used can be arranged into three general configurations, illustrated in Figure 3.9

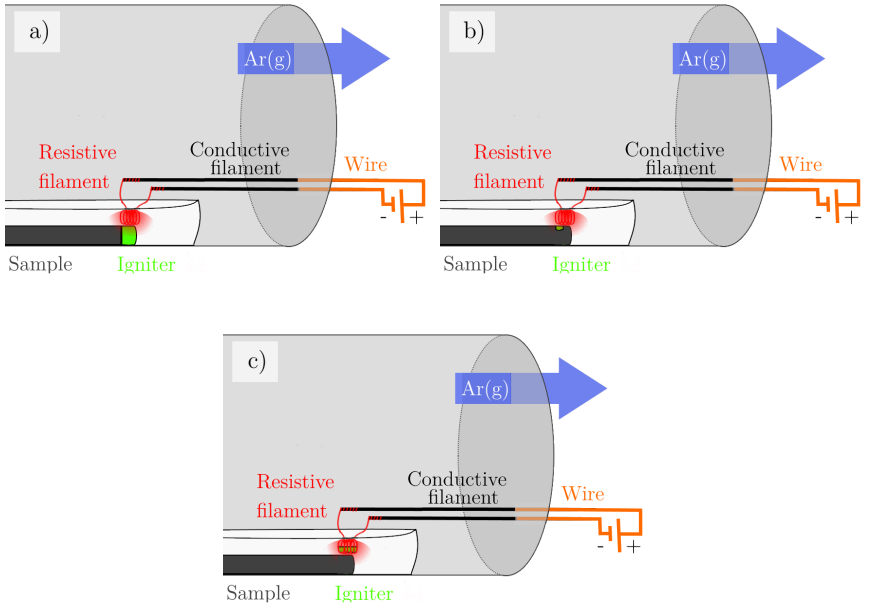

Figure 3.9: Illustrations of the three general configurations of sample, igniter, and filament in room temperature SHS experiments. a) illustrates a sample in contact with an igniter pellet which in turn is in (attempted) contact with the heating filament. This configuration is referred to as "Independent Igniter" in text, and "Indep. Ign.)" in sample names. b) illustrates an igniter pellet pressed within the sample, and the filament is in (attempted) contact with the igniter. This configuration is referred to as "Pressed in igniter" in text, and "Pressed in ign." in sample names. c) illustrates the igniter pellet being forced to be in contact with the filament, which is in (attempted) contact with the sample. This configuration is referred to as "Igniter in filament" in text, and "Ign. in fila." in sample names.

Figure 3.9a illustrates the initial configuration of sample, igniter, and filament in the room temperature SHS-experiments. Here, the goal was to have a beam Zr-Si sample in contact with an igniter pellet, which would be in contact with the filament. This configuration will be referred to as "Independent Igniter" in text, and "Indep. Ign.)" in sample names.

The configuration illustrated in Figure 3.9b was attempted to assure contact between the Zr-Si sample and the igniter and also to contain the heat generated in the igniter in the Zr-Si sample. In this configuration the goal was to have an igniter beam pressed into one end of Zr-Si beam which would be in contact with the filament. This configuration will be

referred to as “Pressed in igniter” in text, and “Pressed in ign.” in sample names.

The configuration illustrated in Figure 3.9c was attempted to better assure contact between igniter pellet and filament so that the igniter would consistently ignite quickly after application of voltage to the filament across experiments. The goal in this configuration was to ensure thermal contact between an igniter pellet and the heating filament, which would be in contact with the Zr-Si sample. This configuration will be referred to as “Igniter in filament” in text, and “Ign. in fila.” in sample names.

Configurations at $600\,^{\circ}\mathrm{C}$

Two experiments were done by using the tube furnace to heat an igniter-containing Zr-Si sample to $600\,^{\circ}\mathrm{C}$, which is slightly above the igniter's measured ignition temperature (see section 3.4.2. In both cases, the samples and the argon atmosphere in the furnace were heated to $600\,^{\circ}\mathrm{C}$ and subsequently cooled down to room temperature, with a heating an cooling rate of $200\,^{\circ}\mathrm{C}\,\mathrm{h}^{-1}$. The geometry of the sample and the placement of the igniter pellet varied between the experiments, and is illustrated in Figure 3.10.

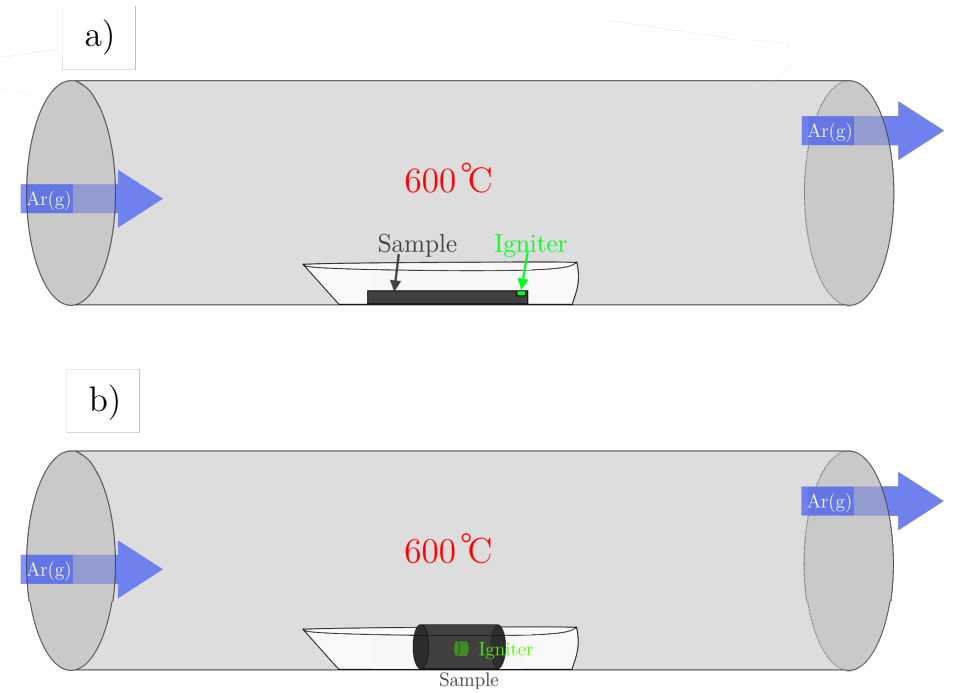

Figure 3.10: Illustration of configurations used in SHS-experiments were the sample and surroundings are heated to 600 °C. a) illustrates a beam-shaped sample with an igniter pressed in at one end. This configuration is referred to as “Igniter in beam end” in text and “Ign- in beam” in sample names. b) illustrates a cylindrical sample where the igniter is pressed in the center of the sample. This configuration is referred to as “Igniter in cylinder” in text and “Ign- in cylinder” in sample names.

Figure 3.10a illustrates the initial configuration, where an igniter pellet was pressed into a Zr-Si beam. This configuration will be referred to as “Igniter in beam end” in text and “Ign- in beam” in sample names. The configuration illustrated in Figure 3.10b was attempted to insure that the all the heat generated in the igniter would be transferred to the sample and not be dissipated into the furnace atmosphere. This configuration will be referred to as “Igniter in cylinder” in text and “Ign- in cylinder” in sample names

3.5.2 Configuration utilizing furnace temperature gradient

An experiment was done were the temperature gradient in the tube furnace was utilized by placing a “long” samples with one end in the center of the furnace. A previous measurement done by technical staff suggests that when setting the furnace to 1400 °C, the center of the furnace will reach approximately 1391 °C. By adding a 2nd degree polyno-

mial trend line in MS Excel, the temperature at the far end was estimated to be 1337 °C, which can be considered as T_0 at the far end, while T_0 increases towards the center of the furnace and the other end of the sample. The configuration is illustrated in Figure 3.11. This configuration is referred to as "Temperature gradient" in text and "Temp. grad." in

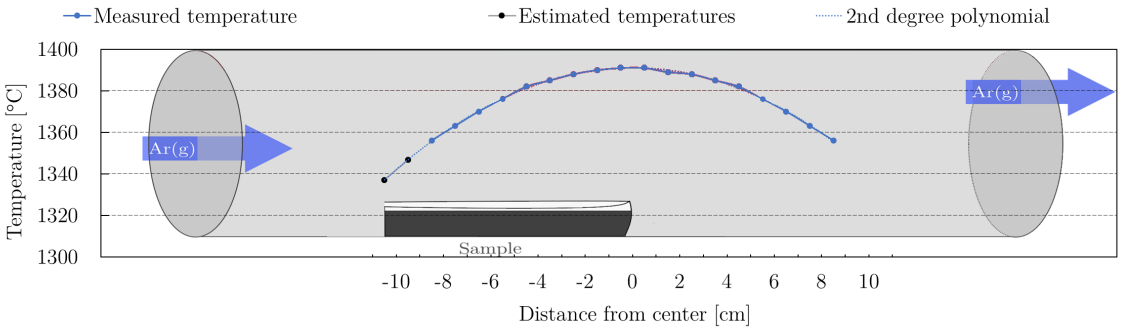

Figure 3.11: Illustration of the set-up used for an SHS experiment only utilizing the inherent temperature gradient in the tube furnace. This configuration is referred to as "Temperature gradient" in text and "Temp. grad." in samples

samples.

3.5.3 SHS at room temperature

In all these experiments, a current was passed through the filament with increasing voltage until ignition of the igniter pellet was observed. The heating duration was 1–2 min for all the samples, and the voltage across the filament was 8–12 V just before ignition.

Experiments with Zr+2Si samples

Four experiments done with Zr+2Si beams at room temperature were found to be of relevance. In the first SHS experiment, the igniter pellet was pressed from magnesium chips and BaO_2-powder. This was the only experiment where magnesium chips were used instead of magnesium powder. The experiment was set-up with the "Independent igniter"-configuration (see section 3.5.1 and Figure 3.9a) in an alumina ship. The mass of the igniter pellet was not documented. The sample will be referred to as "Zr+2Si(Room temp, Indep. Ign.)1". Two powder samples were made from the beam; one from the end of the beam which had been in contact with the igniter, and one a few millimeters from the same end. These powder samples were characterized by XRD and composition was estimated using combined Pawley and Rietveld refinement.

The second experiment was done with the same configuration. The differences were that the igniter pellet was made from magnesium powder instead of chips, and that sample, igniter, and filament was placed in a closed-end alumina tube. The mass of the igniter pellet was 0.220 g. The sample will be referred to as "Zr+2Si(Room temp, Indep. Ign.)2".

Two powder samples were made from this sample, one from the contact point with the igniter, and one some millimeters away from the contact point.

The third experiment at room temperature was done with the configuration illustrated in Figure 3.9b. This experiment was done in the same alumina tube that was used in the experiment presented in the previous paragraph. The mass of the igniter pellet was $0.110\,\mathrm{g}$. The samples will be referred to as "Zr+2Si(Room temp, Pressed in ign.)". Three powder samples were made from the sample; one from the end of the sample which had been in contact with the igniter, one a few millimeters from the same end, and one from the middle of the sample. These powder samples were characterized qualitatively by XRD.

The final Zr+2Si beam experiment was set-up according to the configuration "Igniter in filament" (see section 3.5.1 and Figure 3.9c) in an alumina tube. The mass of the igniter pellet was $0.254\,\mathrm{g}$. A current was passed through the filament with increasing voltage until ignition of the igniter pellet was observed. This sample will be referred to as "Zr+2Si(Room temp, Ign. in fila.)" Three powder samples were made from the beam; one from the end of the beam which had been in contact with the igniter, one a few millimeters from the same end, and one from approximately one centimeter of one of the long side of the beam, taken a few millimeters from the igniter side. These powder samples were characterized qualitatively by XRD.

Experiment done with Zr+Si sample

One experiment was done with a Zr+Si beam in the "Igniter in filament"-configuration in an alumina ship. The mass of the igniter pellet was $0.126\,\mathrm{g}$. The sample will be referred to as "Zr+Si(Room temp, Ign. in fila.)". Two pieces of the beam that had been struck by exploding igniter were taken, where one were milled down and characterized by XRD. The other was used to prepare a sample for SEM-imaging in BSE mode. The sample was polished for $4\,\mathrm{min}$ with Struers $30\,\mu\mathrm{m}$ SiC-paper, and for $30\,\mathrm{min}$ with Struers MD-Dur polishing cloth. The sample was then imaged with SEM in BSE-mode, and characterized by EDS.

3.5.4 SHS at 600 °C

Experiments done with Zr+2Si samples

Two experiments done with Zr+2Si samples at $600\,^{\circ}\mathrm{C}$ were found to be of relevance. The first was done with the "Igniter in beam end"-configuration (see section 3.5.1 and Figure 3.10a). The igniter mass was $0.327\,\mathrm{g}$. The sample will be referred to as "Zr+2Si($600\,^{\circ}\mathrm{C}$, Ign. in beam)". Two powder samples were taken for XRD, and the composition of these samples were estimated with combined Pawley and Rietveld refinement.

The second was done with the "Igniter in cylinder center"-configuration (see section 3.5.1 and Figure 3.10b). The igniter mass was $0.104\,\mathrm{g}$ and the pellet mass Zr+2Si cylinder mass was $3.437\,\mathrm{g}$. The sample will be referred to as "Zr+2Si($600\,^{\circ}\mathrm{C}$, Ign. in cylinder)". After the experiment a powder sample was characterized by XRD, and the composition of each piece was estimated with combined Pawley and Rietveld refinement. A sample for

SEMimaging in BSE-mode was prepared and polished for$4\,\mathrm{min}$ with Struers $30\,\mu\mathrm{m}$ SiC-paper, and for $30\,\mathrm{min}$ with Struers MD-Dur polishing cloth. The sample was then imaged with SEM in BSE-mode, and characterized by EDS.

Experiment done with Zr+Si sample

One experiment done with Zr+Si samples at $600\,^{\circ}\mathrm{C}$ was found to be of relevance. This sample was done in the same experiment as the sample Zr+2Si($600\,^{\circ}\mathrm{C}$, Ign. in cylinder) which was presented in the previous section, *i.e.* with the "Igniter in cylinder center"-configuration. The igniter mass was $0.104\,\mathrm{g}$ and the Zr+Si cylinder mass was $3.511\,\mathrm{g}$. This sample will be referred to as "Zr+Si($600\,^{\circ}\mathrm{C}$, Ign. in cylinder)". The sample was also characterized in the same manner as Zr+2Si($600\,^{\circ}\mathrm{C}$, Ign. in cylinder).

3.5.5 Experiment using furnace temperature gradient

An Zr+2Si mixture was used in an experiment with the "Temperature gradient"-configuration (see section 3.5.1 and Figure 3.11). The sample was made by filling an alumina ship and lightly compacting the powder while it was slightly moist with isopropanol. There was no dwell after the heating, and the heating and cooling rate was $200\,^{\circ}\mathrm{C}\,\mathrm{h}^{-1}$. The sample will be referred to as "Zr+2Si($1400\,^{\circ}\mathrm{C}$, Temp. grad.)". After synthesis, three powder samples were characterized by XRD and the composition of each sample was estimated with combined Pawley and Rietveld refinement. Two SEM samples were prepared from where it seemed to be a reaction front, one where the top of the sample (*i.e.* side exposed to the furnace atmosphere) was to be imaged in BSE-mode and characterized with EDS, and the other of one of the horizontal sides of the sample.

3.5.6 Sample table

All the samples that were presented in the previous sections are gathered in Table 3.5.

Table 3.5: Samples from SHS-experiments, with the Zr-Si mixture used to make the sample, and the configuration and temperature of the experiment

Sample name	Zr-Si mixture	Configuration
Experiments at room temperature		
Zr+2Si(Room temp, Indep. Ign.)1	Zr+2Si	Independent (magnesium chips) igniter (Figure 3.9a) (In alumina ship)
Zr+2Si(Room temp, Indep. Ign.)2	Zr+2Si	Independent igniter (Figure 3.9a) (in closed-end alumina tube)
Zr+2Si(Room temp, Pressed in ign.)	Zr+2Si	Pressed in igniter (Figure 3.9b)
Zr+2Si(Room temp, Ign. in fila.)	Zr+2Si	Igniter in filament (Figure 3.9c)
Zr+Si(Room temp, Ign. in fila.)	Zr+Si	Igniter in filament (Figure 3.9c)
Experiments at 600 °C		
Zr+2Si(600 °C, Ign. in beam)	Zr+2Si	Igniter in beam end (Figure 3.10a)
Zr+2Si(600 °C, Ign. in cylinder)	Zr+2Si	Igniter in cylinder center (Figure 3.10b)
Zr+Si(600 °C, Ign. in cylinder)	Zr+Si	Igniter in cylinder center (Figure 3.10b)
Experiment with furnace temperature gradient at 1400 °C		
Zr+2Si(1400 °C, Temp. grad.)	Zr+2Si	Temperature gradient

3.6 Other experiments

3.6.1 Silicothermic reduction of ZrO_2

Silicothermic reduction of ZrO_2 by Si is a possible reason for asymmetric oxidation of zirconium and silicon. In order to study the effect of this reaction, zirconium powder was oxidized in synthetic air, mixed with silicon powder, and studied with TGA/DSC -analysis.

A sample of zirconium powder was weighed out and poured into an alumina ship. The ship was then placed in a tube furnace, where it was heated with a gas flow of synthetic air (80 % N_2 20 % O_2 to 1500 °C) where it was held for one hour before cooling to room

temperature. The sample was then characterized by XRD over a 2θ-range of 20–80° with 1.2 per step.

A part of the obtained powder was then mixed with the *Si(40-100)* powder with a Si/Zr-ratio of 3. This silicon powder was chosen since the SiO_2-fraction is expected to decrease with increasing powder size. A sample of this powder was characterized by DSC/TGA while heating up to 1550 °C in argon atmosphere.

3.6.2 Reactivity between zirconium silicides and precursors

To study the formation of high-zirconium zirconium silicides, a powder mixture of the Zr-powder and the Si(<75)-powder was used to make a 3Zr+Si mixture. This mixture was pressed to a pellet by combined uniaxial pressing followed by CIP, and heated to 1500 °C in argon atmosphere where it was held for 1 h and then cooled down to room temperature. The heating and cooling rate was 200 °C h^{-1} The sample was then characterized by XRD, and the composition was estimated by combined Pawley and Rietveld refinement. Then the sample - hereby referred to as "$Zr_{(3)}Si$" - was mixed with Si(<75)-powder to study the reactivity with silicon. Si(<75)-powder was added to a total Si/Zr-ratio of 2, *i.e.* the resulting mixture can be described as "$Zr_{(3)}Si$+5Si". Two pellets were made from this mixture first pressing uniaxially and then by CIP. One was heated to 1500 °C in argon atmosphere and held for 1 h before cooling to room temperature. The other was heated to 1400 °C in argon atmosphere and cooled to room temperature with no dwelling. The heating and cooling rate in both experiments was 200 °C h^{-1}. Both samples were characterized by XRD, and the compositions were estimated by combined Pawley and Rietveld refinement. The $Zr_{(3)}Si$+5Si sample that had been heated to and held at 1500 °C was mixed with Zr-powder to a desired Si/Zr-ratio of 1/3. Thus this sample can be described as $ZrSi_2$+Zr, and it was aimed to have the same Si/Zr-ratio as the initial mixture of zirconium and silicon -powders. This mixture was treated in the same manner as the $Zr_{(3)}Si$+5Si -mixture, *i.e.* one pellet heated to 1500 °C and held for 1 h, and the other to 1400 °C and instantaneously cooled down again. The samples were characterized by XRD over a 2θ-range of 10–90° with 0.9 per step and the composition was estimated by combined Pawley and Rietveld refinement. The experimental route is illustrated as a flow scheme in Figure 3.12

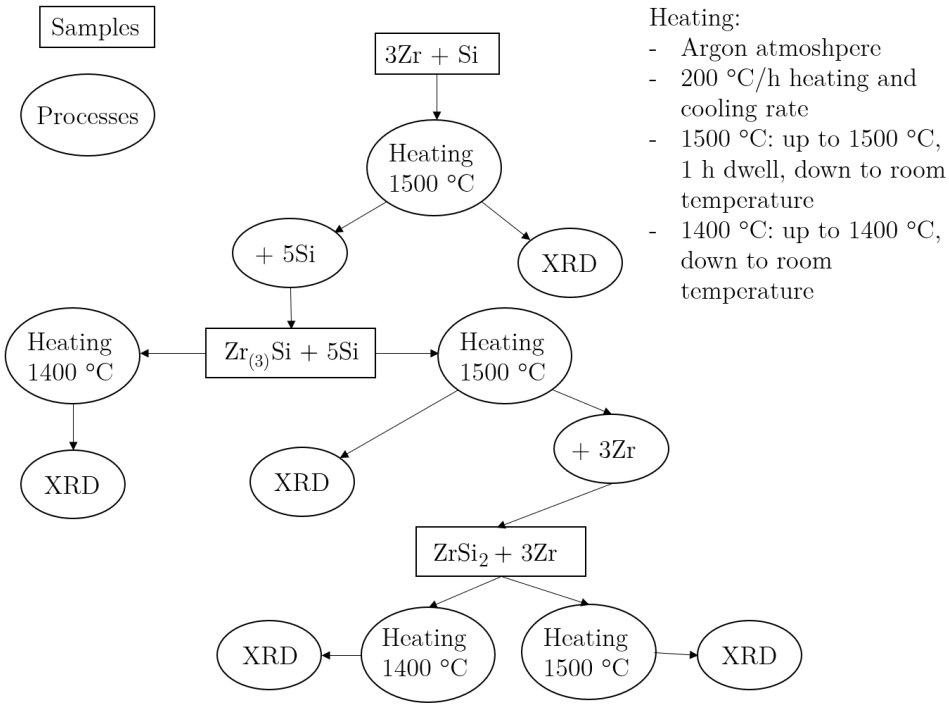

Figure 3.12: Flow scheme illustrating the preparation of an treatment samples for studying reactivity between zirconium silicides and zirconium and silicon powders

4 Results

4.1 Characterization of precursor powders

4.1.1 SEM images

Figure 4.1 shows SEM-images of the precursor powders taken in SE-mode at 100 X magnification at a working distance of 10 mm with 10.0 kV accelerating voltage.

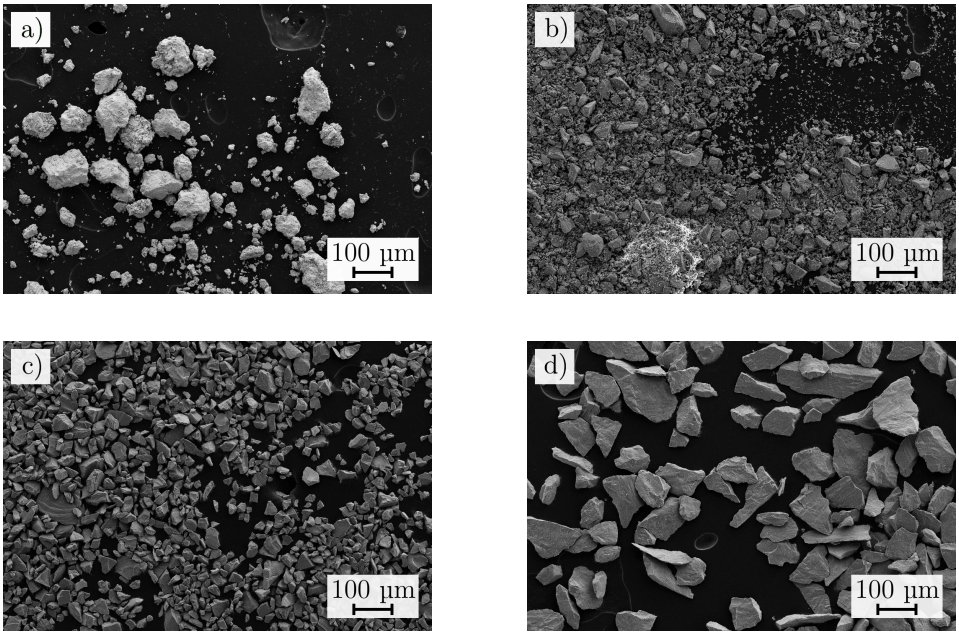

Figure 4.1: SEM-images in SE-mode, with 100 X magnification of the zirconium and silicon powders, where a) shows the zirconium powder, b) the Si(<75)-powder, c) the Si(10-75)-powder, and d) the Si(40-100)-powder.

The zirconium powder appears “fuzzy” and with a broad particle size distribution. The Si(<75) and Si(10-75) -powder resemble each other apart from the large amount of small particles in the Si(<75)-powder. The Si(40-100)-powder particles appears to be less symmetric than the particles of the other powders, and it has a large variation of morphology. Figure 4.2 shows the smallest observed particles in the zirconium and Si(<75) powders. Both images are taken in SE-mode with a working distance of 10 mm and an accelerating voltage of 10 kV. Figure 4.2a is taken at 16 kX magnification, and Figure 4.2b is taken at 40 kX magnification.

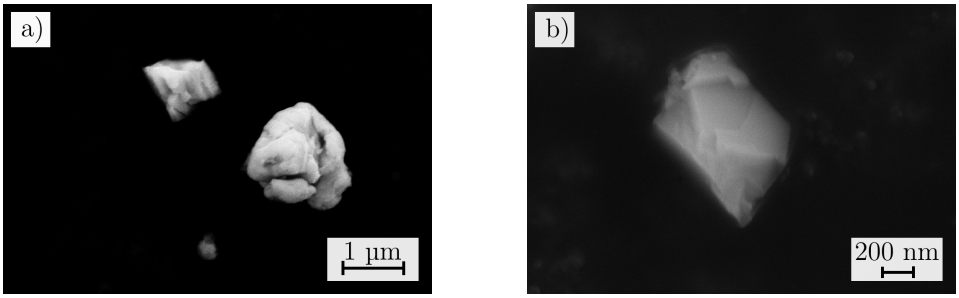

Figure 4.2: SEM-images in SE-mode of the smallest particles observed in the a) zirconium powder at 16 kX magnification and b) Si(<75) powder at 40 kX magnification

Based on these images, the zirconium powder appears to contain the smallest particles of all the powders.

4.1.2 Powder XRD

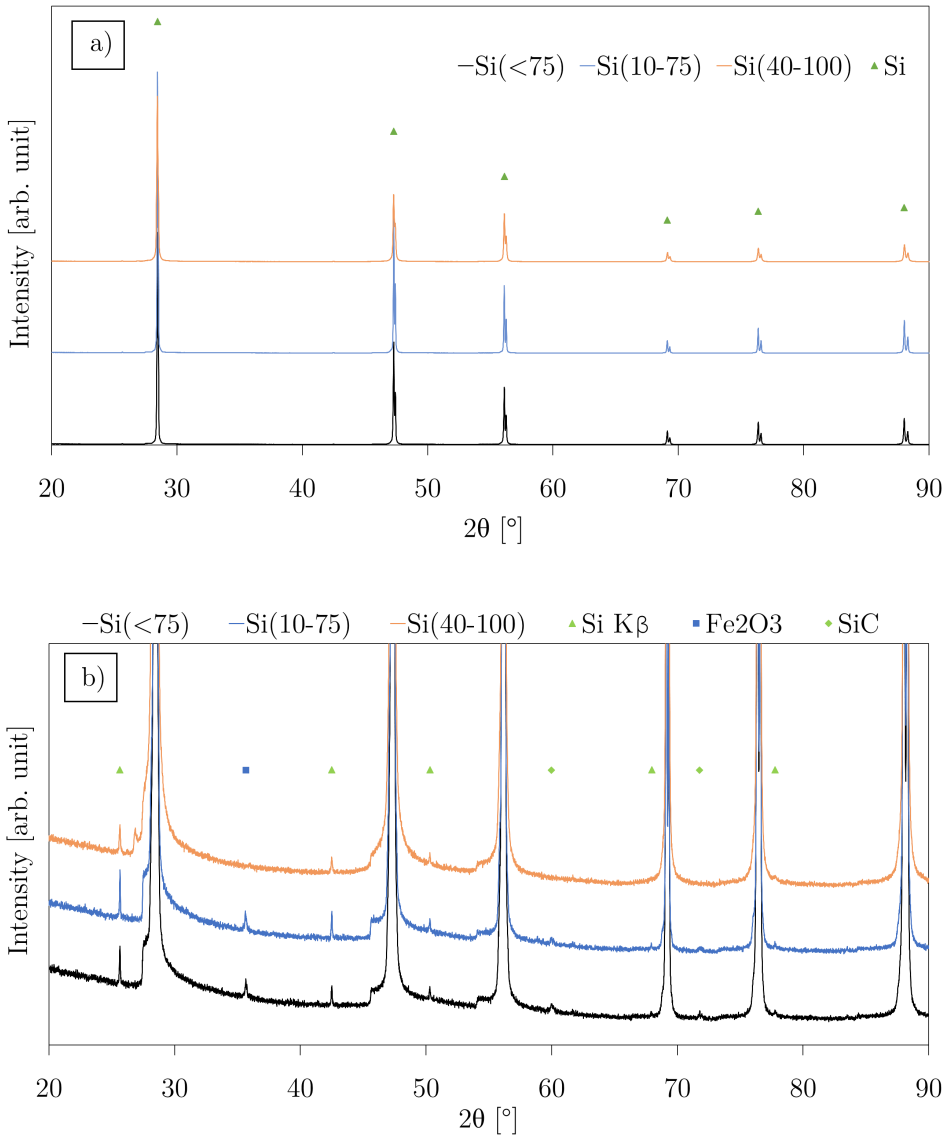

Figure 4.3: XRD diffractograms of the received silicon powders, where a) shows the full diffractograms and b) shows a low intensity range that reveals the smaller peaks

Figure 4.3 shows the resulting diffractograms of XRD of the silicon powders. The concentration of Fe_2O_3 and SiC appeared to be too low for combined Pawley and Rietveld refinement to produce consistent and sensible concentrations. Thus, the concentration of these impurities is considered to be negligible in further application of the powders.

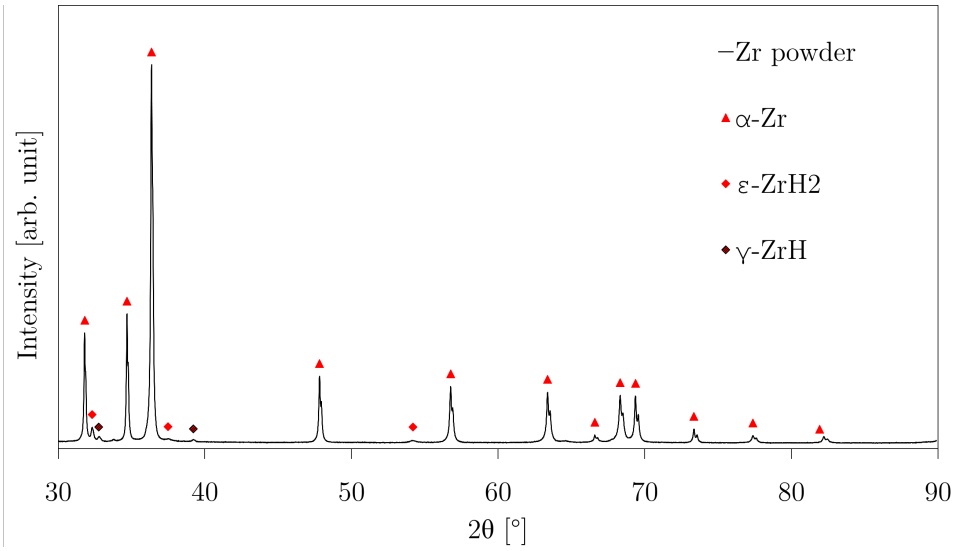

Figure 4.4: XRD diffractogram of the received Zr powder

Figure 4.4 shows the resulting diffractogram og XRD of the zirconium powder, and which phases that make a major contribution to each peak during combined Pawley and Rietveld refinement. The resulting composition is shown in Table 4.1

Table 4.1: Resulting composition from combined Pawley and Rietveld refinement of the diffractogram shown in Figure 4.4. Rwp and GOF were 4.39 and 3.23 respectively

Phase	Amount [at.%]
Zr	94
ϵ-ZrH_2	4
γ-ZrH	1
By element	
Zr	96
H	4

4.2 Co-milling of zirconium and silicon

The Zr+2Si mixtures milled in an attritor mill with different parameters (see section 3.3) were characterized by XRD and SEM in SE-mode. The diffractograms of the samples are shown in Figure 4.5

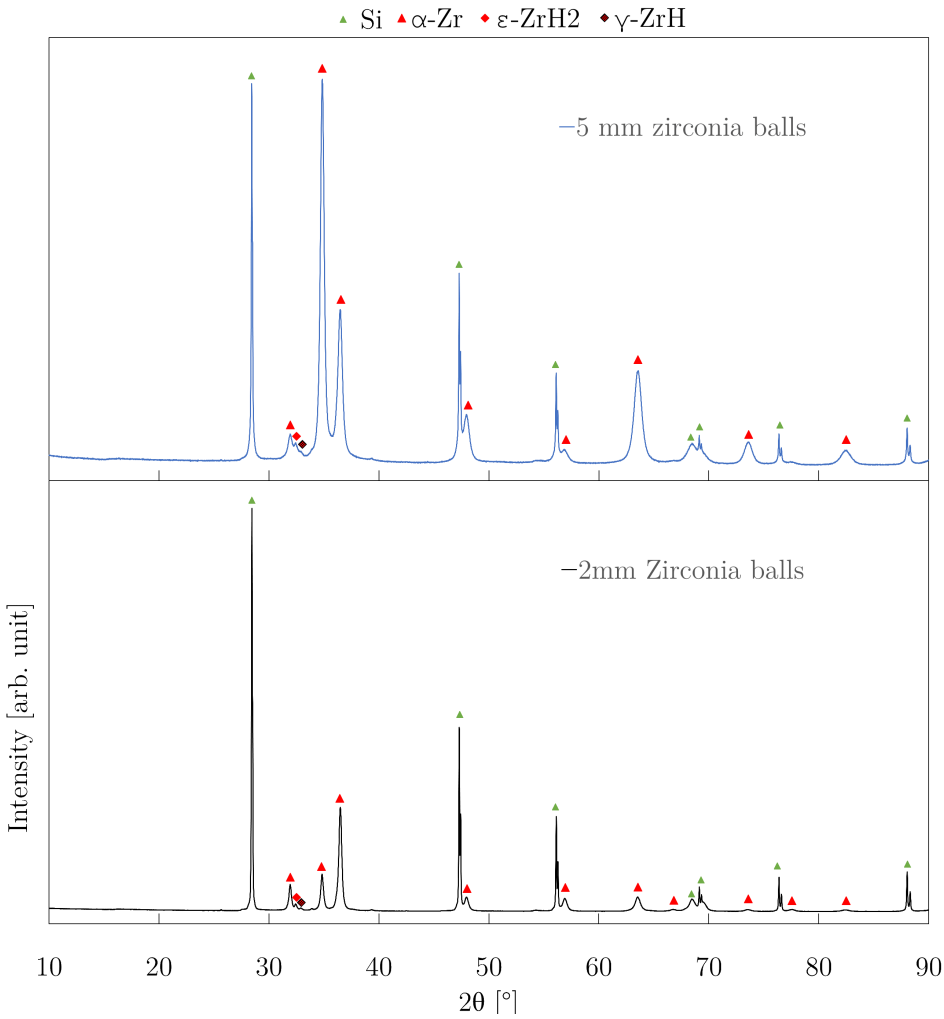

Figure 4.5: Diffractograms of attritor-milled Zr+2Si mixtures where one was milled with 5 mm zirconia balls, and the other was milled with 2 mm zirconia balls.

From the two diffractograms, it is evident that neither the zirconium or the silicon powder reacted during milling. Comparing with the diffractogram of the received silicon powder (see Figure 4.3), the only observable change is broadening of the peak at around 69°,

which is caused by diffraction in the $[4\,0\,0]$ plane, in both the milling experiments. As for zirconium there is are some significant differences between the two diffractograms. The peak intensities are closer to the peak intensities of silicon in diffractogram from the experiment with the large balls. Also, the peak intensity of the peak at around $35°$ relative to the other zirconium peaks is much higher in the experiment with the large balls. This peak is caused by diffraction in the $[0\,0\,0\,2]$ plane. Comparing the two diffractograms with the diffractogram of the received zirconium powder (see Figure 4.4) a substantial peak broadening in almost all the zirconium peaks is evident. SEM-images in SE-mode of the mixture milled with $5\,\mathrm{mm}$ zirconia balls is shown in Figure 4.6.

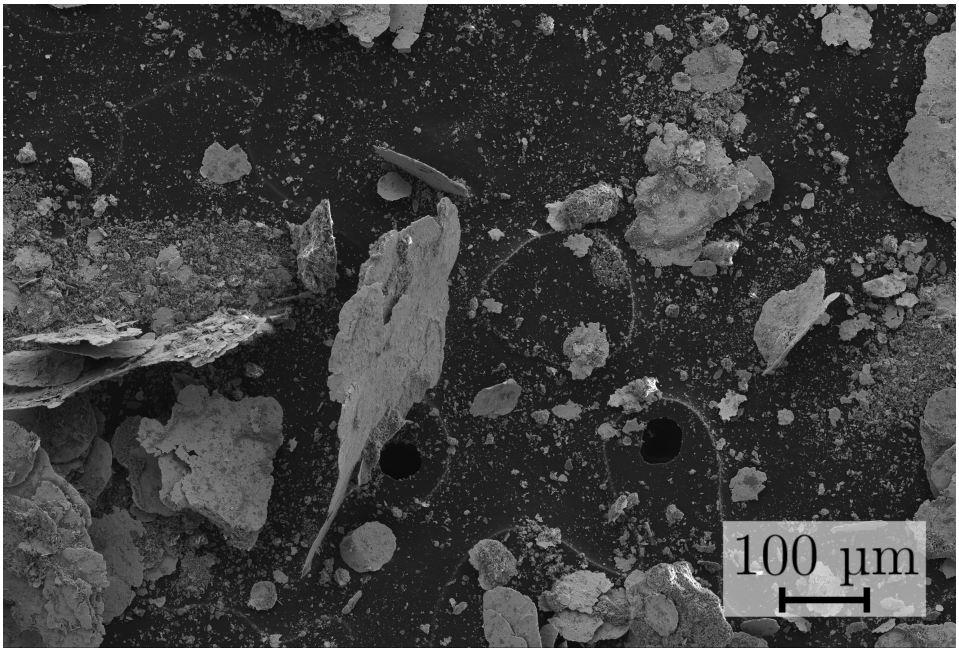

Figure 4.6: SEM-image taken in SE-mode of a Zr+2Si powder mixture attritor-milled with $5\,\mathrm{mm}$ zirconia balls in isopropanol

Figure 4.6 indicates that the zirconium particles have been smudged into large, flat flakes, instead of being crushed. The mixture milled with $2\,\mathrm{mm}$ zirconia balls is shown in Figure 4.7

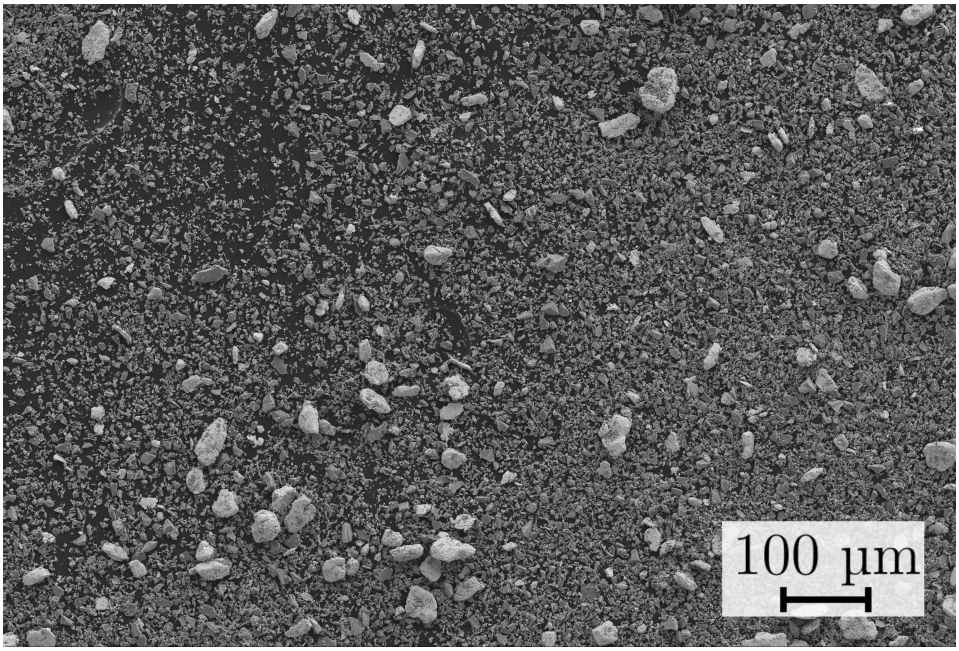

Figure 4.7: SEM-image taken in SE-mode of a Zr+2Si powder mixture attritor-milled with 2 mm zirconia balls in isopropanol

Figure 4.7 indicates that both the zirconium and silicon particles have been crushed, but that the silicon particles have been crushed to smaller particles than the zirconium particles.

4.3 SHS experiments

In this section, mainly results from characterization of the SHS-samples (see Table 3.5) will be presented. Some important observations done during the experiments will also be presented, and photographs of these observations are gathered in section D.

4.3.1 SHS at room temperature

In all the SHS-experiments at room temperature, it was obvious whether the filament was able to ignite the chemical igniter, as it was observable when the filament started glowing from the filament, when the igniter exploded and eventually stopped glowing along with the broken filament (see section D.1 for stills of a video). There were several attempts where the filament broke or the voltage was turned off (it was assumed that heating over long periods of time would weaken the assumption of the synthesis occurring at room temperature) without ignition of the igniter. However, in all the experiments presented in section 3.5.3 the igniter exploded as imaged in Figure D2b.

Experiments with Zr+2Si mixtures

After the experiment with sample Zr+2Si(Room temp, Indep. Ign.)1 (see Table 3.5), it was evident that the igniter had exploded, and that on the side that was in contact with the igniter, a melt from generated form the igniter had been stuck to the side (see section D.2). The origins of the XRD-samples taken from the sample are illustrated in Figure 4.8.

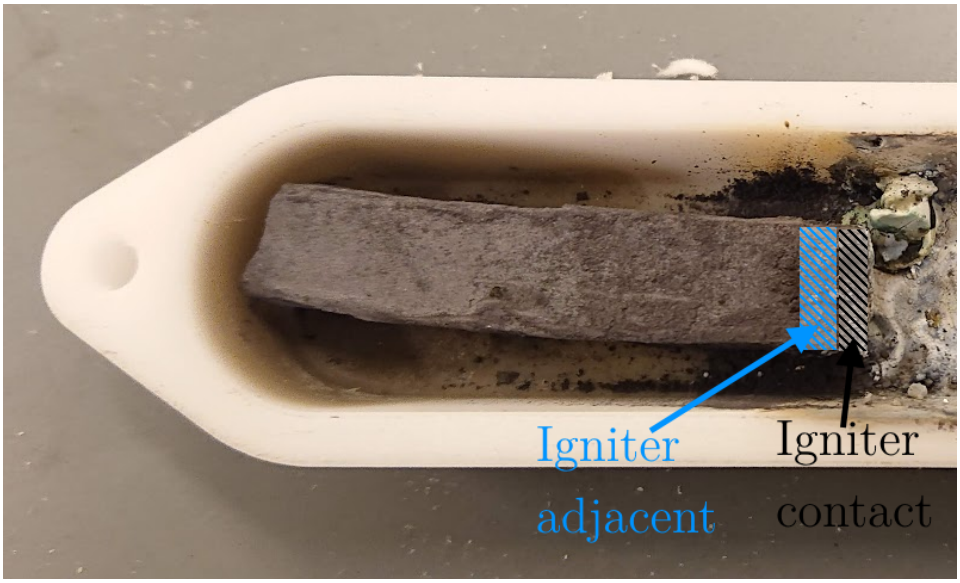

Figure 4.8: Illustration of where the powder samples for XRD were taken from the sample Zr+2Si(Room temp, Indep. Ign.)

Figure 4.9 shows the resulting diffractograms from XRD of the gathered powder samples.

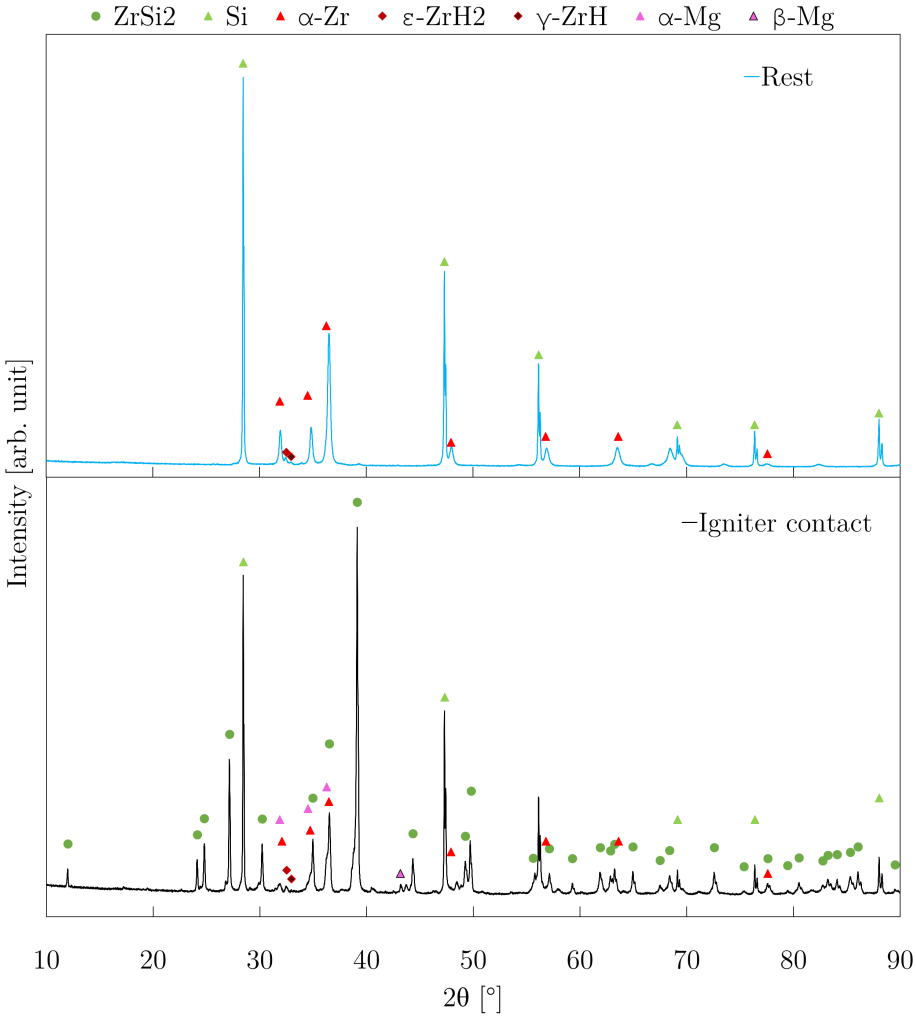

Figure 4.9: Resulting diffractograms from XRD of the Zr+2Si(Room temp, Indep. Ign.)1- The indicators indicate which phases contributed to which peaks in the combined Pawley and Rietveld refinement

Combined Pawley and Rietveld refinement was done to estimate the compositions of the samples, and the indicators show which phases contributed to which peaks during the refinement. It should be noted that β-Mg was not included during the initial qualitative analysis in Bruker Eva - which is why it is not included in Table 3.3 - but was added during the refinement. The resulting composition is shown in Table 4.2.

Table 4.2: Composition estimated by combined Pawley and Rietveld refinement of the diffractograms shown in Figure 4.9. Rwp and GOF were 9.36 and 4.0 for the "Igniter contact"-diffractogram and 7.40 and 3.0 for the "Igniter adjacent"-diffractogram

	Amount [$\mathrm{mol}\%$] in	
Compound	Igniter contact	Igniter adjacent
$ZrSi_2$	16	-
α-Zr	4	11
Si	69	89
ϵ-ZrH_2	<1	<1
γ-ZrH	<1	<1
α-Mg	7	-
β-Mg	3	-

The results indicate that $ZrSi_2$ was formed at the side in contact in the igniter, but not elsewhere in the sample. In the similar experiment with the sample Zr+2Si(Room temp, Indep. Ign.)2 (see Table 3.5), ignition of the igniter pellet was observed to split the alumina tube containing the sample in two (see section D.3). The resulting diffractograms of the powder samples taken for XRD is shown in Figure 4.10.

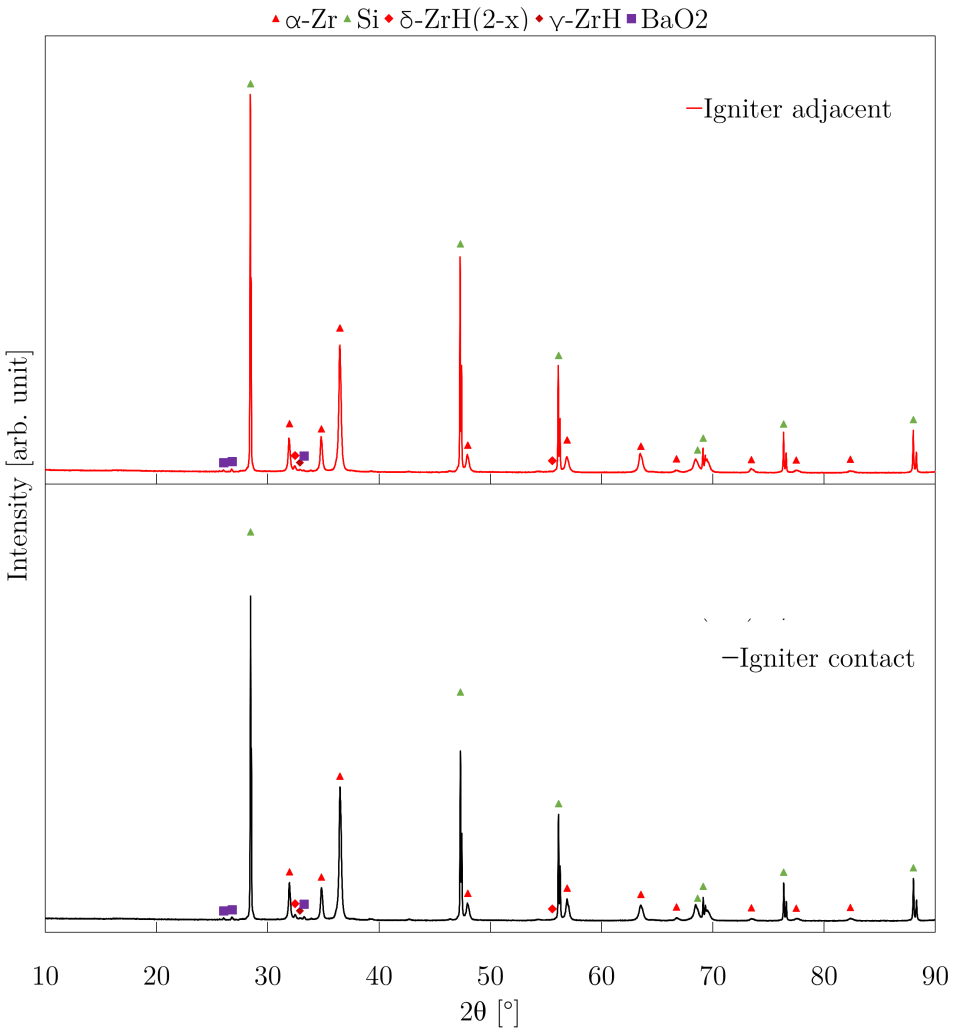

Figure 4.10: Diffractograms of samples taken from Zr+2Si(Room temp, Indep. Ign.)2 (see Table 3.5). The indicators illustrate which phases were attributed to which peaks during a qualitative assessment in Bruker Eva

A qualitative assessment of present phases indicate that no reaction has occured, as no zirconium silicicdes are present. Ignition of the igniter was observed in the experiment using the sample Zr+2Si(Room temp, Pressed in ign.) (see Table 3.5). The origins of the XRD-samples are illustrated in Figure 4.11

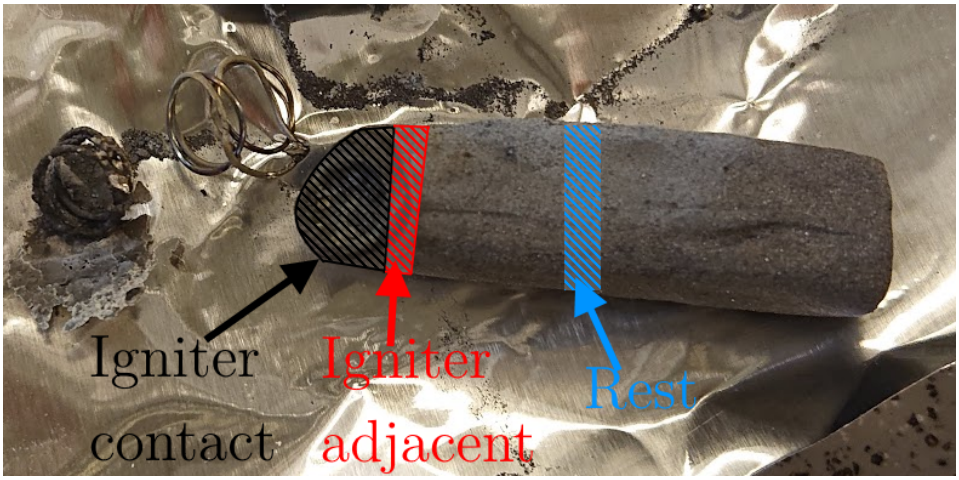

Figure 4.11: Illustration of the powder samples taken from Zr+2Si(Room temp, Pressed in ign.) (see Table 3.5)

The diffractograms from XRD of the powder samples taken from this is shown in Figure 4.12.

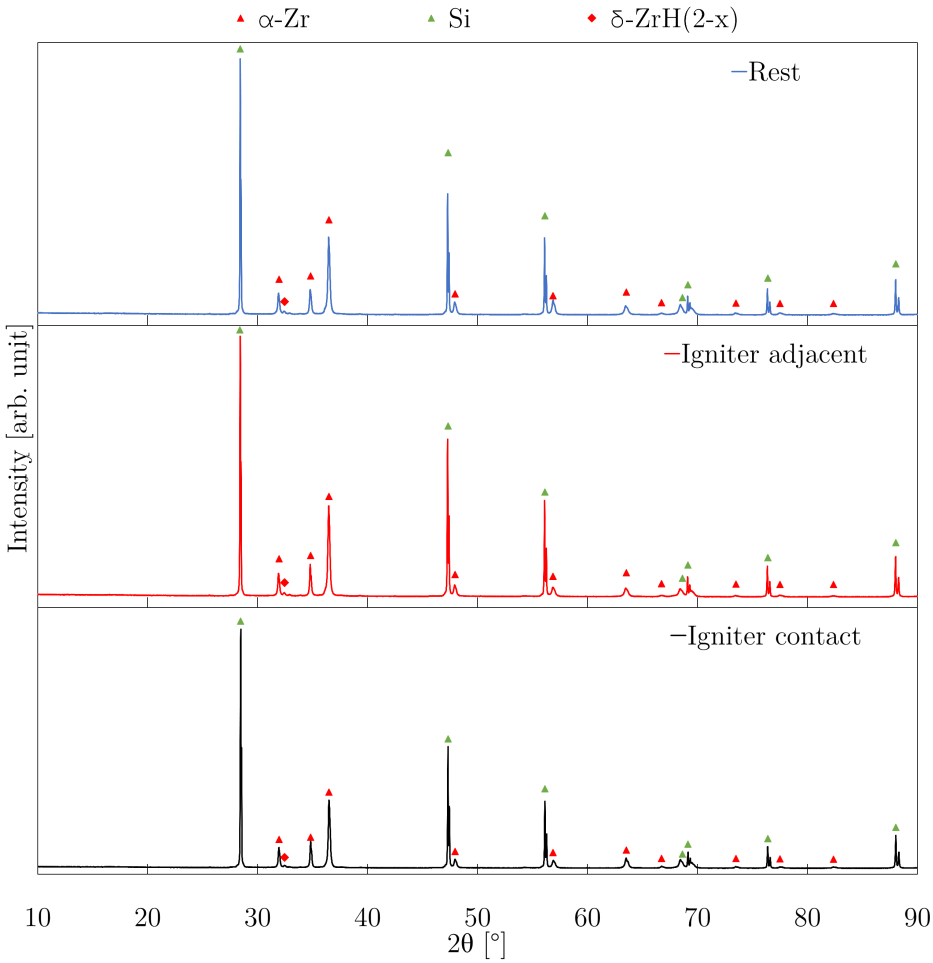

Figure 4.12: Resulting diffractograms from XRD of the samples from the room temperature SHS experiment where the heating filament was adjacent to the end of the Zr+2Si beam which had an igniter pellet pressed into it. The indicators indicate which phases are attributed to which peaks based on qualitative assessment in Bruker Eva.

The qualitative assessment in Eva showed that no zirconium silicides were formed in any part of the beam during the experiments.

Practically the same results were obtained from the sample Zr+2Si(Room temp, Ign. in fila.) (see Table 3.5). The origins of the XRD-samples are illustrated in Figure 4.13

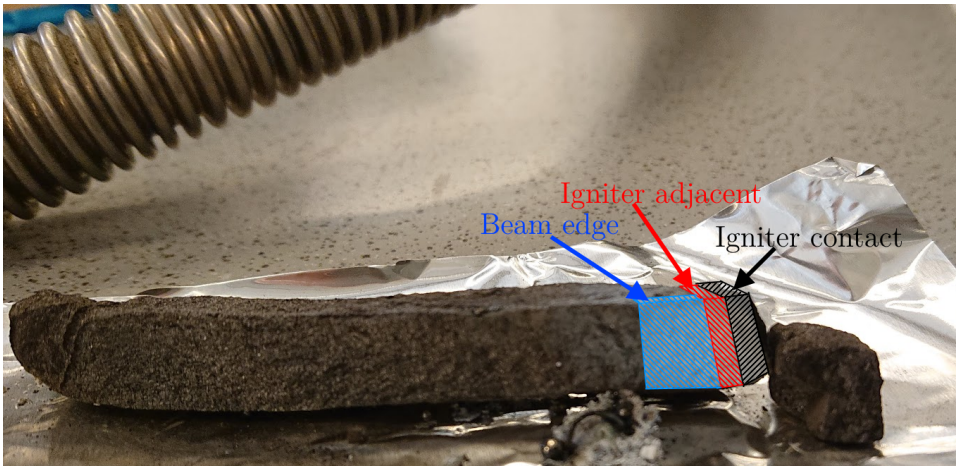

Figure 4.13: Illustration of the powder samples taken of the Zr+2Si samples from the SHS experiment with the configuration illustrated in Figure 3.9c

The resulting diffractograms are shown in Figure 4.14.

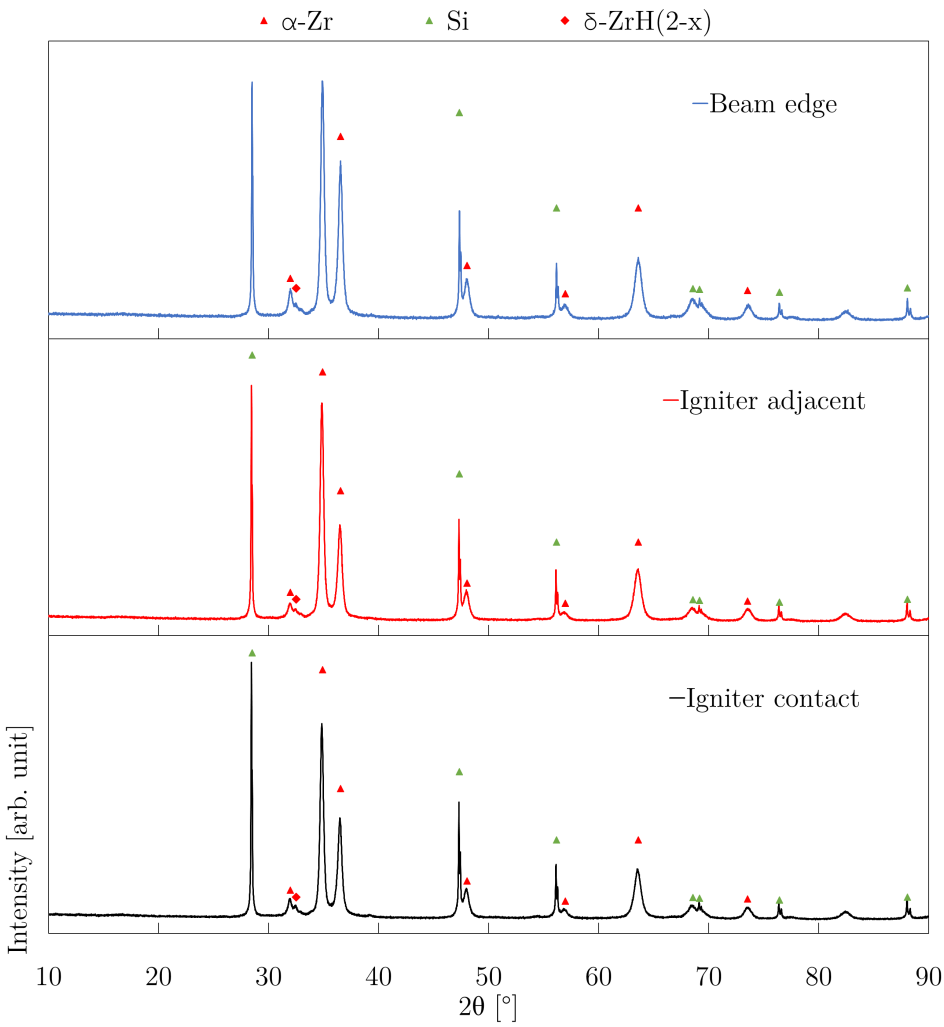

Figure 4.14: Resulting diffractograms from XRD of Zr+2Si(Room temp, Ign. in fila.) (see Table 3.5). The indicators indicate which phases are attributed to which peaks based on qualitative assessment in Bruker Eva.

Experiment done with Zr+Si sample

Zr+Si(Room temp, Ign. in fila.) (see Table 3.5) was struck by igniter pieces when the igniter exploded which stuck to the sample (see section D.4). Some places that where struck by a piece of the igniter pellet were characterized by either XRD or SEM-imaging in BSE-mode and EDS. The resulting diffractogram from the XRD-characterization is shown in Figure 4.15

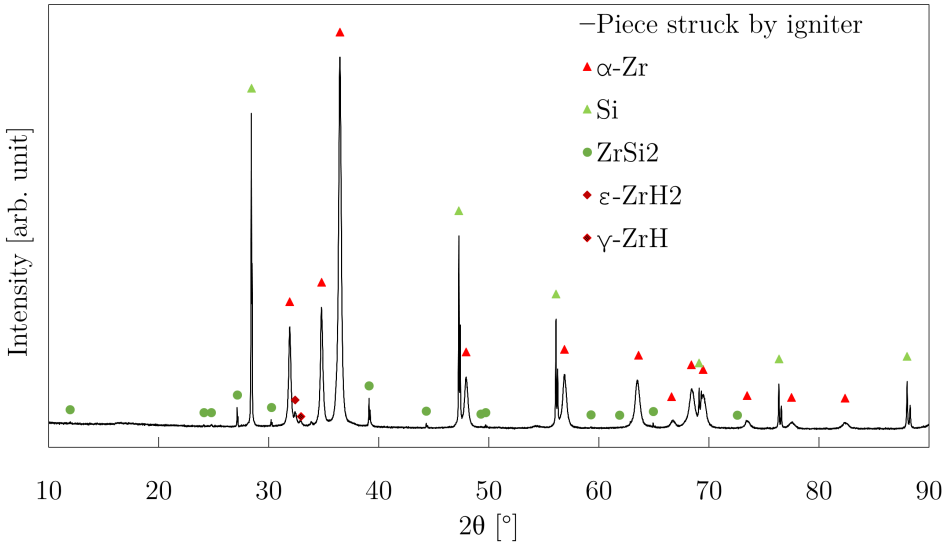

Figure 4.15: Resulting diffractogram from piece of Zr+Si(Room temp, Ign. in fila.) (see Table 3.5) struck by a igniter piece. The indicators illustrate which phases contribute to which peaks during combined Pawley and Rietveld refinement

The composition of the XRD-sample was estimated by combined Pawley and Rietveld refinement. The resulting composition is shown in Table 4.3

Table 4.3: Composition estimated by combined Pawley and Rietveld refinement of the diffractogram shown in Figure 4.15. Rwp and GOF were 7.48 and 3.1

Phase	Amount [mol%]
$ZrSi_2$	1
Si	67
α-Zr	31
ϵ-ZrH_2	<1
γ-ZrH	<1

The results indicate some $ZrSi_2$ had been formed at a point struck by a piece of the igniter. Figure 4.16 shows SEM-images taken in BSE-mode, along with performed EDS-mapping in Figure 4.16a and Figure 4.16d, and points characterized with EDS point-scanning in Figure 4.16b

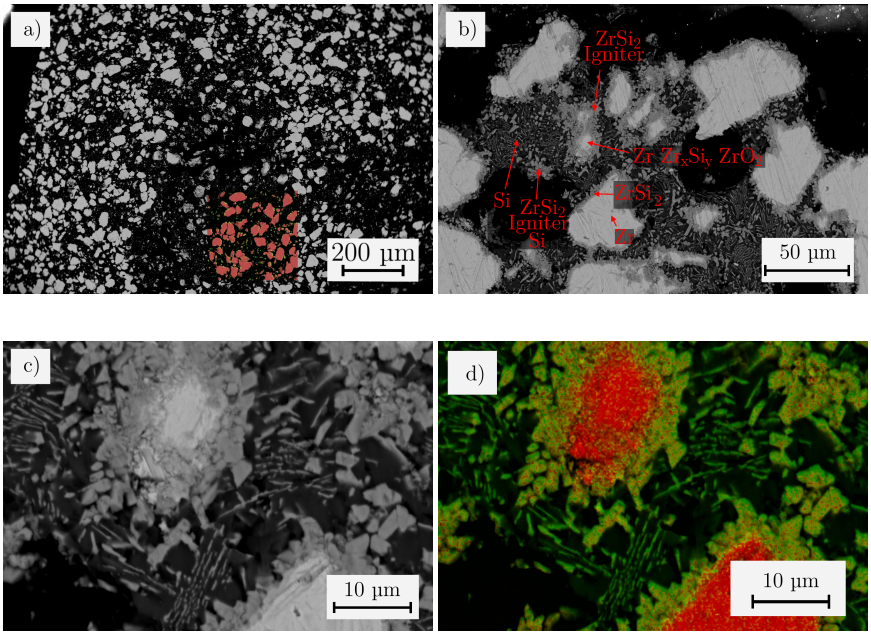

Figure 4.16: SEM-images taken in BSE-mode of a of Zr+Si(Room temp, Ign. in fila.) (see Table 3.5. In the EDS-maps, red indicates zirconium, yellow zirconium silicides, and green silicon. a) shows an overview of the center of the samples, b) shows the edge of the sample where the igniter struck, with points where EDS point scans were done, c) shows a close up of an area in b), and d) shows the same area with an EDS-map overlay

Figure 4.16a shows that the majority of the sample consists of unreacted zirconium and silicon particles. The composition of the assigned phases in Figure 4.16b is shown in Table 4.4

Table 4.4: The result of the EDS point scans of points shown in Figure 4.16b, and what phases are assumed to be present at these points based on the composition. Epoxy, which contributes with a large amount of carbon and a small amount of oxygen, is ignored when assuming which phases are present in each point

	Amount of element [at.%]					
Assigned phase	C	O	Mg	Si	Zr	Ba
Si	17	1	0	74	8	0
$ZrSi_2$, Igniter, Si	34	6	1	42	17	0
$ZrSi_2$, Igniter	42	5	<1	37	16	<1
Zr, Zr_xSi_y, ZrO_2	30	11	0	22	38	0
Zr	31	11	0	0	59	0
$ZrSi_2$	41	5	0	36	18	0

Figure 4.16b indicates that a phase which embeds silicon, zirconium silicides, and zirconium particles has been formed at the contact point with the igniter. Figures 4.16c and 4.16d shows that the embedding phase is silicon with a dendritical shape, and that the zirconium silicides forms a "grainy" phase. The dendritical shape may be due to melting and subsequent precipitation of silicon in molten igniter.

4.3.2 SHS at 600 °C

Experiments done with Zr+2Si samples

The origins of the XRD-samples taken from Zr+2Si(600 °C, Ign. in beam) (see Table 3.5) are illustrated in Figure 4.17.

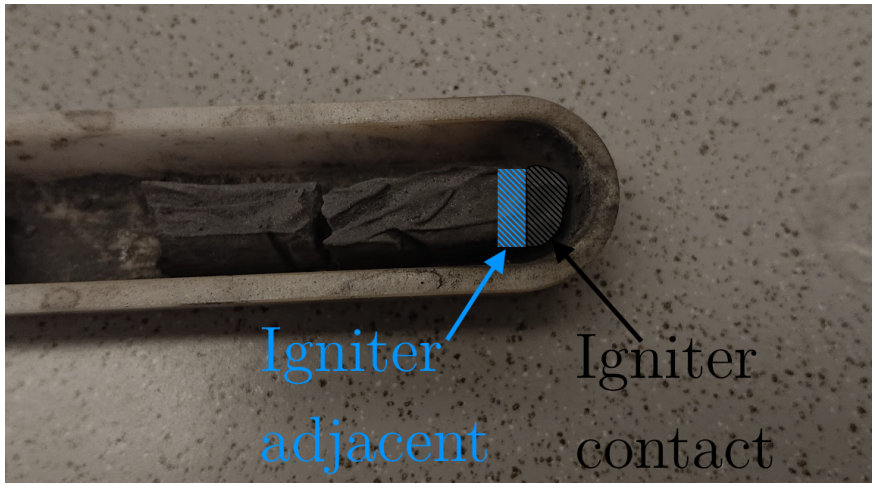

Figure 4.17: Illustrations of XRD-samples taken from Zr+2Si(600 °C, Ign. in beam) (see Table 3.5)

The resulting diffractograms from XRD of the three powder samples are shown in Figure 4.18.

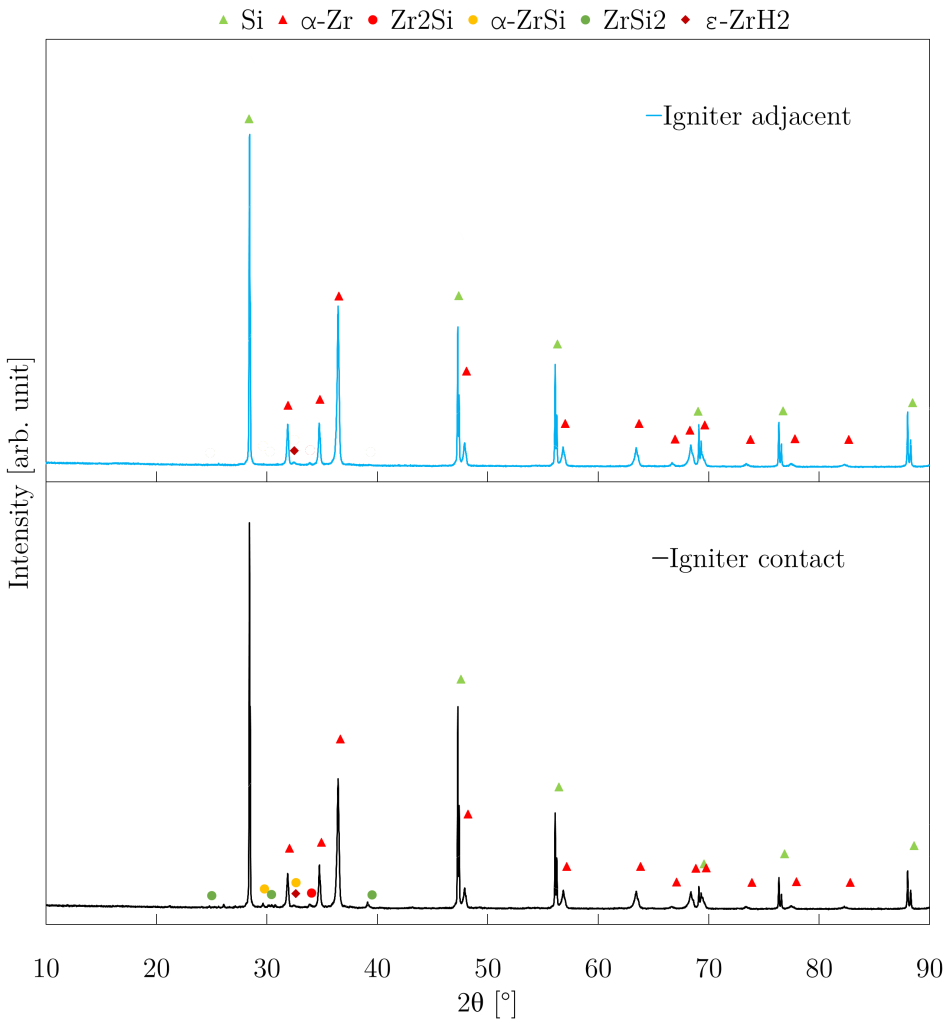

Figure 4.18: Diffractograms taken from powder samples of Zr+2Si(600 °C, Ign. in beam) (see Table 3.5). The indicators illustrate which phase contributed to which peaks during combined Pawley and Rietveld refinement

The composition of the XRD-samples was estimated with combined Pawley and Rietveld refinement. The results are shown in Table 4.5

Table 4.5: Composition estimated by combined Pawley and Rietveld refinement of the diffractograms shown in Figure 4.18. Rwp and GOF were 9.81 and 2.2 for the "Igniter contact"-diffractogram and 13.37 and 3.0 for the "Igniter adjacent"-diffractogram

Compound	Amount [mol%] in Igniter contact	Igniter adjacent
$ZrSi_2$	<1	-
α-ZrSi	<1	-
Zr_2Si	<1	-
α-Zr	9	11
Si	90	89
ϵ-ZrH_2	<1	<1

The results indicate a slight formation of zirconium silicides in the contact point with the igniter, but that there was no propagation.

The sample Zr+2Si(600 °C, Ign. in cylinder) (see Table 3.5 appeared to have been split in two by the exploding igniter (see section D.5). The resulting diffractograms from XRD of the powder samples taken from Zr+2Si(600 °C, Ign. in cylinder) (see Table 3.5) is shown in Figure 4.19

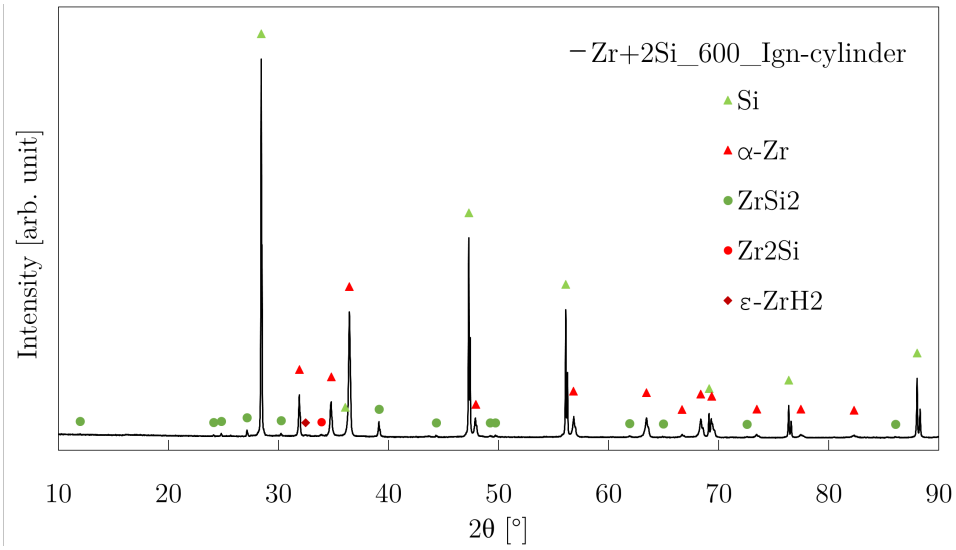

Figure 4.19: Resulting diffractograms from XRD of the powder sampleZr+2Si(600 °C, Ign. in cylinder) (see Table 3.5). The indicators illustrate which phases contributed to which peaks in the combined Pawley and Rietveld refinements

The composition of the XRD-samples was estimated by combined Pawley and Rietveld refinements. The results are shown in Table 4.6.

Table 4.6: Resulting composition from combined Pawley and Rietveld refinement of the diffractogram shown in Figure 4.19. Rwp and GOF were 5.27 and 2.0 respectively

Phase	Amount [mol%]
$ZrSi_2$	1
Zr_2Si	<1
α-Zr	3
Si	95
ϵ-ZrH_2	<1

The results indicate formation of trace amounts of $ZrSi_2$ and Zr_2Si.

Figure 4.20 shows SEM-images taken in BSE-mode of the SEM-sample prepared from Zr+2Si(600 °C, Ign. in cylinder). Figure 4.20b includes an overlay made by EDS-mapping.

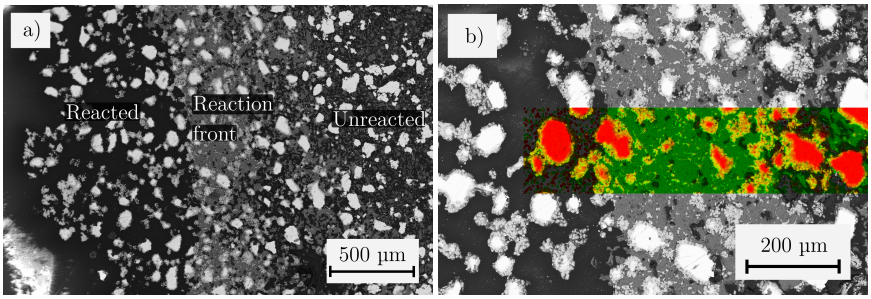

Figure 4.20: The figure shows SEM-images taken in BSE-mode of the sample Zr+2Si(600 °C, Ign. in cylinder) (see Table 3.5). a) shows the difference between the reacted zone, the reaction front, and the unreacted front, and b) is close-up of the reaction front with an EDS-map overlay. In the EDS-map, red refers to zirconium, yellow refers to zirconium silicides, and green refers to silicon

Figure 4.20a depicts three zones with distinctively different microstructures. The different microstructures have been attributed to one zone being reacted, the second zone being a reaction front, and the third zone being unreacted. In the reacted zone, white particles are surrounded by a gray phase. The large amount of epoxy, *i.e.* the black phase, indicates a high degree of porosity before moulding. Figure 4.20b shows that the white particles are zirconium and that the gray phase is zirconium silicides. The second zone consists of white particles embedded in a dense gray phase. Figure 4.20b shows that the dense phase

is silicon, the white particles are zirconium, and that there is a layer of zirconium silicides on the zirconium particles. The dense silicon phase is attributed to melting and subsequent cooling. The third phase consists of white and gray particles, and Figure 4.20b shows that the white particles are zirconium and the gray particles are silicon.

Experiment done with Zr+Si sample

The resulting diffractograms from XRD of the powder sample taken from Zr+Si(600 °C, Ign. in cylinder) (see Table 3.5) is shown in Figure 4.21

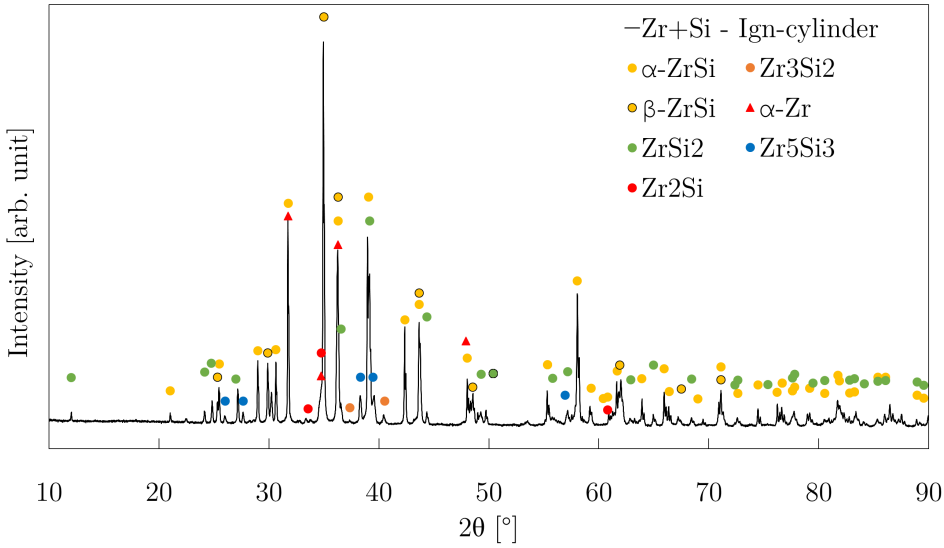

Figure 4.21: Resulting diffractogram from XRD of the powder sample taken from Zr+Si(600 °C, Ign. in cylinder) (see Table 3.5)The indicators illustrate which phases contributed to which peaks in the combined Pawley and Rietveld refinements

The composition of the XRD-sample was estimated by combined Pawley and Rietveld refinements. The results are shown in Table 4.7.

Table 4.7: Resulting composition from combined Pawley and Rietveld refinements of diffractogram shown in Figure 4.21. Rwp and GOF were 10.55 and 4.2 in respectively

Phase	Amount [mol%]
$ZrSi_2$	17
α-ZrSi	55
β-ZrSi	26
Zr_3Si_2	1
Zr_5Si_3	2
Zr_2Si	1
α-Zr	<1

SEM-images taken in BSE-mode are shown in Figure 4.22

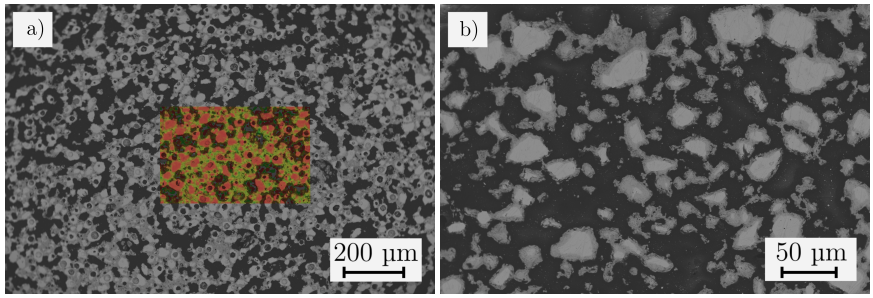

Figure 4.22: SEM-images taken in BSE-mode of a sample taken from Zr+Si(600 °C, Ign. in cylinder) (see Table 3.5) a) shows an area of the microstructure and composition that extended from the edge that was in contact of the igniter and across the majority of the sample. In the EDS-map overlay, red refers to zirconium, yellow refers to zirconium silicides, and green refers to silicon. b) shows an area of the microstructure that extends from the far edge from the igniter contact point and inwards to before the middle of the sample.

The XRD-results indicate a nearly consumption of zirconium an silicon in formation of a wide array of zirconium silicides, including the high-temperature phases β-ZrSi and Zr_5Si_3. The SEM-images reveals that there is unreacted zirconium spread out in the sample. The SEM-results also show that the majority of the sample has a microstructure consisting of relatively small zirconium particles embedded in a matrix of zirconium silicides, while the edge of the cylinder (*i.e.* the part of the sample furthest away from the igniter and most exposed to the furnace atmosphere) had a microstructure consisting of zirconium silicides surrounding larger Zr-particles.

4.3.3 SHS with inherent tube furnace gradient

After the experiment with the sample Zr+2Si($1400\,^{\circ}\mathrm{C}$, Temp. grad.), two different regions with a defined border could be observed. The border was located where the temperature was expected to be 1370–$1376\,^{\circ}\mathrm{C}$ based on the existing measurement of the furnace temperature gradient (see section D.6). These regions were suspected to be a reacted region and an unreacted region, and XRD-samples of the border between the regions and each regions were characterized The resulting diffractograms from XRD of powder these samples are shown in Figure 4.23

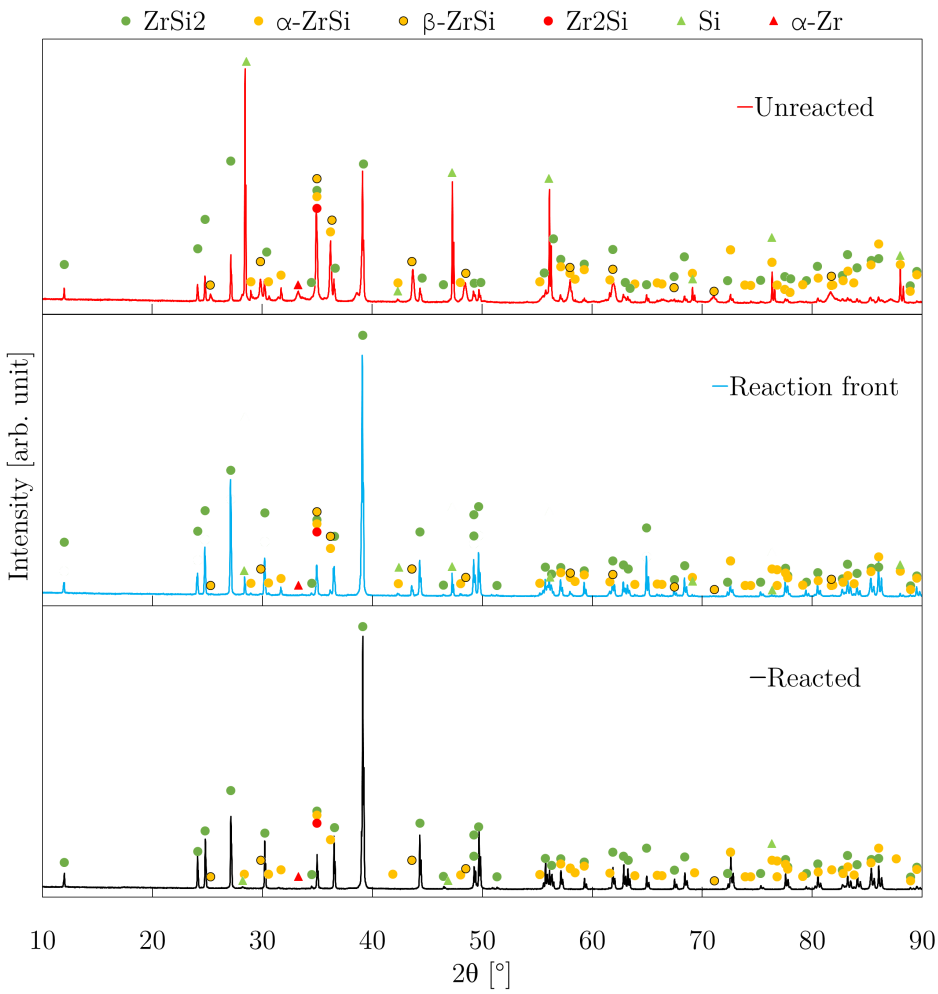

Figure 4.23: Resulting diffractograms of powder samples taken from an alumina ship filled with a lightly compacted attritor-milled Zr+2Si powder mixture which was placed with one end in the center of the tube furnace, after heating to 1391 °C at on end and approximately 1337 °C at the other. The indicators illustrate which phases contributed to which peaks during combined Pawley and Rietveld refinements

The composition of the XRD-samples was estimated with combined Pawley and Rietveld refinement. The results are shown in Table 4.8.

Table 4.8: Resulting compositions from combined Pawley and Rietveld refinements of diffractograms shown in Figure 4.23. *Rwp* and GOF were 10.93 and 4.4 in "Unreacted", 12.56 and 4.8 in "Reaction front", and 14.95 and 5.8 in "Reacted"

	Amount [mol%] in		
Phase	Unreacted	Reaction front	Reacted
$ZrSi_2$	8	66	93
α-ZrSi	3	4	2
β-ZrSi	10	1	<1
Zr_2Si	<1	<1	1
α-Zr	1	<1	4
Si	78	29	<1

'SEM-images were taken in BSE-mode of the top of the sample (*i.e.* side exposed to atmosphere) and the side of the sample, and the areas were also characterized by EDS-mapping. The images with EDS-map overlay are shown in Figure 4.24

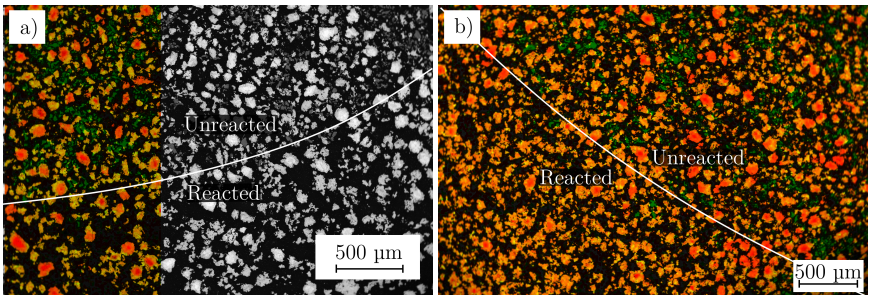

Figure 4.24: SEM-images taken in BSE-mode with EDS-map overlay of samples taken from an alumina ship filled with a lightly compacted attritor-milled Zr+2Si powder mixture which was placed with one end in the center of the tube furnace, after heating to 1391 °C at on end and approximately 1337 °C at the other. In the EDS-maps, red refers to zirconium, yellow refers zirconium silicides, and green refers to silicon

The results indicate that both the regions were reacted to a degree, but the region referred to as the reacted region is more reacted than the unreacted region. The "reacted" region is in fact almost completely reacted. The concentration of $ZrSi_2$ was increased from a minor amount to being the main phase, and the concentration of other zirconium silicides than $ZrSi_2$ is reduced from a significant amount to only trace amounts. Figure 4.24 shows that zirconium silicide is found as a shell-like structure on unreacted zirconium particles in both zones, but that the "unreacted" zone contain unreacted silicon particles opposed to "reacted" region. The absence of silicon particles in the most reacted zone indicates

either complete consumption of silicon or formation of a liquid. The side of the sample, both when studied by the naked aye and when imaged with SEM showed that the "reacted zone" extended longer at the bottom of the sample *i.e.* than at the top of the sample.

4.3.4 Summary of results

Table 4.9: The Zr-Si mixture and experiment configuration used in the SHS-experiments, and the amount of product formed in different ares of the samples. The configurations are described in section 2.1.2

Mixture Configuration	Igniter contact	Igniter adjacent	Rest
Experiments at room temperature			
Zr+2Si Independent igniter	Major amount of $ZrSi_2$	No reaction	-
Zr+2Si Independent igniter	No reaction	No reaction	-
Zr+2Si Press in igniter	No reaction	No reaction	No reaction
Zr+2Si Igniter in filament	No reaction	No reaction	No reaction [a]
Zr+Si Igniter in filament	Small amounts of zirconium silicides	No reation	No reaction
Experiments at 600 °C			
Zr+2Si Igniter in beam end	Trace amounts of Zr_xSi_y	No reaction	No reaction
Zr+2Si Igniter in cylinder center	Major amount of Zr_xSi_y	Minor amount of Zr_xSi_y	No reaction
Zr+Si Igniter in cylinder center	Mainly Zr_xSi_y	Mainly Zr_xSi_y	Mainly Zr_xSi_y
Experiment with furnace temperature gradient at 1400 °C			
	Reacted	Reaction Front	Unreacted
Zr+2Si Termperature gradient	Mainly Zr_xSi_y	Major amount of Zr_xSi_y	Major amount of Zr_xSi_y

4.4 Silicothermic reduction

4.4.1 Oxidation of zirconium powder

The zirconium powder heated to 1500 °C in a synthetic air atmosphere (see section 3.6.1 was characterized by XRD, resulting in the diffractogram shown in Figure 4.25

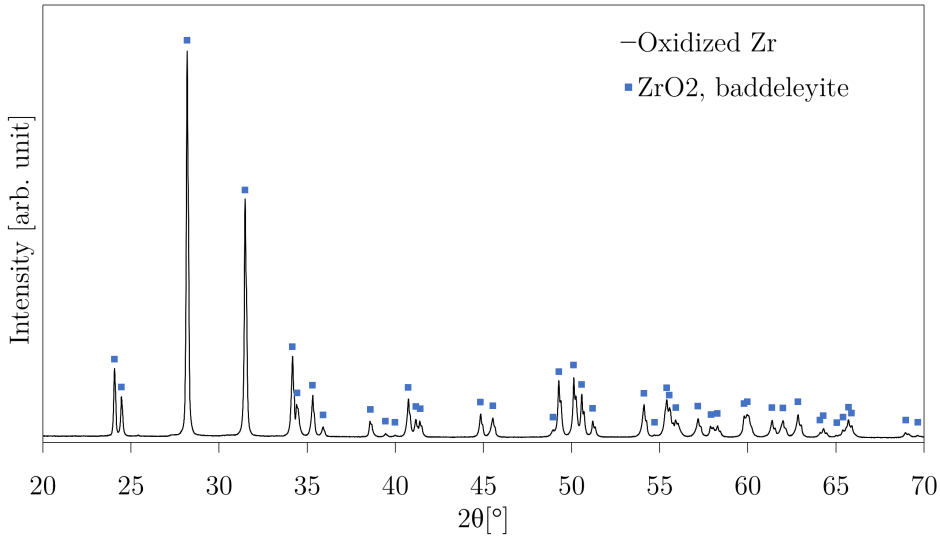

Figure 4.25: Diffractogram from powder XRD of zirconium powder heated to 1500 °C in synthetic air

The diffractogram indicates that the zirconium powder was fully oxidized to ZrO_2 after the heat treatment, which made it possible to isolate the reaction shown in Eq. (2.18) between ZrO_2 and Si from the reaction between zirconium and silicon.

4.4.2 DSC/TGA measurement of siliocthermic reduction

Shortly after reaching the maximum temperature of the DSC/TGA measurements (1550 °C), the platinum sample holder broke, which caused the apparatus to perform an emergency shut-down. Figure 4.26 shows the TGA- and DSC measurements from start to shut-down.

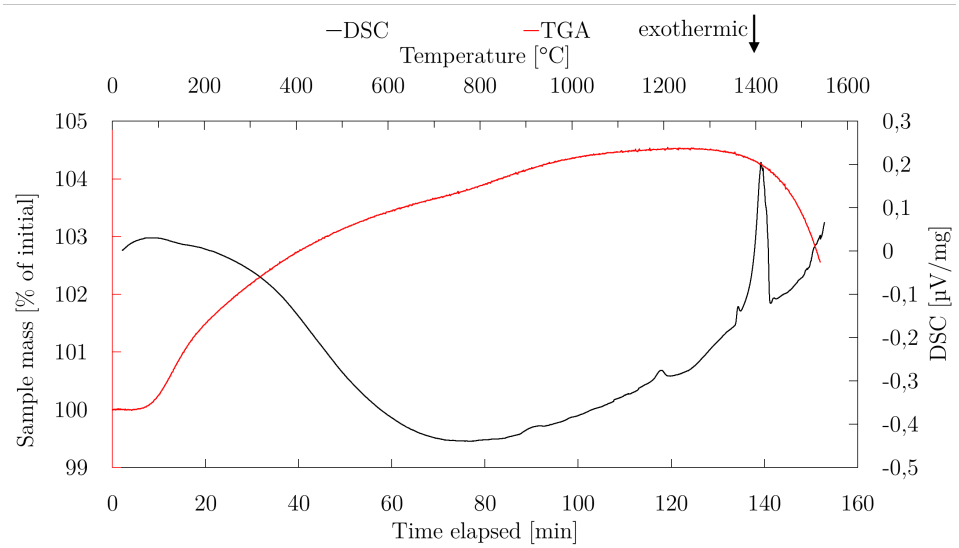

Figure 4.26: DSC/TGA characerization of a ZrO_2 and Si powder mixture in an alumina crucible in argon atmosphere during heating to 1550 °C

Figure 4.26 indicates a large mass loss occurring simultaneously as one or more reactions which is in sum is highly endothermic. The mass loss is attributed to formation of SiO (g) by reduction of ZrO_2 by Si. The absorbed heat is in part attirbuted to this reaction, in addition to melting of silicon. Figure 4.27 shows the resulting diffractogram from powder XRD of the analyzed powder, and which phases makes a major contribution to each peak during the Rietveld refinement.

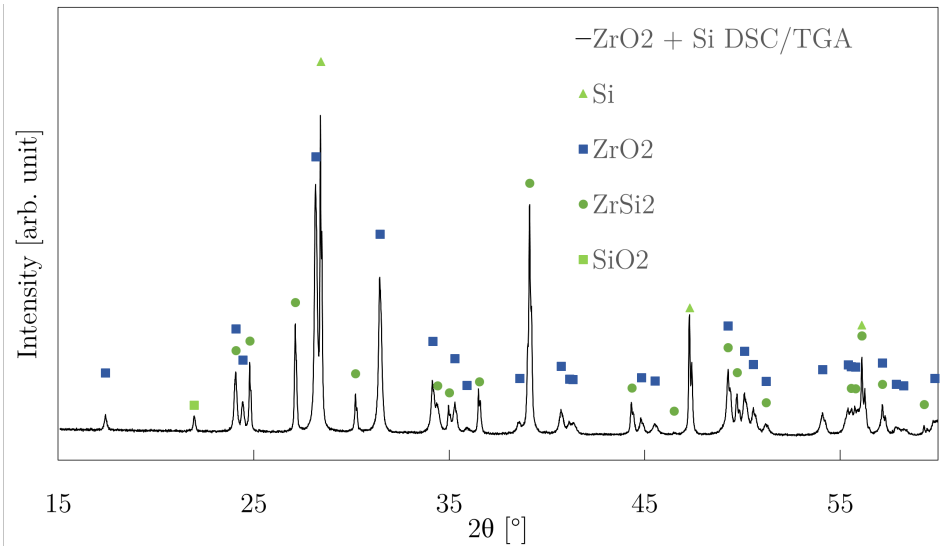

Figure 4.27: Diffractogram from powder XRD of ZrO_2 and Si powder mixture analyzed with TGA/DSC. Which phase(s) contributed to each peaks during Pawley and Rietveld refinement is shown by the indicators

Figure 4.27 shows the resulting diffractogram from XRD of the ZrO_2-Si after the DSC/TGA -measurement. Which phases made a major contribution to each peak during combined Pawley and Rietveld refinement is shown with indicators. The resulting composition is shown in Table 4.10, along with the composition of the sample before the DSC/TGA measurement.

Table 4.10: Composition of ZrO_2-Si sample before DSC/TGA measurement, and after measurement which was given by combined Pawley and Rietveld refinement of the diffractogram shown in Figure 4.27. Rwp and GOF were 8,72 and 2,3 respectively

	Amount [mol%] in	
Compound	Initial mixture	After DSC/TGA
$ZrSi_2$	0	10
ZrO_2	24	21
Si	76	59
SiO_2	0	10
	By elements [mol%]	
Zr	8	10
Si	76	69
O	16	21

The compositions in Table 4.10 show that the amount of elemental silicon was substantially reduced after the DSC/TGA measurement. However, not all the reacted silicon was depleted from the sample, but rather reacted to SiO_2. The $ZrSi_2$ found in the sample after the thermal analysis can only have been formed (at least at measurable level) by reduction of ZrO_2 by silicon as the ZrO_2-powder contained did not contain a measurable amount of Zr.

4.5 Reactivity between zirconium silicides and precursors

The diffractograms of each heat treated sample is given in section E. The resulting composition from combined Pawley and Rietveld refinement of these diffractograms are shown in Table 4.11

Table 4.11: Resulting compositions from combined Pawley and Rietveld refinement of diffractograms of samples generated by the experiments presented in section 3.6.2

	3Zr + Si	$ZrSi_2$+Zr		$Zr_{(3)}Si$ + 5Si	
Max temperature [°C]	1500	1500	1400	1500	1400
Dwell time [h]	1	1	-	1	-
α-Zr [at.%]	29	34	28	-	-
Zr_2Si [at.%]	69	64	42	-	-
Zr_3Si_2 [at.%]	2	2	5	-	-
α-ZrSi [at.%]	-	-	2	3	-
β-ZrSi [at.%]	-	-	23	-	-
$ZrSi_2$ [at.%]	-	-	2	97	100
Diffractogram	Figure E8	Figure E9	Figure E10	Figure E11	Figure E12
Rwp	8.7	16.6	17.07	9.7	10.4
GOF	2.3	3.8	8.2	6.3	6.3

5 Discussion

Since this thesis revolves around SHS, the results of the SHS-experiments will be interpreted and discussed first. These discussions will be divided into reaction completeness, factors that affected ignition of the mixture, and factors that affected the propagation of the reaction. Some figures from the results will be combined and presented to highlight the significance of the results. The following discussions of the results from co-milling of zirconium and silicon, development of SHS-reactor, silicothermic reduction, and reactivity between zirconium silicides and precursors will be tied to the discussions of the SHS-experiments.

5.1 SHS experiments

All together, a self-propagating synthesis of $ZrSi_2$ was not achieved in this thesis. Since the synthesis has been shown to be viable in previous literature, there must be features of the experiments in this thesis that causes sub-optimal synthesis conditions for ignition and propagation of the combustion reaction. Pinpointing these features may give insight on which factors affect the synthesis, and which requirements there are for a self-propagating combustion reaction.

5.1.1 Reaction completeness in different experiments

From the results of the SHS experiments, summarized in Table 4.9, four main types of synthesis completion can be defined:

1. Initiation of silicon melt and formation of zirconium silicides. Observed in SEM-images of Zr+Si(Room temp, Ign. in fila), and assumed to have occured in Zr+2Si(Room temp, Indep. Ign)1 and Zr+2Si(600 °C, Ign. in beam).
2. Ignition of Zr-Si mixture and establishment of combustion front. Observed in SEM-images of Zr+2Si(600 °C, Ign. in cylinder).

3. Ignition of Zr-Si mixture and semi-complete propagation. Observed in SEM-images of Zr+2Si(1400 °C, Temp. grad.).

4. Ignition of Zr-Si mixture and complete propagation. Observed in SEM-images of Zr+Si(600 °C, Ign. in cylinder).

Even though the first type involves formation of zirconium silicides from a silicon melt, it will not be considered as ignition of the Zr-Si mixture as the reactivity was too low to establish a reaction front. SEM-images of the four types are shown in Figure 5.1

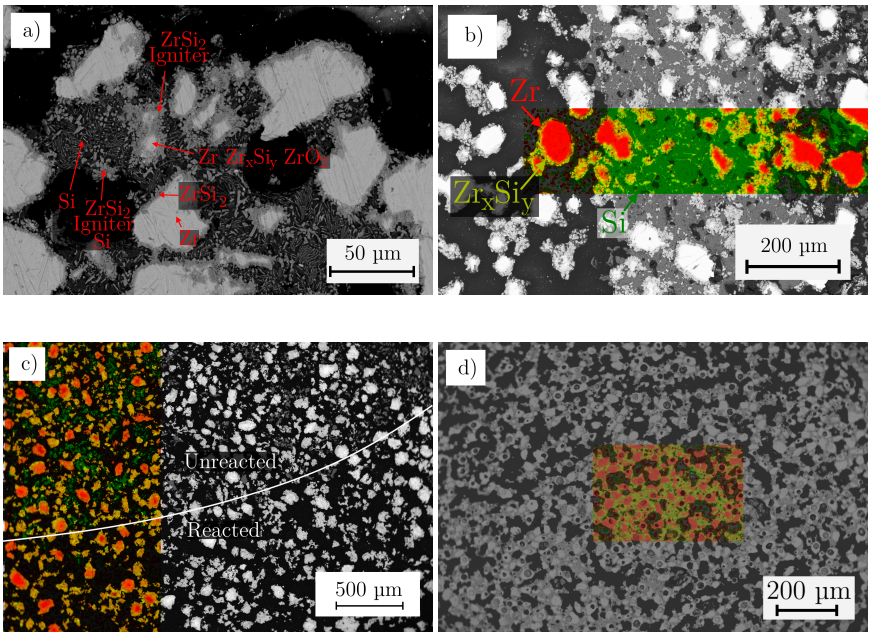

Figure 5.1: SEM-images showing four types of synthesis completion. a) is an image of Zr+Si(Room temp, Ign. in fila.) and depicts initiation of silicon melt and formation of zirconium silicides without ignition in the Zr-Si mixture. b) is an image of Zr+2Si(600 °C, Ign. in cylinder) and depicts combustion at the igniter contact point, and establishment of combustion front adjacent to the igniter, but no propagation. c) is an image of of Zr+2Si(1400 °C, Temp. grad.) and depicts well-defined border between a nearly completely reacted zone and a somewhat reacted zone. d) is an image of Zr+Si(600 °C, Ign. in cylinder) and depicts the microstructure of the nearly fully reacted sample. Experimental details of each sample is given in Table 3.5.

5.1.2 Effect of synthesis temperature and igniter explosivity on the ignition of Zr-Si mixtures

At room temperature, the results indicate that a silicon melt and formation of zirconium silicides was only initiated in samples Zr+2Si(Room temp, Indep. Ign.)1 and Zr+Si(Room temp., Ign. in fila.). A key difference between these samples and the samples that did not react at room temperature was that igniter that appeared to have been melted was stuck to the sample after the experiments. The explosive nature of the igniter was reflected in all these experiments, especially in the unreacted sample Zr+2Si(Room temp, Indep. Ign.)2 where the explosive force was enough to split the alumina tube the sample was contained in (see section D.3). When the igniter was pressed in to the Zr-Si beam as in Zr+2Si(Room temp, Pressed in Ign), it exploded away from the beam and may thus have been unable to transfer a sufficient amount of heat to the Zr-Si sample.

The experiments at $600\,^{\circ}\mathrm{C}$ allowed the pellet to be incorporated into the center of the samples, which was done in samples Zr+2Si($600\,^{\circ}\mathrm{C}$, Ign. in cylinder) and Zr+Si($600\,^{\circ}\mathrm{C}$, Ign. in cylinder). These samples were successfully ignited, which in part can be attributed to better heat transfer from igniter to Zr-Si mixture as the igniter did not explode away. The higher temperature in the samples and tube furnace did also reduce the required heat transmission and the heat dissipation from sample to furnace atmosphere. The contribution of the higher temperature is reflected in the difference between Zr+2Si(Room temp, Pressed in ign.) and Zr+Si($600\,^{\circ}\mathrm{C}$, Ign. in beam) where the only difference between the samples was the temperature the experiment was done at. The sample from the room temperature experiment did not react, while formation of zirconium silicides was initiated in the sample from the experiment at $600\,^{\circ}\mathrm{C}$. In turn, synthesis completion of this sample compared to the synthesis completion of the two other samples at $600\,^{\circ}\mathrm{C}$ indicates that the positive effect of having the igniter contained in the center of the sample was larger than the positive effect of increased synthesis temperature.

5.1.3 Propagation of combustion in a Zr-Si mixture

Effect of heat dissipation, reaction mechanism, and zirconium particle size

The results show that the samples Zr+2Si($600\,^{\circ}\mathrm{C}$, Ign. in cylinder), Zr+Si($600\,^{\circ}\mathrm{C}$, Ign. in cylinder), and Zr+2Si($1400\,^{\circ}\mathrm{C}$, Temp gradient) were successfully ignited and propagation was initiated, but that only sample Zr+Si($600\,^{\circ}\mathrm{C}$) experienced full propagation.

Effect of heat dissipation

Figure 5.1b indicates that heat was dissipated from the combustion front faster than heat was generated as the propagation was extinguished. In the set-up of the SHS-experiments, the tube furnace can in regard to heat transfer be seen as an infinitely large atmosphere compared to the small samples. In addition, the argon flux causes forced convection, which increases the heat transfer. It is likely that heat dissipation from the samples to the furnace atmosphere played a detrimental role in the results of the SHS-experiments. As imaged in Figure D6, Zr+2Si($600\,^{\circ}\mathrm{C}$, Ign. in cylinder) and Zr+Si($600\,^{\circ}\mathrm{C}$, Ign. in cylinder) were cracked upon upon ignition of the igniter, so heat dissipation to the furnace atmosphere

may have played a key role in the extinguishing of the combustion front in Zr+Si(600 °C, Ign. in cylinder).

Effect of reaction mechanism and zirconium particle size

As ZrSi has a lower formation enthalpy than $ZrSi_2$, (see Table 2.2) and subsequently a higher combustion temperature (see Table 2.3) it is expected that the combustion in a Zr+Si mixture is less sensitive than in a Zr+2Si mixture since the ignition in both is caused by formation of the same liquid. However, the difference in reaction mechanism in the Zr+Si mixtures and Zr+2Si mixtures may have a substantial influence. In section 2.6.1 the findings by Bertolino *et al.* [67] and available data on the Zr-Si system was used to determine that the reaction mechanism during combustion of a Zr+Si mixture is a liquid-liquid reaction, and a solid-liquid reaction in Zr+2Si mixture. This is reflected by Figure 5.1b and Figure 5.1d. In Figure 5.1d the unreacted zirconium particles are significantly smaller than in Figure 5.1b, and the zirconium silicide phase is not mainly found as a shell around zirconium particles as in Figure 5.1b. This indicates that the zirconium particles were dissolved in the melt during combustion in the Zr+Si mixture, but not in the Zr+2Si mixture. This makes the Zr+Si mixture less sensitive to the particle size in the zirconium powder since combustion does not rely on diffusion of liquid silicon into the zirconium particles.

The microstructure at the bottom of the Zr+Si(600 °C, Ign. in cylinder) sample was different from the microstructure in the rest of the sample, as shown in Figure 4.22b. This microstructure consisted of larger unreacted zirconium particles surrounded by a zirconium silicide shell, which indicate that combustion in this area did not involve liquid-liquid interaction, but interaction between solid zirconium and liquid silicon. This shows that propagation can occur in a Zr+Si mixture even though the temperature is too low to initiate the liquid-liquid interactions that govern the combustion at ideal conditions. This may be the case for all Zr-Si mixtures that react by liquid-liquid mechanisms. However, the product may contain unreacted zirconium even though the reaction propagates throughout the sample.

Hence, the incomplete propagation in Zr+2Si(600 °C, Ign. in cylinder) can be partly attributed to the zirconium powder particles being too large. A high reaction rate is one of the most important requirements in SHS since the heat generated by the combustion competes with heat dissipation in the sample and to the surroundings, and extended diffusion distance from the molten silicon to the zirconium particles vastly reduces the reaction rate.

The effect of solid-state diffusion

The results of experiment done on sample Zr+2Si(1400 °C, Temp-grad) indicated a clear boundary between a nearly completely reacted zone and a less reacted zone. The microstructure in the sample (imaged in Figure 5.1c) indicates that the unreacted zone only reacted by solid-state diffusion. The figure also illustrates an absence of silicon particles in the most reacted zone, which was attributed to either formation of a liquid or complete reaction of silicon. The complete absence opposed to large presence of silicon particles suggests significantly higher reaction rate in the most reacted zone, which in turn verifies that a liquid was formed. The XRD results show that the the composition in the least re-

acted zone consists of similar amounts of $ZrSi_2$ and ZrSi, while the most reacted zone is almost pure $ZrSi_2$. This indicates that the main differences between the zones is a more complete reaction between silicon and zirconium, and reaction between ZrSi and Si to form $ZrSi_2$ by the reaction shown in Eq. (2.21).

The temperature in most of the sample, including at the boundary, is expected to have been above the ignition temperature of Zr-Si mixtures. This leads to ambiguation on how the boundary occurred. One possibility is that the hottest part of the mixture, *i.e.* the side of the sample that was in the middle of the furnace was ignited and the combustion propagated outwards where the temperature was below the ignition temperature until the propagation stopped and thus creating the boundary. Another possibility is that the reaction did not propagate due to the dissipation of heat to the furnace atmosphere being equal to the generation of heat during combustion, and that each part of the sample reacted when it reached the ignition temperature by heating from the furnace. Since the reacted zone was longer in the bottom of the sample than the top of the sample, there has probably been propagation at least at the bottom. Either way, the results give some interesting insight into the negative effect of solid-state diffusion before ignition.

As discussed in section 2.6.1 and illustrated in Eq. (2.19), Eq. (2.20), and Eq. (2.21), the products of solid-state diffusion reduces the exothermicity of combustion as the reaction enthalpies for formation of $ZrSi_2$ between zirconium silicides and silicon is less negative than the reaction enthalpy between zirconium and silicon. This leads to less release of reaction heat during combustion, and hence a lower combustion temperature and less heat supplied to adjacent mixture. The fact that there was insufficient generated heat to propagate the reaction across a temperature gradient of a little over $50\,^{\circ}\mathrm{C}$ reflects the loss of exothermicity in the mixture.

The maximum temperature in the furnace atmosphere at the point of the boundary is estimated to have been 1370–$1376\,^{\circ}\mathrm{C}$, which is significantly above the ignition temperature of $1356\,^{\circ}\mathrm{C}$ in the preceding work for this thesis. The heating rate during the investigation of ignition temperature in the preceding work was three times faster than the heating rate in the temperature gradient experiment in this thesis, so less solid-state diffusion products is expected. As previously discussed, this results in a more reactive mixture. Since melting occurs gradually over a temperature interval, this difference in ignition temperature suggests that less liquid was required for ignition in the preceding work than in the temperature gradient experiment in this thesis, which reflects the difference in reactivity in the mixtures. All in all, the difference in ignition temperatures indicates that extensive solid-state diffusion may increase the ignition temperature. The most viable way of decreasing the solid-state diffusion before ignition in combustion synthesis, including both volume synthesis and self-propagating synthesis, is to increase the heating rate. As the heating rate in the tube furnace utilized in this experiment was only $200\,^{\circ}\mathrm{C\,h^{-1}}$, it should be manageable to achieve far less solid-state diffusion than what was observed in Zr+2Si($1400\,^{\circ}\mathrm{C}$, Temp. grad.).

5.1.4 SHS of $ZrSi_2$ compared to SHS of $MoSi_2$

Of all the challenges related to SHS of $ZrSi_2$, only the sensitivity to zirconium particle size stands out as a bigger challenge in $ZrSi_2$ than in $MoSi_2$. The other challenges – explosivity in igniter, depletion of supplied heat, and reduced exothermicity from solid-state diffusion – are expected to have nearly the same negative effect on SHS of $MoSi_2$ based on the information presented in section 2.5.1.

5.2 Co-milling of zirconium and silicon

The XRD characterization of the attritor-milled Zr+2Si mixtures shows that isopropanol is a viable milling dispersant, as neither zirconium or silicon reacted (see Figure 4.5). The results also illustrate the influence of size of the milling medium, as the zirconium particles were extensively flattened when $5\,\mathrm{mm}$ balls were used, but not when $2\,\mathrm{mm}$ balls were used. As discussed in section 2.6.1, an advantage of the flattening is that the mixture can become more active, but there are advantages related to further pre-treatment of the powder. It is therefore important to be able to predict if flattening will occur or not, and these results illustrate the influence of the chosen milling media.

The peak broadening observed in zirconium can be attributed to microscopic strain, which is more likely to occur in the ductile zirconium than the brittle easily crushed silicon, which in turn is reflected in the lack of peak broadening in silicon. Broadening of one silicon peak was observed, but peak broadening caused microscopic strain should be independent of the crystallographic planes. The extinguishing of the combustion front observed in an ignited Zr+2Si mixture shown in Figure 5.1b was partly attributed to the large size of the zirconium particles causing an insufficient reaction rate. To further reduce the particle size in an attritor-mill, which is a convenient milling apparatus for milling on a large scale, the force subjected to mixture may be increased and the size of milling media can be decreased. Additionally, the hydride-dehydride process described in section 2.4.3 can be utilized to embrittle zirconium easier and hence make it more millable. This process does however require heating of the mixture to liberate the hydrogen, but the added heat could be utilized if the SHS is done while mixture is still hot after hydrogen liberation. As explained in section 2.4.3, hydrogen is completely liberated at $800\,^{\circ}\mathrm{C}$, which would be unusually high as a pre-heating temperature in SHS, and if extended time at this temperature is required for complete liberation, solid-state diffusion may occur to a significant extent in the mixture. However, it may not be necessary to liberate all the hydrogen before synthesis as the zirconium may be sufficiently reactive even with a significant concentration of dissolved hydrogen, and the combustion heat may liberate the rest of the hydrogen gas.

5.3 The SHS-experiment set-up

The thermal analysis of the Mg-BaO_2 mixture and the glow observed in the heating filament during current flow is shown in Figure 5.2.

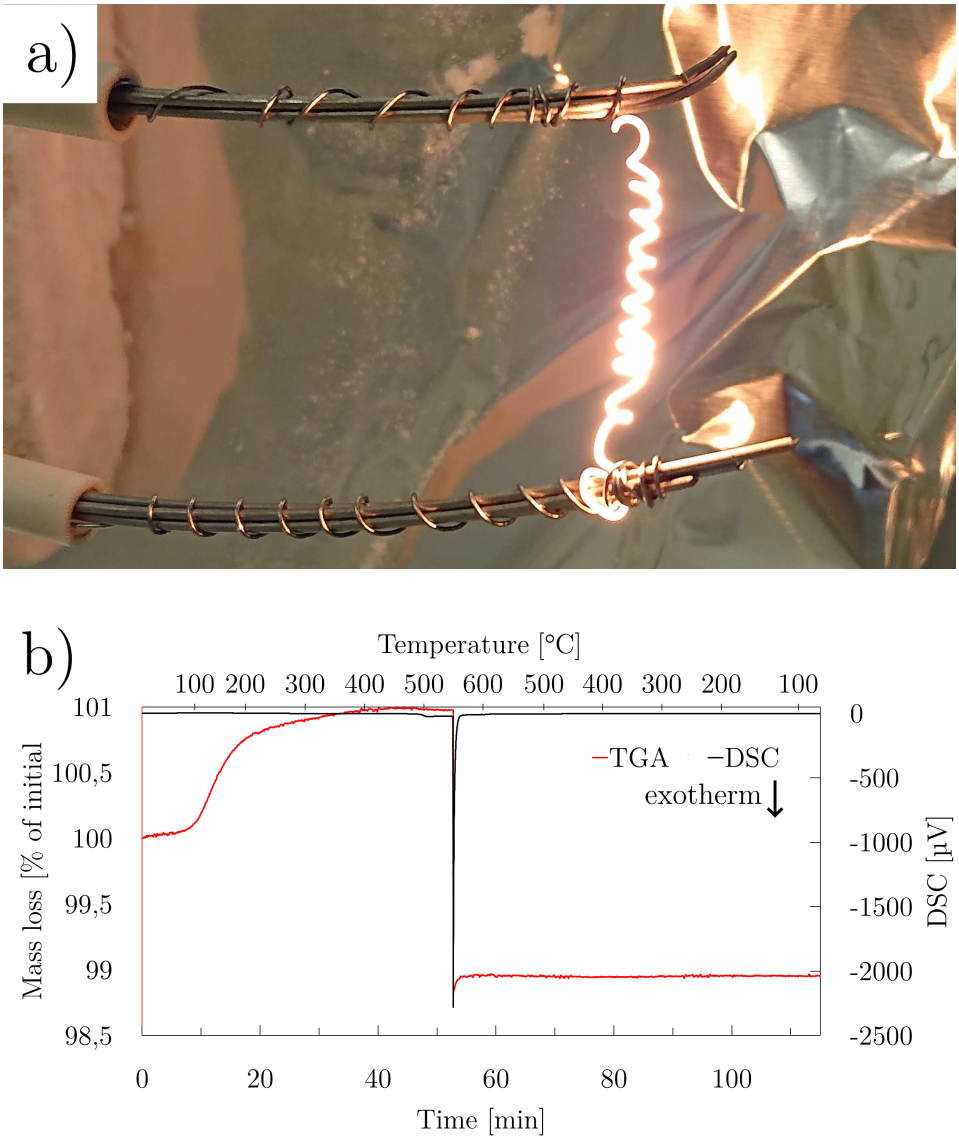

Figure 5.2: Results of pre-experiment leading to the conclusion that resistive heating combined with chemical ignition could be used in the room temperature SHS experiments. a) shows the observed glow in a Kanthal A filament when a voltage of 11 V was applied, and b) shows a DSC/TGA-analysis of a Mg-BaO_2 powder mixture heated to 600 °C and cooled back down

The almost white glow observed in the filament and the highly exothermic ignition of the chemical igniter at $550\,^{\circ}\mathrm{C}$lead to the conclusion that the combination of the two could achieve high enough temperature to ignite the Zr+2Si mixture with the voltage and amperage that could be applied by the available equipment. As discussed in section 5.1.2, this was confirmed by the results of the SHS-experiments, but also indicated that the explosivity reflected in the TGA-curve in Figure 5.2b was a disadvantage. In fact, in the experiments where the Zr-Si was not ignited, this was mainly attributed to the explosivity of the igniter. As discussed in section 2.2.2, the release of oxygen gas could be reduced by increasing the reaction rate of oxidation of magnesium *e.g.* by using a finer magnesium powder. However, since the igniter seemed to melt when ignited but still exploded due to rapid release of oxygen gas, the effect of decreased magnesium particle size can be considered insufficient.

Explosivity may be a common challenge when using chemical igniters in general, as the reaction they utilize often produce a gas. As discussed in section 5.1.2, encapsulating the igniter so it does not explode away from the Zr-Si mixture increases the efficiency. Therefore, chemical igniters may be more effective in a compact set-up where exploding igniter is restricted to be within or in contact with the sample. In such a configuration, the sudden pressure increase from the igniter may even give a shock wave effect. This was presented as an independent way of ignition in section 2.1.2, so the combined pressure increase and heat release from a chemical igniter could be beneficial if well-utilized in SHS.

5.4 Silicothermic reduction

5.4.1 Reactivity

The results in section 4.4 gives some insight on the reactivity of silicothermic reduction at the temperatures achieved during SHS. The reaction shown in Eq. (2.18) was successfully isolated as zirconium powder used in the experiment was completely oxidized. Thus, the presence of a substantial amount of $ZrSi_2$ after the thermal analysis indicates that ZrO_2 must have been reduced by silicon. Even though the composition of the sample (ZrO_2 + 3Si) was less silicon-rich than the stoichiometric composition corresponding to complete reaction to $ZrSi_2$ (ZrO_2 + 4Si), no other silicides than $ZrSi_2$ were indicated by XRD. This reflects that the reduction of ZrO_2 was incomplete, but may also indicate that the reaction between zirconium and silicon to form $ZrSi_2$ is faster than the reduction of ZrO_2 and silicon.

5.4.2 Relevance for SHS

The results of the thermal analysis of the ZrO_2+3Si mixture and the subsequent XRD characterization shows that the reactivity is significant at the temperatures achieved during SHS, and that the reaction absorbs heat and depletes silicon either by evaporating it out the sample as SiO(g). If the produced SiO(g) was to be contained within the sample, it may self-react to form Si and SiO_2 which reduces silicon depletion but introduces SiO_2 impurities. The quantitative XRD results shows that the reaction is incomplete, which should be

expected from the low vapor pressure of SiO in the reaction (see Figure 2.10. The effect of silicothermic reduction during SHS could not be estimated from the results of the SHS experiments as the experiments were mostly unsuccessful in achieving complete combustion. Based on the results from the isolated experiments on silicothermic reduction, it is expected to have a low effect on SHS due to the relatively low oxide content in zirconium and silicon powders.

5.5 Reactivity between zirconium silicides and precursors

5.5.1 Reactivity of silicon versus reactivity of zirconium

The results in Table 4.11 indicate that when heated to $1500\,^{\circ}\mathrm{C}$ and held for 1 hour, zirconium reacts completely with the existent zirconium silicides. At these conditions, solid-state diffusion is fast enough to facilitate the complete reactions as the samples are at a temperature above $1000\,^{\circ}\mathrm{C}$ for six hours ($200\,^{\circ}\mathrm{C\,h^{-1}}$ heating and cooling rate). However, when only heating to $1400\,^{\circ}\mathrm{C}$ and cooling back down without dwelling the product of the reaction between zirconium and zirconium silicides changed significantly. Specifically, the results indicate that less Zr_2Si and ZrSi was present in the final product as opposed to the experiment at $1500\,^{\circ}\mathrm{C}$. Similar results were obtained by Bertolino *et al.* [67] in experiments with diffusion couples. They found that only $ZrSi_2$ and ZrSi was formed at the Zr-Si interface up to $1570\,^{\circ}\mathrm{C}$, where Zr_2Si. This indicates that the temperature in the sample must have exceeded the furnace temperature in the heat treatment of zirconium and zirconium silicide by a significant amount. As discussed in section 5.1.3 this is unlikely, but the trend is similar to the findings by Bertolino *et al.* [67].

The reaction between silicon and zirconium silicides is essentially completed at both $1500\,^{\circ}\mathrm{C}$ with 1 hour dwell and at $1400\,^{\circ}\mathrm{C}$ with no dwell. Thus, silicon appears to be more reactive with zirconium silicides than zirconium with zirconium silicides at $1400\,^{\circ}\mathrm{C}$ which can be attributed to the presence of a silicon melt or silicon-rich eutectic. The superior reactivity of silicon is also reflected in that no Zr_3Si was formed during heating of 3Zr+Si to $1500\,^{\circ}\mathrm{C}$ with one hour dwell.

5.6 Relevance to SHS

The results show that at the temperatures achieved during SHS of $ZrSi_2$, silicon is significantly more active than zirconium in the formation of zirconium silicides. The results from heat treatment of silicon of with zirconium silicides support the observations that zirconium-rich silicides formed by solid-state diffusion before ignition can be re-reacted with silicon to form $ZrSi_2$ in the combustion front. The results from heat treatment of zirconium with zirconium silicides is not of much interest in SHS of $ZrSi_2$, but may be of interest in SHS of the other more zirconium rich silicides.

At optimal conditions, synthesis of other zirconium silicides than $ZrSi_2$ achieves a high enough temperature to melt both silicon and $ZrSi_2$, and some even reach a high enough temperature to melt zirconium and some zirconium rich silicides. However, extensive

solid-state diffusion can reduce the combustion temperature. Dalene [6] and Bertolino *et al.* [67] found that $ZrSi_2$ is formed during solid-state diffusion. If the combustion temperature has been lowered to below the melting point of $ZrSi_2$, which is the case in the experiments between zirconium and zirconium silicides in this thesis, reaction of $ZrSi_2$ with the zirconium to form the desired product must happen through solid-state diffusion. As shown in the experiment where zirconium and zirconium silicides were heated to $1400\,^{\circ}\mathrm{C}$ and cooled back down with no dwelling, this reaction is likely to be incomplete and the product may therefore be impure.

To summarize, "addition" of zirconium to "wrong" zirconium silicides that have been formed before ignition is more difficult than "addition" of silicon to "wrong" zirconium silicides, which makes SHS of zirconium-rich silicides more vulnerable to impurities formed by solid-state diffusion.

Remarks on SEM results of Zr+2Si_RT_Ign-in-fila: The results indicate that zirconium silicides only were formed in the contact point with the igniter, and that this formation was initiated by melting of silicon by the igniter mixture. The microstructure of the zirconium silicides have a "grainy" appearance, and the phase is mostly located around unreacted zirconium.

Remarks on igniter explosion in Zr+2Si_RT_Indep-Ign1 Even though the DSC/TGA-analysis of the igniter with magnesium powder does not reflect this behaviour (see Figure 3.7) this behaviour is well-reflected in the DSC/TGA-analysis of the igniter with magnesium powder and the melt can be attributed to melting of the igniter reactants. Both the increase in oxygen release and melting of reactants can in turn be attributed to the rapid exothermic reaction between magnesium and BaO_2.

6 Conclusions

6.0.1 Factors causing incomplete SHS

Synthesis of $ZrSi_2$ in the reactor developed in this thesis was unsuccessful. This has been attributed to:

- Insufficient heating of the Zr-Si mixtures by the Mg-BaO_2 igniter. It was shown that the igniter reached a high enough temperature to ignite the mixtures, but that to much of the generated heat was dissipated due to the explosive nature of the igniter. The use of the chemical igniter could however be promising in a more compact set-up as it can offer ignition by both heating and shock wave
- Dissipation of heat from Zr-Si mixtures and into the furnace atmosphere was considered to have a detrimental effect on the ignition and propagation of the combustion reaction due to the small samples compared to the atmosphere and the forced convection caused by the argon flux.
- Insufficient milling of zirconium in Zr-Si mixtures. The high sensitivity to zirconium particle size was shown to be related to the reaction mechanism in the combustion formation of $ZrSi_2$ as propagation of the combustion formation of ZrSi was successful. The combustion formation mechanism of ZrSi resembles the combustion formation mechanism in $MoSi_2$, which indicates the SHS of $ZrSi_2$ is more senstive to zirconium particle size than SHS of $MoSi_2$.
- Reduced exothermicity from solid-state diffusion before ignition. It was shown that extensive solid-state diffusion before ignition reduced the exothermicity of a Zr+2Si mixture to the extent that the "combustion" was unable to release heat quicker than the heat was dissipated to an argon atmosphere with a temperature only some tens of °C lower than the ignited sample. The experiment where this effect was observed is not especially representative of SHS, and the effect is expected the pre-heating temperature is high and the heating rate is slow, or for volume synthesis with a low heating rate.

- Most of these factors are expected to be accounted for in large-scale SHS, and are therefore not considered to be detrimental for development of large-scale SHS of $ZrSi_2$. $MoSi_2$ has been produced on a large scale by SHS, and only the sensitivity to the metal particle size (Mo or Zr) is expected to be of higher significance in synthesis of $ZrSi_2$. Large zirconium particles can be accounted for by increased milling force, reduced milling medium, or embrittlement of zirconium during milling by the hydride-dehydride process.

6.0.2 Reactions general for the Zr-Si system

Silicothermic reduction and reactivity between zirconium silicides and zirconium or silicon was studied. Some conclusions can be drawn from these experiments:

- Silicothermic reduction was shown to be a possible parasite reaction during combustion in the Zr-Si system that absorbs heat and depletes silicon. Due to the relatively low oxide content and the low yield of silicothermic reduction, it is expected to have a negligible effect on SHS, but the effect will increase with increasing amount of particle surface oxides.
- $ZrSi_2$ is expected to be most vulnerable to being "deactivated" by solid-state diffusion of all the zirconium silicides as it has the lowest combustion temperature, but is expected to be the least vulnerable to presence of zirconium silicide impurities formed by solid-state diffusion in the final product, given that the combustion is fully propagated through the sample. However, the effect of this on SHS at room temperature is considered to be negligible as there will too little time for solid-state diffusion to occur in a significant degree before combustion.

7 Further Work

7.1 Future studies of SHS of $ZrSi_2$

Based on the results of this thesis, future studies of SHS of zirconium silicides should utilize a more compact SHS-reactor. That is, the sample should completely fill the reactor, so the green reactive mixtures can be reacted directly without pre-synthesis pressing, the dissipation of heat is reduced, and explosive chemical igniter can be used for ignition without dissipation of the heat generated by the igniter. A more repeatable and robust SHS synthesis is required to study the possible effect of silicothermic reduction as well. Other heating techniques should be studied as well. Laser heating could be a promising alternative as it can be extremely rapid, which can make it easier to study the ignition and propagation in detail. Microwave heating has a poor performance at low temperature but its performance increases with temperature, and especially in silicon as this is a semiconductor. So, applying microwave heating after a sample is ignited by another technique can make the combustion wave more robust while maintaining the steep temperature gradient between reaction front and unreacted mixture. This can be especially helpful as the combustion temperature in $ZrSi_2$ is close to the ignition temperature.

7.2 Large scale synthesis of $ZrSi_2$ by SHS

Based on the literature review and the conclusions drawn from the experiments, some ideas regarding an efficient large scale synthesis route of $ZrSi_2$ have emerged.

7.2.1 SHS from ZrH_2 and Si

Since it was concluded that zirconium was insufficiently milled before SHS, it may be necessary to utilize the the hydride-dehydride technique to obtain sufficiently small zirconium particles. As discussed in section 5.2the temperature where hydrogen is completely liberated is higher than what is usually used for pre-heated SHS. However, SHS

with 600 °C, only 200 °C was used in this thesis without signs of detrimental solid-state diffusion. Additionally, complete dehydration may not be required to obtain sufficiently reactive zirconium, and the combustion will liberate hydrogen. However, since the liberation of hydrogen is an endotherm reaction it may be absorb significant heat from the combustion wave.

All in all, the required hydration to achieve sufficient embrittlement and the required dehydration to achieve sufficient reactivity would be important to optimized, which may require empiric studies of the proposed synthesis route.

7.2.2 SHS from ZrO_2 and Si

An interesting study was done by Cho *et al.* [72], who synthesized $ZrSi_2$ from $ZrSiO_4$, SiO_2, and Mg through a thermite type reaction. This reaction requires a large amount of magnesium, and results in impurities of ZrSi. However, by using silicon instead of SiO_2, the required amount of magnesium is reduced. $ZrSiO_4$ is one of the main raw materials used to produce zirconium, and the process that is used (Kroll process), involves redcution of $ZrCl_2$by magnesium [34]. So from a standpoint of atom economy, the consumption of magnesium in this SHS reaction is justified. Additionally, the use of silicon instead of SiO_2 may result in a purer product as SiO_2-reduction step is removed which makes the silicon more available for reaction, and there is less risk of formation of $SiO(g)$ from reduced silicon and SiO_2.

Considering the complete route from raw materials to $ZrSi_2$, this reaction route bypasses the refinement process of zirconium from raw materials, which may result in substantial economic and energetic savings.

Bibliography

[1] M. E. Schlesinger, "Thermodynamics of Solid Transition-Metal Silicides", *Chem. Rev.*, vol. 90, no. 4, pp. 607–628, Jun. 1990, ISSN: 15206890. DOI: 10.1021/cr00102a003.

[2] H. Yeom, B. Maier, R. Mariani, D. Bai, and K. Sridharan, "Evolution of multilayered scale structures during high temperature oxidation of ZrSi2", *J. Mater. Res.*, vol. 31, no. 21, pp. 3409–3419, Nov. 2016, ISSN: 20445326. DOI: 10.1557/jmr.2016.363.

[3] Z. Yao, J. Stiglich, and T. S. Sudarshan, "Molybdenum silicide based materials and their properties", *J. Mater. Eng. Perform.*, vol. 8, no. 3, pp. 291–304, Jun. 1999, ISSN: 10599495. DOI: 10.1361/105994999770346837.

[4] X. Chen and C. Liang, "Transition metal silicides: fundamentals, preparation and catalytic applications", *Catal. Sci. Technol.*, vol. 9, no. 18, pp. 4785–4820, 2019, ISSN: 2044-4753. DOI: 10.1039/c9cy00533a.

[5] H. Yeom, B. Maier, R. Mariani, D. Bai, P. Xu, and K. Sridharan, "Development of zirconium-silicide coatings for accident tolerant zirconium-Alloy fuel cladding", in *Int. Congr. Adv. Nucl. Power Plants, ICAPP 2016*, vol. 3, 2016, pp. 2126–2131, ISBN: 9781510825949.

[6] J. M. Dalene, "Combustion synthesis of zirconium silicdes", Department of Materials Science, Engineering, NTNU – Norwegian University of Science, and Technology, Project report in TMT4500.

[7] E. A. Levashov, A. S. Mukasyan, A. S. Rogachev, and D. V. Shtansky, "Self-propagating high-temperature synthesis of advanced materials and coatings", *Int. Mater. Rev.*, vol. 62, no. 4, pp. 203–239, May 2017, ISSN: 17432804. DOI: 10.1080/09506608.2016.1243291.

[8] A. Varma, A. S. Rogachev', A. S. Mukasyan, and S. Hwang, "Combustion Synthesis of Advanced Materials: Principles and Applications", in *Adv. Chem. Eng.* Elsevier, 1998, ch. Combustion.

[9] Z. Chunping and Z. Kaifeng, "Pulse Current Auxiliary Sintering", in *Sinter. Appl.* InTech, Feb. 2013, ch. 9, pp. 201–227. DOI: 10.5772/53469.

[10] I.-Y. Ko, J.-H. Park, J.-K. Yoon, K.-S. Nam, and I.-J. Shon, "ZrSi2–SiC composite obtained from mechanically activated ZrC + 3Si powders by pulsed current activated combustion synthesis", *Ceram. Int.*, vol. 36, no. 2, pp. 817–820, Mar. 2010, ISSN: 0272-8842. DOI: 10.1016/J.CERAMINT.2009.09.046.

[11] J.-H. Park, K.-S. Nam, B.-S. Lee, W.-B. Kim, and I.-J. Shon, "High frequency induction heated synthesis and consolidation of nanostructured ZrSi2 from mechanically activated (Zr+2Si) powders", *J. Ceram. Process. Res.*, vol. 10, no. 1, pp. 85–89, 2009.

[12] E. J. Davies, *Conduction and Induction Heating*, ser. Energy Engineering 2. P. Peregrinus Limited, 1991, vol. 5, p. 51, ISBN: 9780863411748. DOI: 10.1049/pe:19910014.

[13] D. Sands, "Pulsed Laser Heating and Melting", in *Heat Transf. - Eng. Appl.* InTech, Dec. 2011. DOI: 10.5772/28736.

[14] Y. X. Li, J. D. Hu, H. Y. Wang, Z. X. Guo, and A. N. Chumakov, "Thermodynamic and lattice parameter calculation of TiCx produced from Al-Ti-C powders by laser igniting self-propagating high-temperature synthesis", *Mater. Sci. Eng. A*, vol. 458, no. 1-2, pp. 235–239, Jun. 2007, ISSN: 09215093. DOI: 10.1016/j.msea.2006.12.075.

[15] R. J. Meredith and I. o. E. Engineers, *Engineers' Handbook of Industrial Microwave Heating*, ser. Energy Engineering Series. Institution of Electrical Engineers, 1998, ISBN: 9780852969168.

[16] S. G. Nishvili, D. Agrawal, and R. Roy, "Microwave combustion synthesis and sintering of intermetallics and alloys", *J. Mater. Sci. Lett.*, vol. 18, pp. 665–668, 1999. DOI: 10.1023/A:1006671507193.

[17] V. V. Barzykin, "Initiation of SHS processes", Tech. Rep. 7, 1992, pp. 909–918.

[18] I. I. Volnov, *Peroxides, Superoxides, and Ozonides of Alkali and Alkaline Earth Metals*. Springer US, 2012, ISBN: 9781468482522.

[19] A. G. Blackman and L. R. Gahan, *SI Chemical Data*, 7th ed. Jon Wiley & Sons, 2014, ISBN: 9780730302469.

[20] V. D. Hogan and S. Gordon, "Pre-ignition and Ignition Reactions of the System Barium Peroxide–Magnesium–Calcium Resinate", *J. Phys. Chem.*, vol. 61, no. 10, pp. 1401–1405, 1957, ISSN: 0022-3654.

[21] A. S. Rogachev and A. S. Mukasyan, *Combustion for Material Synthesis*. CRC Press, 2014, ISBN: 9781482239522.

[22] A. G. Merzhanov and I. P. Borovinskaya, "Historical retrospective of SHS: An autoreview", *Int. J. Self-Propagating High-Temperature Synth.*, vol. 17, no. 4, pp. 242–265, Dec. 2008, ISSN: 1061-3862. DOI: 10.3103/s1061386208040079.

[23] X. Su, F. Fu, Y. Yan, G. Zheng, T. Liang, Q. Zhang, X. Cheng, D. Yang, H. Chi, X. Tang, Q. Zhang, and C. Uher, "Self-propagating high-temperature synthesis for compound thermoelectrics and new criterion for combustion processing", *Nat. Commun.*, vol. 5, Sep. 2014, ISSN: 20411723. DOI: 10.1038/ncomms5908.

[24] K. G. Shkadinskii, B. I. Khaikin, and A. G. Merzhanov, "PROPAGATION OF A PULSATING EXOTHERMIC REACTION FRONT IN THE CONDENSED PHASE", *Combust. Explos. Shock Waves*, vol. 7, no. 1, pp. 15–22, 1971.

[25] N. N. Greenwood and A. Earnshaw, "Silicon", in *Chem. Elem.* 2nd ed., Butterworth-Heinemann, Jan. 1997, ch. 9, pp. 328–366, ISBN: 9780750633659. DOI: 10.1016/B978-0-7506-3365-9.50015-8.

[26] C. Li, C. Wang, J. Han, L. Yan, B. Deng, and X. Liu, "A comprehensive study of the high-pressure–temperature phase diagram of silicon", *J. Mater. Sci.*, vol. 53, no. 10, pp. 7475–7485, May 2018, ISSN: 15734803. DOI: 10.1007/s10853-018-2087-9.

[27] G. Eranna, *Crystal Growth and Evaluation of Silicon for VLSI and ULSI*. Taylor & Francis, 2014, ISBN: 9781482232813.

[28] O. D. Shchelikov, "THERMOPHYSlCAL PROPERTIES OF MATERIALS Volume Changes during Melting and Heating of Silicon and Germanium Melts MA1K "Nauka /lnterperiodica"", *High Temp.*, vol. 38, no. 3, pp. 405–412, 2000, ISSN: 1210-1873.

[29] R. K. Eckhoff, S. J. Parker, B. Gruvin, M. Hatcher, and T. Johansson, "Ignitability and Explosibility of Silicon Dust Clouds", *J. Electrochem. Soc.*, vol. 133, no. 12, p. 2631, 1986, ISSN: 00134651. DOI: 10.1149/1.2108493.

[30] W. E. Lee and D. W. Richerson, *Modern Ceramic Engineering: Properties, Processing, and Use in Design*, 3rd ed. CRC Press, 2005, ISBN: 1574446932.

[31] D. Sen, C. Thaulow, S. V. Schieffer, A. Cohen, and M. J. Buehler, "Atomistic study of crack-tip cleavage to dislocation emission transition in silicon single crystals", *Phys. Rev. Lett.*, vol. 104, no. 23, p. 235 502, Jun. 2010, ISSN: 00319007. DOI: 10.1103/PhysRevLett.104.235502.

[32] C. H. Cho, "Characterization of Young's modulus of silicon versus temperature using a "beam deflection" method with a four-point bending fixture", *Curr. Appl. Phys.*, vol. 9, no. 2, pp. 538–545, Mar. 2009, ISSN: 15671739. DOI: 10.1016/j.cap.2008.03.024.

[33] B. E. Deal and A. S. Grove, "General relationship for the thermal oxidation of silicon", *J. Appl. Phys.*, vol. 36, no. 12, pp. 3770–3778, Dec. 1965, ISSN: 00218979. DOI: 10.1063/1.1713945.

[34] N. N. Greenwood and A. Earnshaw, "Titanium, Zirconium and Hafnium", in *Chem. Elem.* 2nd ed., Butterworth-Heinemann, Jan. 1997, ch. 21, pp. 954–975, ISBN: 9780750633659. DOI: 10.1016/B978-0-7506-3365-9.50027-4.

[35] C. W. Greeff, "Phase changes and the equation of state of Zr", *Model. Simul. Mater. Sci. Eng.*, vol. 13, no. 7, p. 1015, Aug. 2005, ISSN: 0965-0393. DOI: 10.1088/0965-0393/13/7/001.

[36] L. Jaworska, J. Cyboron, S. Cygan, A. Zwolinski, B. Onderka, and T. Skrzekut, "Zirconium phase transformation under static high pressure and ω-Zr phase stability at high temperatures", *Materials (Basel).*, vol. 12, no. 14, Jul. 2019, ISSN: 19961944. DOI: 10.3390/ma12142244.

[37] L. Kubin, *Dislocations, Mesoscale Simulations and Plastic Flow*. Oxford University Press, Apr. 2013, ch. 3, ISBN: 9780198525011. DOI: 10.1093/acprof:oso/9780198525011.001.0001.

[38] L. B. Addessio, E. K. Cerreta, and G. T. Gray, "Mechanical Behavior of Zirconium and Hafnium in Tension and Compression", *Metall. Mater. Trans.*, vol. 36A, pp. 2893–2903, Nov. 2005.

[39] P. F. Weck, E. Kim, V. Tikare, and J. A. Mitchell, "Mechanical properties of zirconium alloys and zirconium hydrides predicted from density functional perturbation theory", *Dalt. Trans.*, vol. 44, no. 43, pp. 18 769–18 779, 2015, ISSN: 14779234. DOI: 10.1039/c5dt03403e.

[40] J. P. Abriata, J. Garcés, and R. Versaci, "The O-Zr (Oxygen-Zirconium) system", *Bull. Alloy Phase Diagrams*, vol. 7, no. 2, pp. 116–124, Apr. 1986, ISSN: 01970216. DOI: 10.1007/BF02881546.

[41] W. G. Guldner and L. A. Wooten, "Reactions of Zirconium with Gases at Low Pressure", *J. Electrochem. Soc.*, vol. 93, no. 6, p. 223, 1948, ISSN: 0013-4651. DOI: 10.1149/1.2773810.

[42] B. Puchala and A. Van Der Ven, "Thermodynamics of the Zr-O system from first-principles calculations", *Phys. Rev. B*, vol. 88, p. 94 108, 2013. DOI: 10.1103/PhysRevB.88.094108.

[43] F. Cardarelli, *Materials Handbook: A Concise Desktop Reference*. Springer International Publishing, 2018, ISBN: 9783319389257.

[44] C. M. Efaw, J. L. Vandegrift, M. Reynolds, S. McMurdie, B. J. Jaques, H. Hu, H. Xiong, and M. F. Hurley, "Characterization of zirconium oxides part I: Raman mapping and spectral feature analysis", *Nucl. Mater. Energy*, vol. 21, p. 100 707, Dec. 2019, ISSN: 23521791. DOI: 10.1016/j.nme.2019.100707.

[45] D. FERON, *Nuclear Corrosion Science and Engineering*, ser. Woodhead Publishing Series in Energy. Elsevier Science, 2012, ISBN: 9780857095343.

[46] X. Ma, C. Li, K. Bai, P. Wu, and W. Zhang, "Thermodynamic assessment of the Zr-N system", *J. Alloys Compd.*, vol. 373, no. 1-2, pp. 194–201, Jun. 2004, ISSN: 09258388. DOI: 10.1016/j.jallcom.2003.10.051.

[47] I. I. Chernov, M. S. Staltsov, B. A. Kalin, and L. Y. Guseva, "Some problems of hydrogen in reactor structural materials: A review", *Inorg. Mater. Appl. Res.*, vol. 8, no. 5, pp. 643–650, Sep. 2017, ISSN: 2075115X. DOI: 10.1134/S2075113317050094.

[48] M. Mitkov and D. Božić, "Hydride-dehydride conversion of solid Ti6Al4V to powder form", *Mater. Charact.*, vol. 37, no. 2-3, pp. 53–60, Aug. 1996, ISSN: 10445803. DOI: 10.1016/s1044-5803(96)00061-7.

[49] H. Zhang, H. Shen, X. Che, and L. Wang, "Zirconium powder production through hydrogenation and dehydrogenation process", *Xiyou Jinshu/Chinese J. Rare Met.*, vol. 35, no. 3, pp. 417–421, May 2011, ISSN: 02587076. DOI: 10.3969/j.issn.0258-7076.2011.03.018.

[50] M. Lindgren and I. Panas, "On the fate of hydrogen during zirconium oxidation by water: Effect of oxygen dissolution in α-Zr", *RSC Adv.*, vol. 4, no. 22, pp. 11 050–11 058, Feb. 2014, ISSN: 20462069. DOI: 10.1039/c4ra00020j.

[51] K. Kumar, "Intermetallics: Silicides", in *Encycl. Mater. Sci. Technol.* Elsevier, 2001, pp. 4243–4246, ISBN: 9780080431529. DOI: 10.1016/B0-08-043152-6/00744-0.

[52] W. D. Klopp, "A review of chromium, molybdenum, and tungsten alloys", *J. Less Common Met.*, vol. 42, no. 3, pp. 261–278, 1975, ISSN: 0022-5088. DOI: https://doi.org/10.1016/0022-5088(75)90046-6.

[53] L. Brewer and R. H. Lamoreaux, "The Mo-O system (Molybdenum-Oxygen)", *Bull. Alloy Phase Diagrams*, vol. 1, no. 2, pp. 85–89, 1980, ISSN: 0197-0216. DOI: 10.1007/BF02881199.

[54] C. Zhang, M. C. Gao, Y. Yang, and F. Zhang, "Thermodynamic modeling and first-principles calculations of the Mo–O system", *Calphad*, vol. 45, pp. 178–187, 2014, ISSN: 0364-5916. DOI: https://doi.org/10.1016/j.calphad.2013.12.006.

[55] R. Mitra and R. Wanhill, "Structural Intermetallics", in, Nov. 2017, pp. 229–245, ISBN: 978-981-10-2133-6. DOI: 10.1007/978-981-10-2134-3_10.

[56] T. Minasyan, L. Liu, Y. Holovenko, S. Aydinyan, and I. Hussainova, "Additively manufactured mesostructured MoSi2-Si3N4 ceramic lattice", *Ceram. Int.*, vol. 45, no. 8, pp. 9926–9933, 2019. DOI: 10.1016/j.ceramint.2019.02.035.

[57] S. W. Jo, G. W. Lee, J. T. Moon, and Y. S. Kim, "On the formation of MoSi2 by self-propagating high-temperature synthesis", *Acta Mater.*, vol. 44, no. 11, pp. 4317–4326, Nov. 1996, ISSN: 13596454. DOI: 10.1016/1359-6454(96)00106-1.

[58] H. Okamoto, "The Si-Zr (Silicon-Zirconium) system", *Bull. Alloy Phase Diagrams*, vol. 11, no. 5, pp. 513–519, Oct. 1990, ISSN: 01970216. DOI: 10.1007/BF02898272.

[59] L. Brewer and O. Krikorian, "Reactions of Refractory Silicides with Carbon and Nitrogen", *J. Electrochem. Soc.*, vol. 103, no. 1, p. 38, 1956, ISSN: 00134651. DOI: 10.1149/1.2430231.

[60] H. M. Chen, F. Zheng, H. S. Liu, L. B. Liu, and Z. P. Jin, "Thermodynamic assessment of B-Zr and Si-Zr binary systems", *J. Alloys Compd.*, vol. 468, no. 1-2, pp. 209–216, Jan. 2009, ISSN: 09258388. DOI: 10.1016/j.jallcom.2008.01.061.

[61] J. Canel, J. Zaman, J. Bettembourg, M. Le Flem, and S. Poissonnet, "Composite zirconium silicides through an in situ process", *Int. J. Appl. Ceram. Technol.*, vol. 3, no. 1, pp. 23–31, Jan. 2006, ISSN: 1546542X. DOI: 10.1111/j.1744-7402.2006.02063.x.

[62] M. Le Flem, J. Canel, and S. Urvoy, "Processing and characterization of Zr3Si2 for nuclear applications", *J. Alloys Compd.*, vol. 465, no. 1-2, pp. 269–273, Oct. 2008, ISSN: 09258388. DOI: 10.1016/j.jallcom.2007.10.047.

[63] H. Yeom, B. Maier, R. Mariani, D. Bai, S. Fronek, P. Xu, and K. Sridharan, "Magnetron sputter deposition of zirconium-silicide coating for mitigating high temperature oxidation of zirconium-alloy", *Surf. Coatings Technol.*, vol. 316, pp. 30–38, Apr. 2017, ISSN: 02578972. DOI: 10.1016/j.surfcoat.2017.03.018.

[64] G. Cheol Lee, H. Noh, H. Yeom, H. Jo, T. Kyun Kim, M. Kim, K. Sridharan, and H. Sun Park, "Zirconium-silicide coating on zircaloy-4 substrate for accident tolerance: Effects on oxidation resistance and boiling", *Ann. Nucl. Energy*, vol. 126, pp. 350–358, Apr. 2019, ISSN: 0306-4549. DOI: 10.1016/J.ANUCENE.2018.11.019.

[65] M. Holt, R. J. Campbell, and M. B. D. Nikitin, "Fukushima Nuclear Disaster", Congresiional Research service, Tech. Rep., 2012.

[66] A. V. Tkachenko and T. Y. Kosolapova, "Conditions of preparation of zirconium silicides", *Sov. Powder Metall. Met. Ceram.*, vol. 7, no. 3, pp. 178–181, Mar. 1968, ISSN: 00385735. DOI: 10.1007/BF00774148.

[67] N. Bertolino, U. Anselmi-Tamburini, F. Maglia, G. Spinolo, and Z. Munir, "Combustion synthesis of Zr–Si intermetallic compounds", *J. Alloys Compd.*, vol. 288, no. 1-2, pp. 238–248, Jun. 1999, ISSN: 0925-8388. DOI: 10.1016/S0925-8388(99)00077-8.

[68] S. Shu, F. Guo, and Y. Zhan, "Ab initio Insight Into the Structure and Properties of Zr–Si System", *Phys. Status Solidi - Basic Solid State Phys.*, 2019, ISSN: 15213951. DOI: 10.1002/pssb.201900018.

[69] R. C. Weast, *Handbook of Chemistry and Physics*, 67th. United States: CRC Press Inc, 1986, ISBN: 0-8493-0467-0.

[70] L. Topor and O. J. Kleppa, "Standard enthalpies of formation of Me5Si3 (Me Y, Lu, Zr) and of Hf3Si2", *J. Less-Common Met.*, vol. 167, no. 1, pp. 91–99, Dec. 1990, ISSN: 00225088. DOI: 10.1016/0022-5088(90)90292-R.

[71] S. Meschel and O. Kleppa, "Standard enthalpies of formation of some 4d transition metal silicides by high temperature direct synthesis calorimetry", *J. Alloys Compd.*, vol. 274, no. 1-2, pp. 193–200, Jun. 1998, ISSN: 0925-8388. DOI: 10.1016/S0925-8388(98)00504-0.

[72] I.-J. Cho, K.-T. Park, S.-K. Lee, H. H. Nersisyan, Y.-S. Kim, and J.-H. Lee, "Rapid and cost-effective method for synthesizing zirconium silicides", *Chem. Eng. J.*, vol. 165, no. 2, pp. 728–734, Dec. 2010, ISSN: 1385-8947. DOI: 10.1016/J.CEJ.2010.09.038.

[73] W. E. Lee and D. W. Richerson, *Modern Ceramic Engineering: Properties, Porecessing, and Use in Design*, Fourth. CRC Press, 2018, ISBN: 9871498716918.

[74] C. F. Burmeister and A. Kwade, "Process engineering with planetary ball millss", *Chem. Soc. Rev.*, vol. 42, no. 18, pp. 7660–7667, Aug. 2013, ISSN: 14604744. DOI: 10.1039/c3cs35455e.

[75] L. T. Canham, "Nanoscale semiconducting silicon as a nutritional food additive", *Nanotechnology*, vol. 18, no. 18, May 2007, ISSN: 09574484. DOI: 10.1088/0957-4484/18/18/185704.

[76] H. M. Rong, Private communication, Oct. 2019.

[77] B. K. Yen, "X-ray diffraction study of mechanochemical synthesis and formation mechanisms of zirconium carbide and zirconium silicides", *J. Alloys Compd.*, vol. 268, no. 1-2, pp. 266–269, Mar. 1998, ISSN: 0925-8388. DOI: 10.1016/S0925-8388(97)00581-1.

[78] D. Restrepo, S. M. Hick, C. Griebel, J. Alarcón, K. Giesler, Y. Chen, N. Orlovskaya, and R. G. Blair, "Size controlled mechanochemical synthesis of ZrSi2", *Chem. Commun.*, vol. 49, no. 7, pp. 707–709, Jan. 2013, ISSN: 13597345. DOI: 10.1039/c2cc36323b.

[79] H. Liu, Y. Cai, Q. Xu, Q. Song, and H. Liu, "A novel preparation of Zr-Si intermetallics by electrochemical reduction of ZrSiO4 in molten salts", *New J. Chem.*, vol. 39, no. 12, pp. 9969–9975, Oct. 2015, ISSN: 13699261. DOI: 10.1039/c5nj01896j.

[80] T. Røe, K. Blandhol, J. P. Svanem, and H. Rong, "Silicon Content of Silicon Materials", in *Silicon Chem. Sol. Ind. XIV*, Svolvær, 2018.

[81] A. Jain, S. P. Ong, G. Hautier, W. Chen, W. D. Richards, S. Dacek, S. Cholia, D. Gunter, D. Skinner, G. Ceder, and K. a. Persson, "The Materials Project: A materials genome approach to accelerating materials innovation", *APL Materials*, vol. 1, no. 1, p. 011 002, 2013, ISSN: 2166532X. DOI: 10.1063/1.4812323.

[82] T. Maimaitiyili, "Phase transformation and stability studies of the Zr-H system", PhD thesis, DIvision of Materials Engineering, Lund, Oct. 2015, ISBN: 978-91-7623-552-2.

[83] M. BOYKO, N. MUTS, I. Muts, and R. Gladyshevskii, "Structure refinements of the compounds Pr5Si3 and Zr3Si2", *Chem. Met. Alloy.*, vol. 7, pp. 56–62, Jan. 2014. DOI: 10.30970/cma7.0278.

[84] K. Wiik, Private communication, May 2020.

Appendices

A Estimation of SiO(g) partial pressure

In this thesis, the partial pressure of SiO(g) as a result of different reactions is estimated in a temperature range by determining the equilibrium constant of the reaction at discrete temperatures based on the Gibbs free energy of the reaction. For the reaction

$$i\mathrm{A(s,l)} + j\mathrm{B(s,l} \longrightarrow n\mathrm{C(s,l)} + m\mathrm{D\,(g)} \uparrow \tag{A.1}$$

the partial pressure of D(g) (which corresponds to SiO(g) for the applications in this thesis) can be estimated through the equations:

$$\Delta_r G(T) = -RT \ln K(T) \tag{A.2}$$

where $\Delta_r G(T)$ is the Gibbs free energy of the reaction at the given temperature R is the universal gas constant ($8.314\,\mathrm{J\,K^{-1}\,mol^{-1}}$) T is the given temperature, and $K(T)$ is the equilibrium constant at the given temperature which in turn is described by

$$K(T) = \frac{a^n_{\mathrm{C(s,l)}} a^m_{\mathrm{D\,(g)}}}{a^i_{\mathrm{A(s,l)}} a_{\mathrm{B(s,l)}}} \tag{A.3}$$

where $a^n_{\mathrm{C(s,l)}}$ is the chemical activity of substance C(s, l) in the reaction in Eq. (A.1), *etc.* The partial pressure of D(g) can be estimated at discrete temperatures by solving Eq. (A.2) for $K(T)$, and assuming that the chemical activity of condensed phases is 1 and that the activity of a gas is equal to it's partial pressure divided by the standard pressure ($1\,\mathrm{bar}$). $\Delta_r G(T)$ is in turn calculated by

$$\Delta_r G(T) = n\Delta_f G_{\mathrm{C(s,l)}}(T) + m\Delta_f G_{\mathrm{D\,(g)}}(T) - i\Delta_f G_{\mathrm{A(s,l)}}(T) - j\Delta_f G_{\mathrm{B(s,l)}}(T) \tag{A.4}$$

where $\Delta_f G_{\mathrm{C(s,l)}}$ is the Gibbs free energy formation of substance C(s, l) at temperature T *etc.*, which was collected from HSC Chemistry .

referanse

B Properties of reactants

Table B1 summarizes a selection of compound properties presented in chapter 2. The selection is made based on which properties will be compared between the compounds as part of discussion of expected system behavior or observed results. The table serves as a clear and easy way to verify the comparisons that are made during discussion.

Table B1: Collection of presented chemical and mechanical properties zirconium and silicon compounds

Property	Zr	Si	ZrO_2	SiO_2
Density $[\mathrm{g\,cm^{-3}}]$	6.51	cd: 2.33 Liquid: 2.54		
Phase transition temperature (at 1 bar) [°C]	hcp $\rightarrow$ bcc: 862 bcc $\rightarrow$ liquid: 1857	cd$\rightarrow$liquid: 1412	$\alpha \rightarrow \beta$: 1205 $\beta \rightarrow \gamma$: 1525-2377	
Fracture toughness $[\mathrm{MPa\,m^{1/2}}]$		0.6		
E-modulus [GPa]	91-98.8	130-169		
Stress-strain response	ductile	brittle below $607\,^{\circ}\mathrm{C}$		
UTS [MPa]	280			
max strain [%]	55			
$\Delta_f G^{\ominus}$ $[\mathrm{kJ\,mol^{-1}}]$	0	0	-1043	-856

C Customized flange

The sketch the flange used for room temperature SHS was based on is shown in Figure C1a, and the technical drawing used for machining of the flange is shown in Figure C1b.

a)

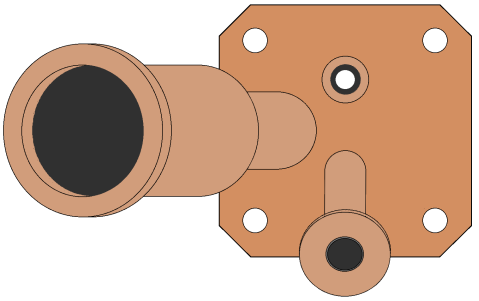

b)

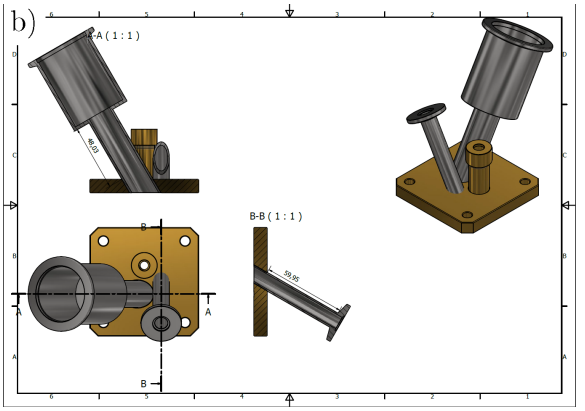

Figure C1: Drawings of the custom flange needed for the room temperature experiments. a) is the initial sketch, and b) is the technical drawing used for machining of the flange.

D Observations during SHS

During the SHS-experiments, some interesting observations were made simply by the naked the eye, and these observations were photographed. These photographs are listed below.

D.1 Heating of igniter in tube furnace

The course of events during an heating of the an igniter during SHS-experiments was filmed, and stills from the video are shown in Figure D2.

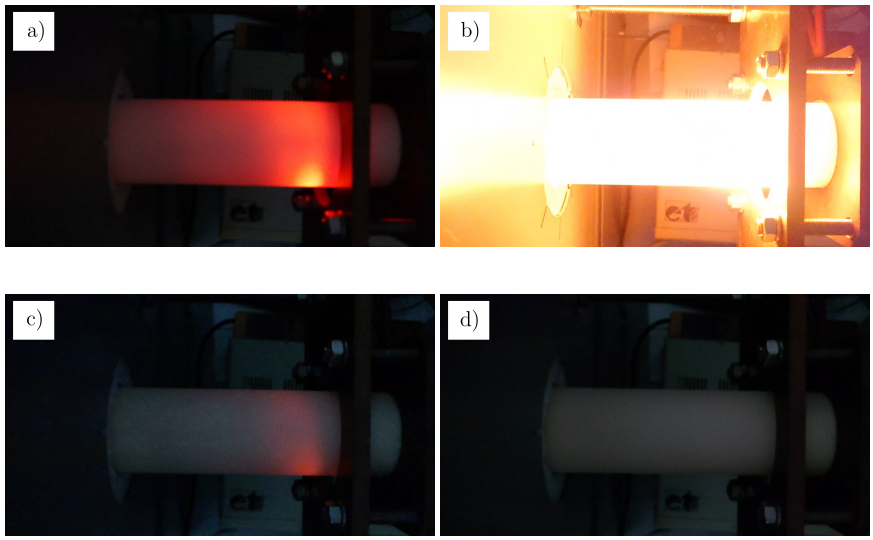

Figure D2: Images of course of events during an SHS-experiment. a) shows the filament glowing when a current is passed through, b) shows the explosion of the igniter pellet, c) shows a fading glow likely coming from the igniter, and d) shows that the glow from both filament and igniter disappears after the explosion

D.2 Zr+2Si(Room temp, Indep. Ign)1 after experiment

Figure D3 shows an image from above and one of the side in contact with the igniter of the sample Zr+2Si(Room temp, Indep. Ign)1 (see Table 3.5).

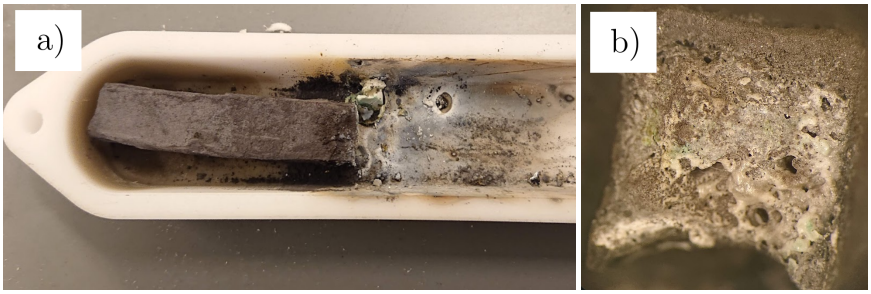

Figure D3: Images of the sample Zr+2Si(Room temp, Indep. Ign)1 (see Table 3.5). a) is a top view of the sample, and b) is an image of the side that was in contact with the igniter

D.3 Cracking of alumina tube by Zr+2Si(Room temp, Indep. Ign)2

The alumina tube and the part of the sample Zr+2Si(Room temp, Indep. Ign)2 (see Table 3.5) that was in contact with the igniter is shown in Figure D4

Figure D4: Image of alumina tube sample container and part of Zr+2Si beam that was in contact with igniter during a room temperature SHS experiment where the filament was adjacent to the igniter pellet which was in contact with the Zr+2Si beam

D.4 Igniter pieces on Zr+Si(Room temp, Ign. in fila.)

Figure D5 shows an image of the sample Zr+Si(Room temp, Ign. in fila.) (see Table 3.5) after the experiment.

Figure D5: Zr+Si(Room temp, Ign. in fila.) (see Table 3.5) after experiment. The small white pieces are pieces of the exploding igniter.

D.5 Samples Zr+2Si(600 °C, Ign. in cylinder) and Zr+2Si(600 °C, Ign. in cylinder) before and after the experiment

a)

b)

Figure D6: Images of Samples Zr+2Si(600 °C, Ign. in cylinder) and Zr+2Si(600 °C, Ign. in cylinder) a) before and b) after the experiment

D.6 Zr+2Si(1400 °C, Temp. grad.) after synthesis

A top view of the sample Zr+2Si(1400 °C, Temp. grad.) (see Table 3.5) after the experiment is shown in Figure D7.

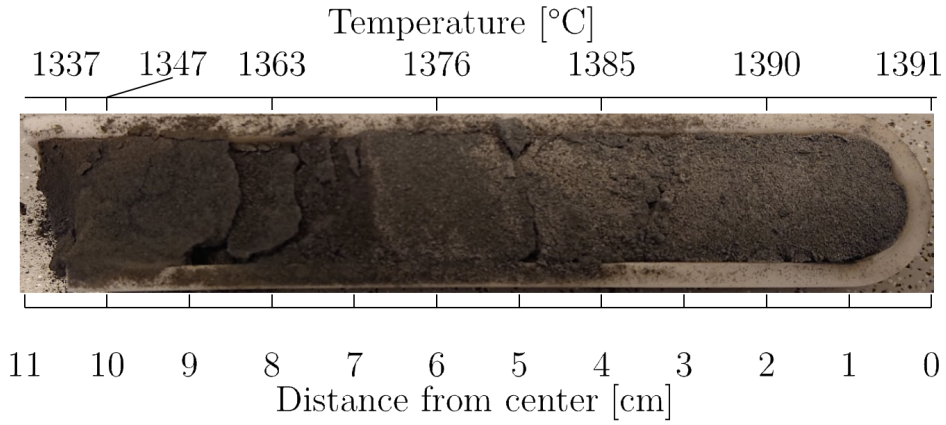

Figure D7: Top view of Zr+2Si(1400 °C, Temp. grad.) (see Table 3.5) after the experiment

E Reactivity between zirconium silicides and precursors - diffractograms

The diffractograms used to determine the compositions in Table 4.11 by combined Pawley and Rietveld refinement are presented below.

E.1 3Zr + Si

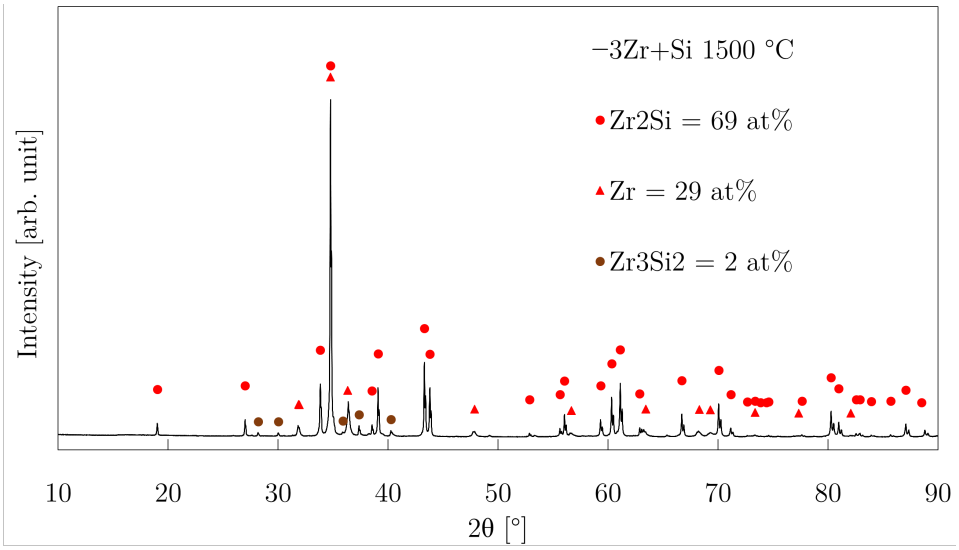

Figure E8: The resulting diffractogram of XRD of the sample "3Zr+Si"(see section 3.6.2) at 1500 °C for one hour, with a heating rate of 200 °C h^{-1}. Which phases contribute to each peak is shown with indicators.

E.2 $ZrSi_2$ + 3Zr

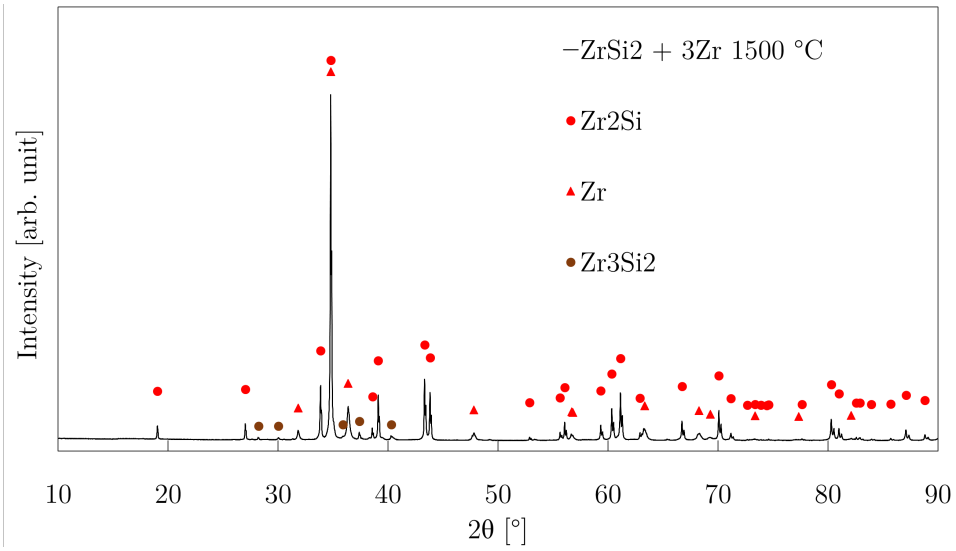

Figure E9: The resulting diffractogram of XRD of the sample "$ZrSi_2$+Zr" (see section 3.6.2) after it was heated and held at 1500 °C for one hour, with a heating rate of 200 °C h^{-1}. Which phases contribute to each peak is shown with indicators.

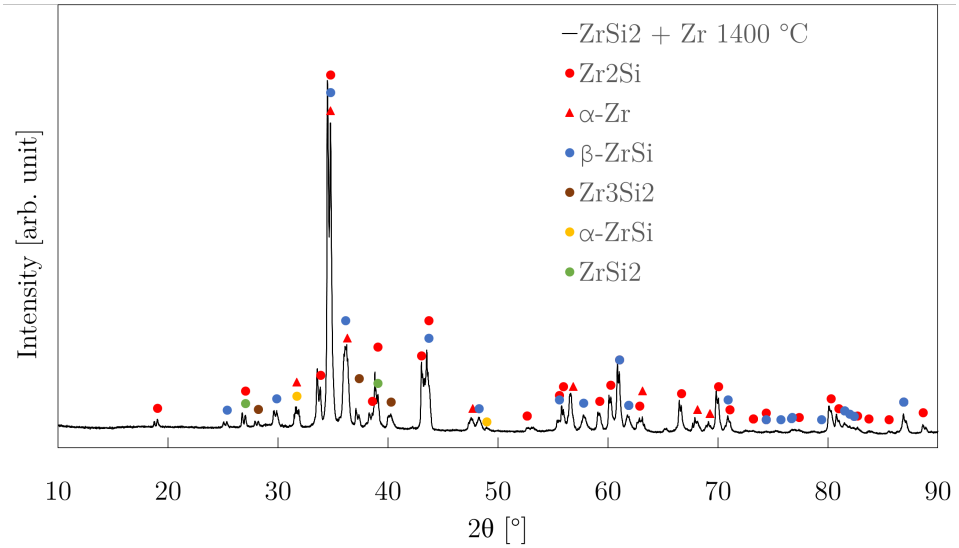

Figure E10: The resulting diffractogram of XRD of the sample "$ZrSi_2$+Zr"(see section 3.6.2) after it was heated to 1400 °C with a heating rate of 200 °C h^{-1}. Which phases contribute to each peak is shown with indicators.

E.3 $Zr_{(3)}Si$ + 5Si

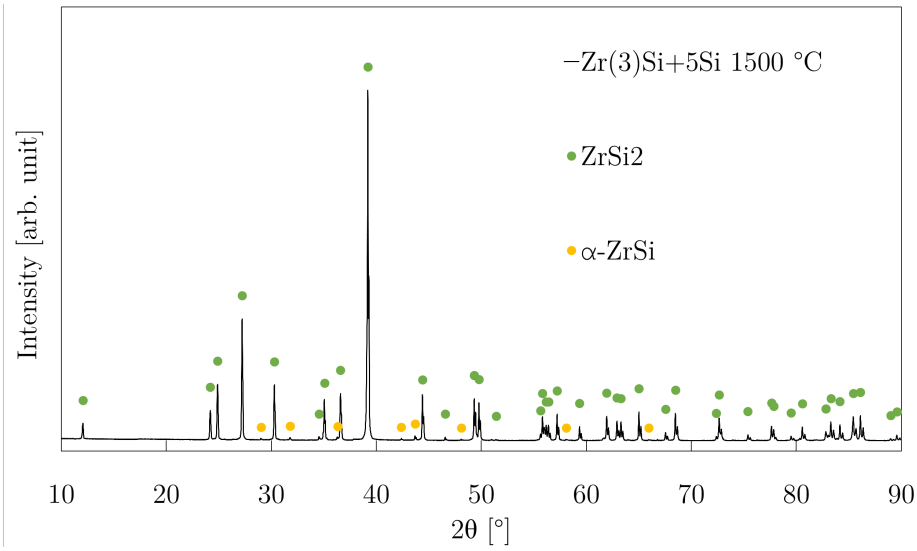

Figure E11: The resulting diffractogram of XRD of the mixture "$Zr_{(3)}Si$ + 5 Si" (see section 3.6.2), after it was heated and held at 1500 °C for one hour, with a heating rate of 200 °C h^{-1}. Which phases contribute to each peak is shown with indicators.

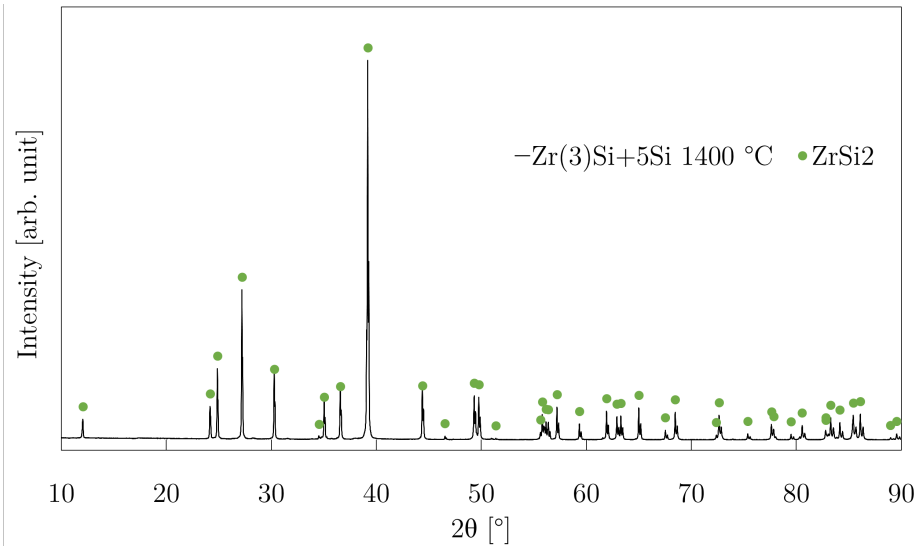

Figure E12: The resulting diffractogram of XRD of the mixture "$Zr_{(3)}Si$ + 5 Si" (see section 3.6.2), after it was heated to 1400 °C with a heating rate of 200 °C h^{-1}. Which phases contribute to each peak is shown with indicators.

F Documentation for received powders

Si(<75) particle size distribution

Result Analysis Report

Particle Name:
Silicon

Accessory Name:
Scirocco 2000

Size range:
0.20 to 2000.000 um

Obscuration:
2.68 %

Particle RI:
3.500

Absorption:
0.1

Dispersant RI:
1.000

Weighted Residual:
0.252 %

Specific Surface Area:
0.82 m²/g

Span :
2.335

Vol. Weighted Mean D[4,3]:
21.527 um

Result units:
Volume

Surface Weighted Mean D[3,2]:
7.316 um

d(0.1): 3.473 um **d(0.5):** 17.852 um **d(0.9):** 45.153 um

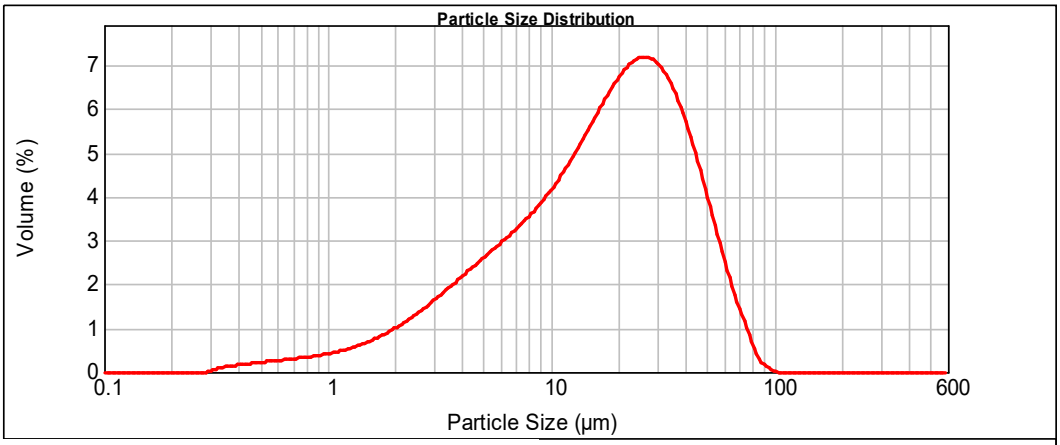

Size (µm)	Vol Under %	Size (µm)	Vol Under %	Size (µm)	Vol Under %	Size (µm)	Vol Under %	Size (µm)	Vol Under %	Size (µm)	Vol Under %
0.010	0.00	0.071	0.00	0.501	0.51	3.548	10.27	25.119	65.25	177.828	100.00
0.011	0.00	0.079	0.00	0.562	0.69	3.981	11.82	28.184	70.66	199.526	100.00
0.013	0.00	0.089	0.00	0.631	0.89	4.467	13.54	31.623	75.96	223.872	100.00
0.014	0.00	0.100	0.00	0.708	1.10	5.012	15.43	35.481	81.01	251.189	100.00
0.016	0.00	0.112	0.00	0.794	1.34	5.623	17.47	39.811	85.62	281.838	100.00
0.018	0.00	0.126	0.00	0.891	1.61	6.310	19.69	45.000	89.89	316.228	100.00
0.020	0.00	0.141	0.00	1.000	1.90	7.079	22.08	50.119	93.02	354.813	100.00
0.022	0.00	0.158	0.00	1.122	2.24	7.943	24.65	56.234	95.67	398.107	100.00
0.025	0.00	0.178	0.00	1.259	2.61	8.913	27.42	60.000	96.85	446.684	100.00
0.028	0.00	0.200	0.00	1.413	3.05	10.000	30.41	70.795	98.90	501.187	100.00
0.032	0.00	0.224	0.00	1.585	3.55	11.220	33.66	75.000	99.36	562.341	100.00
0.035	0.00	0.251	0.00	1.778	4.14	12.589	37.21	89.125	99.93	630.957	100.00
0.040	0.00	0.282	0.00	1.995	4.84	14.125	41.07	100.000	100.00	707.946	100.00
0.045	0.00	0.316	0.02	2.239	5.64	15.849	45.28	110.000	100.00	794.328	100.00
0.050	0.00	0.355	0.10	2.512	6.58	17.783	49.84	125.893	100.00	891.251	100.00
0.056	0.00	0.398	0.21	2.818	7.65	20.000	54.84	141.254	100.00	1000.000	100.00
0.063	0.00	0.447	0.35	3.162	8.88	22.387	59.90	150.000	100.00		

Si(10-75) particle size distrubution

Result Analysis Report

Particle Name: Silicon	**Accessory Name:** Scirocco 2000	**Size range:** 0.20 to 2000.000 um	**Obscuration:** 1.58 %
Particle RI: 3.500	**Absorption:** 0.1		
	Dispersant RI: 1.000	**Weighted Residual:** 0.472 %	

Specific Surface Area: 0.23 m²/g	**Span :** 1.297	**Vol. Weighted Mean D[4,3]:** 32.285 um	**Result units:** Volume
Surface Weighted Mean D[3,2]: 26.080 um			

d(0.1): 15.625 um **d(0.5): 29.218 um** **d(0.9): 53.514 um**

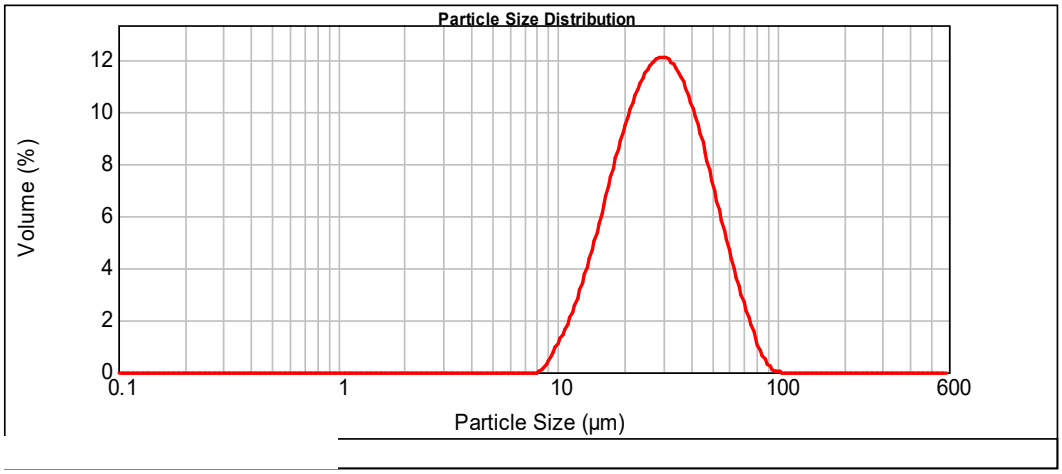

Size (µm)	Vol Under %	Size (µm)	Vol Under %	Size (µm)	Vol Under %	Size (µm)	Vol Under %	Size (µm)	Vol Under %	Size (µm)	Vol Under %
0.010	0.00	0.500	0.00	9.000	0.07	30.000	52.10	95.000	100.00	400.000	100.00
0.020	0.00	0.600	0.00	10.000	0.60	35.000	64.14	100.000	100.00	500.000	100.00
0.030	0.00	0.700	0.00	11.000	1.48	40.000	73.80	110.000	100.00	600.000	100.00
0.040	0.00	0.800	0.00	12.000	2.72	45.000	81.27	120.000	100.00	700.000	100.00
0.050	0.00	0.900	0.00	13.000	4.33	50.000	86.93	130.000	100.00	800.000	100.00
0.060	0.00	1.000	0.00	14.000	6.27	55.000	91.11	140.000	100.00	900.000	100.00
0.070	0.00	2.000	0.00	15.000	8.48	60.000	94.15	150.000	100.00	1000.000	100.00
0.080	0.00	3.000	0.00	16.000	10.95	65.000	96.30	160.000	100.00	1500.000	100.00
0.090	0.00	4.000	0.00	17.000	13.61	70.000	97.79	170.000	100.00	2000.000	100.00
0.100	0.00	5.000	0.00	18.000	16.44	75.000	98.79	180.000	100.00		
0.200	0.00	6.000	0.00	19.000	19.39	80.000	99.42	190.000	100.00		
0.300	0.00	7.000	0.00	20.000	22.42	85.000	99.78	200.000	100.00		
0.400	0.00	8.000	0.00	25.000	37.84	90.000	99.94	300.000	100.00		

Si(10-75) chemical analysis

From : **Elkem Bremanger**

CERTIFICATE OF ANALYSIS

CHEMICAL ANALYSIS

Elements	%
% Si	99,70
% Fe	0,031
% Al	0,099
% Ca	0,012
% Ti	0,002

Fe, Al, Ca and Ti are measured with XRF.
Si= 99,9% - Al-Ca-Fe-Ti.

Zr-powder particle size distriburion

LIPMANN WALTON & CO LTD

Established 1953, Member of the Minor Metals Trade Association

Palace Gate House, Palace Gate, Hampton Court Road, East Molesey, Surrey, KT8 9BN, United Kingdom
Tel: +44 (0) 208 487 0236 / Fax: +44 (0) 208 941 7366 / Mob: + 44 (0) 7785 330 042
Web: www.lipmann.co.uk / E-mail: lipmann@lipmann.co.uk

18th June 2019

Particle Size Analysis

Particle Name: Zirconia av	**Accessory Name:** Hydro 2000S (A)	**Analysis model:** General purpose	**Sensitivity:** Normal
Particle RI: 2.165	**Absorption:** 0.1	**Size range:** 0.100 to 1000.000 um	**Obscuration:** 14.59 %
Dispersant Name: Water	**Dispersant RI:** 1.330	**Weighted Residual:** 1.418 %	**Result Emulation:** Off
Concentration: 0.0623 %Vol	**Span :** 1.769	**Uniformity:** 0.546	**Result units:** Volume
Specific Surface Area: 0.201 m?g	**Surface Weighted Mean D[3,2]:** 29.839 um	**Vol. Weighted Mean D[4,3]:** 66.765 um	

d(0.1): 17.846 um **d(0.5):** 60.601 um **d(0.9):** 125.067 um

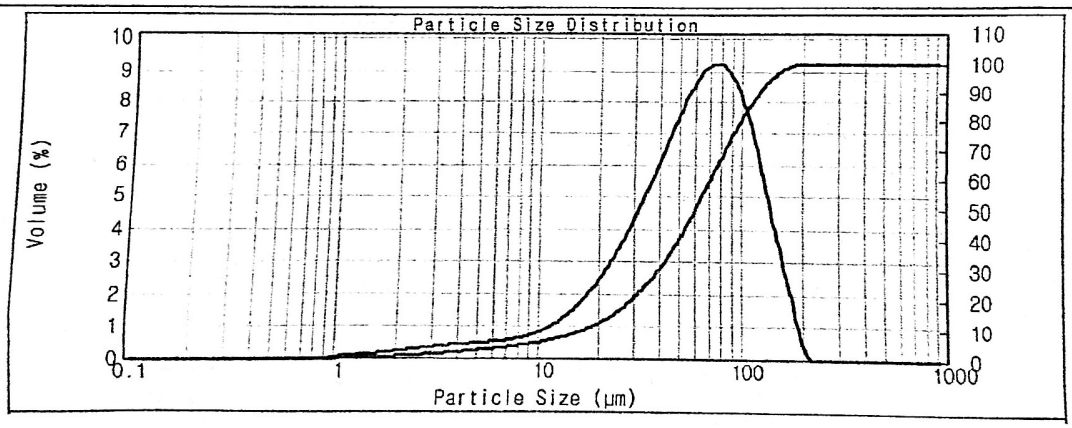

Size (µm)	Vol Under %
0.010	0.00
0.011	0.00
0.013	0.00
0.015	0.00
0.017	0.00
0.020	0.00
0.023	0.00
0.026	0.00
0.030	0.00
0.035	0.00
0.040	0.00
0.046	0.00
0.052	0.00
0.060	0.00
0.069	0.00
0.079	0.00
0.091	0.00

Size (µm)	Vol Under %
0.105	0.00
0.120	0.00
0.138	0.00
0.158	0.00
0.182	0.00
0.209	0.00
0.240	0.00
0.275	0.00
0.316	0.00
0.363	0.00
0.417	0.00
0.479	0.00
0.550	0.00
0.631	0.00
0.724	0.00
0.832	0.00
0.955	0.00

Size (µm)	Vol Under %
1.096	0.02
1.259	0.10
1.445	0.19
1.660	0.31
1.905	0.46
2.188	0.65
2.512	0.88
2.884	1.14
3.311	1.45
3.802	1.79
4.365	2.16
5.012	2.56
5.754	2.98
6.607	3.43
7.586	3.92
8.710	4.48
10.000	5.12

Size (µm)	Vol Under %
11.482	5.90
13.183	6.88
15.136	8.11
17.378	9.66
19.953	11.60
22.909	14.01
26.303	16.96
30.200	20.51
34.674	24.75
39.811	29.76
45.709	35.58
52.481	42.24
60.256	49.68
69.183	57.71
79.433	66.04
91.201	74.24
104.713	81.83

Size (µm)	Vol Under %
120.226	88.37
138.038	93.53
158.489	97.17
181.970	99.33
208.930	100.00
239.883	100.00
275.423	100.00
316.228	100.00
363.078	100.00
416.869	100.00
478.630	100.00
549.541	100.00
630.957	100.00
724.436	100.00
831.764	100.00
954.993	100.00
1096.478	100.00

Size (µm)	Vol Under %
1258.925	100.00
1445.440	100.00
1659.587	100.00
1905.461	100.00
2187.762	100.00
2511.886	100.00
2884.032	100.00
3311.311	100.00
3801.894	100.00
4365.158	100.00
5011.872	100.00
5754.399	100.00
6606.934	100.00
7585.776	100.00
8709.636	100.00
10000.000	100.00

Zr-powder chemical analysis

LIPMANN WALTON & CO LTD

Established 1953, Member of the Minor Metals Trade Association

Palace Gate House, Palace Gate, Hampton Court Road, East Molesey, Surrey, KT8 9BN, United Kingdom
Tel: +44 (0) 208 487 0236 / Fax: +44 (0) 208 941 7366 / Mob: + 44 (0) 7785 330 042
Web: www.lipmann.co.uk / E-mail: lipmann@lipmann.co.uk

18th June 2019

Certificate of Analysis

Ref: SAL 3712

Material: Zirconium Powder

(Unit : wt. %)

Components	Result
$Zr_{total} + Hf_{total}$	Min 99
Magnesium (Mg)	Max 0.002
Silicon (Si)	Max 0.095
Aluminum (Al)	Max 0.003
Titanium (Ti)	Max 0.11
Calcium (Ca)	Max 0.065
Oxygen (O)	Max 0.40
Nitrogen (N)	Max. 0.02
Hydrogen (H)	Max. 0.007
Iron (Fe)	Max 0.03
Carbon (C)	Max 0.004
Hafnium (Hf)	0.02
Nickel (Ni)	Max 0.002
Chlorine (Cl)	Max 0.003

Johan Moan Dalene

Self-propagating high-temperature syntheis of zirconium disilicide

NTNU
Kunnskap for en bedre verden